DTU Library

Pyrolytic carbon electrodes for bioelectrochemical applications

Hassan, Yasmin Mohamed

Publication date:
2018

Document Version
Publisher's PDF, also known as Version of record

Link back to DTU Orbit

Citation (APA):
Hassan, Y. M. (2018). Pyrolytic carbon electrodes for bioelectrochemical applications. DTU Nanotech.

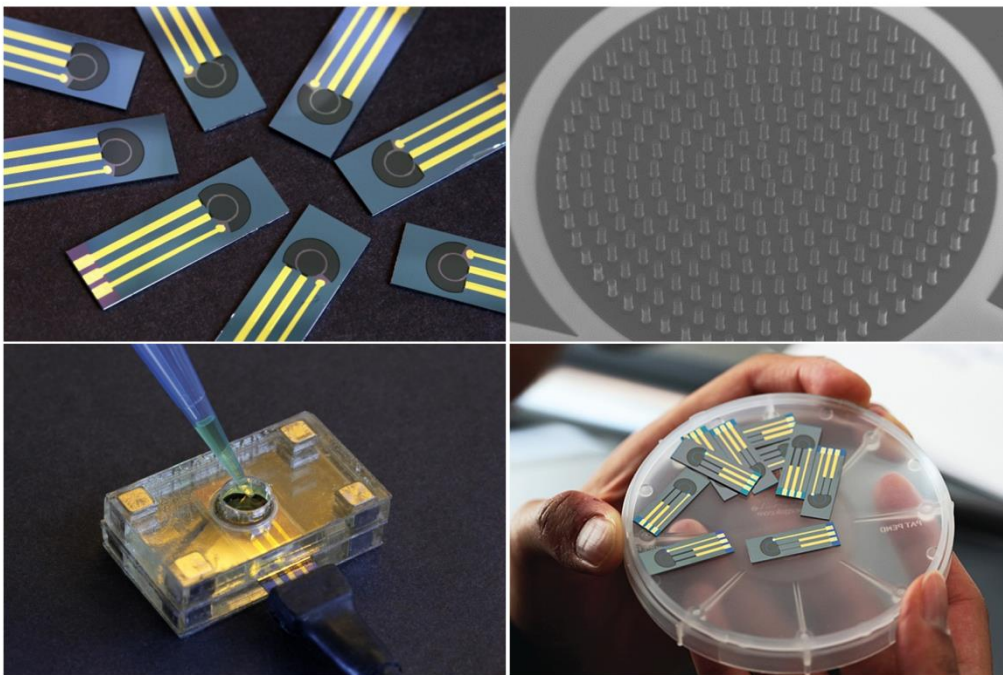# Pyrolytic carbon electrodes for bioelectrochemical applications

Yasmin Mohamed Hassan
PhD Thesis May2018

DTU Nanotech
Department of Micro- and Nanotechnology

Pyrolytic carbon electrodes for bioelectrochemical applications

Yasmin Mohamed Hassan

Ph.D. Thesis

May 2018

Main supervisor: Assoc. Prof. Stephan Sylvest Keller

Co-supervisor: Postdoc Claudia Caviglia

Preface

This thesis is submitted as partial requirement for obtaining a Ph.D. degree from the Technical University of Denmark (DTU). The project was funded by the Young Investigator Program of the Villum Foundation (project no. VKR023438).

The research was carried out in the Department of Micro- and Nanotechnology (DTU Nanotech) from May 2015 to May 2018. The Ph.D. was supervised by Assoc. Prof. Stephan Sylvest Keller and co-supervised by postdoc Claudia Caviglia.

Kongens Lyngby,
1st May, 2018
Yasmin Mohamed Hassan

Contents

Abstract

Carbon represents an interesting electrode material due to its favourable material properties such as biocompatibility and high chemical resistance. For this reason it has been widely used for several electrochemical applications including electroanalytical chemistry, fuel cells or electrocatalysis. In particular, among the available carbon allotropes, pyrolytic carbon represents a promising material for various applications such as electrochemical sensors, capacitors, batteries or microelectromechanical systems (MEMS). Pyrolytic carbon can be obtained from the pyrolysis of lithographically patterned photoresists in a fabrication process called carbon MEMS (C-MEMS) which is simple, highly reproducible and offers the possibility to customize the electrode design. Due to its biocompatibility, pyrolytic carbon has been previously used as biosensor and for cell studies. The aim of the research work of this thesis was the fabrication and optimization of two dimensional (2D) and three dimensional (3D) pyrolytic carbon electrodes for bioelectrochemical applications.

The research presented in this thesis focused on: (1) the optimization of the pyrolysis process used to obtain the pyrolytic carbon electrodes in order to obtain improved performances in terms of conductivity and electrochemical behaviour. (2) The investigation of new polymer templates for the fabrication of new carbon structures. (3) The development of a platform for electrochemical monitoring of 2D bone cell cultures using electrochemical impedance spectroscopy (EIS) and square wave voltammetry (SWV). (4) The design and fabrication of 3D electrodes for the development of a 3D *in vitro* model for the support of bone diseases research and for preliminary studies regarding use of pyrolytic carbon as anode material in biophotovoltaic cells.

Resumé

Kulstof er et spændende elektrodemateriale da det har fordelagtige egenskaber såsom biokompatibilitet og høj kemisk stabilitet. Af den årsag har det haft mange elektrokemiske anvendelser som for eksempel i elektroanalytisk kemi, brændselsceller og elektrokatalyse. Blandt de forskellige typer af kulstof-baserede materialer har pyrolytisk kulstof et stort potentiale til anvendelse i forskellige applikationer såsom elektrokemiske sensorer, kondensatorer, batterier og mikroelektromekaniske systemer (MEMS). Pyrolytisk kulstof kan blandt andet produceres i gennem pyrolyse af lysfølsomme resiner struktureret med fotolitografi i en fremstillingsprocess kaldt C-MEMS, som er enkel, meget præcis og gør det muligt at elektrodedesigne de specifikke behov. Pyrolytisk kulstof har tidligere været brugt i biosensorer eller til forskningsstudier med celler. Formålet med forskningsarbejdet i denne afhandling var at fremstille og optimere to-dimensionelle (2D) og tre-dimensionelle (3D) pyrolytiske kulstofelektroder til bioelektrokemiske anvendelser.

Forskningen, som er inkluderet i denne afhandling fokuserer på: (1) at optimere pyrolyse processen, som blev brugt til at fremstille de pyrolytiske kulstofelektroder for at opnå forbedrede elektriske og elektrokemiske egenskaber. (2) at undersøge nye plastikmaterialer som udgangspunkt til fremstilling af nye kulstofelektroder. (3) at udvikle en platform til elektrokemisk observering af 2D kulturer af knogleceller ved brug af elektrokemisk impedance spektroskopi (EIS) og square wave voltammetry (SWV). (4) at designe en fremstilling af 3D elektroder til udviklingen af en 3D *in vitro* model til understøttelse af forskning i knoglesygedomme og til de første undersøgelser vedrørende brug af pyrolytisk kulstof som anode materiale i biofotovoltaiske celler.

Acknowledgements

During the past three years many people made this experience in Denmark somehow special, sharing nice memories with me. Now it´s time to give you the recognition you deserve and I will do my best to thank all of you! ☺

First of all, I would like to thank my supervisors, Stephan and Claudia, for giving me the possibility to work on this project. Thank you Stephan for believing in me from the beginning, for understanding my very (sometimes too much) structured way of thinking and for pushing me to explore new crazy ideas! Thank you for always finding the time to discuss and help me even though you had an incredible busy schedule! I´m proud to say that I had an amazing supervisor, and I hope you will keep up the good work with the new PhDs! ☺ Thank you Claudia for the useful inputs on the part of the project related to cell work.

Thanks to all the present and past members of the Biomaterial Microsystems group: Zarmeena, Long, Suhith, Ritika, Sheida, Thor, Hannah, Gaetano, Ioannis, Stefania, Florence. You were the ones who made BioMic a cool group, and I´m so happy I have been part of it! Thanks to my officemate Nina, the loudest Danish person I have ever met! You brought fun to the office and helped me to take things less seriously when needed! Thanks to my students, Maxime, Sebastiano and Leonardo for the help during my project. It has been a pleasure supervising you, seeing you become more and more confident in the lab and I´m really proud of the great work you delivered! Thanks to the neighbouring Nanoprobes group, for treating me like an honorary member and for asking me to join during your lunches and coffee breaks!

Thanks to the great friends I met at DTU: *le mie ggggioie* Laura e Andrea, Bannay, Fabio, Lidia, Giorgia, Simo, Marco M., Ada and Lucia. You always managed to make me smile even after a bad day in the lab! ☺ Thanks to the amazing DTU volley club! I can´t make a list of all the awesome people that form this group…I can just say thanks for all the fun times, tournaments and parties we had! In particular, thanks to the DTU

List of abbreviations

$[Fe(CN)_6]^{3-}$	Ferricyanide
$[Fe(CN)_6]^{4-}$	Ferrocyanide
2D	Two-dimensional
3D	Three-dimensional
A	Surface area
ALP	Alkaline Phosphatase
a_{ox}	Activity of the oxidized species
a_{red}	Activity of the reduced species
ATP	Adenosine triphosphate
Au	Gold
BCIP-NBT	5-bromo-4-chloro-3-indolyl phosphate/nitroblue tetrazolium
BPV	Biological photovoltaic cells
BSE	Backscattered electrons
C	Carbon
C-MEMS	Carbon MEMS
CCD	Central composite design
C_{dl}	Double layer capacitance
CE	Counter electrode
CI	Cell index
CPE	Constant phase element
CV	Cyclic voltammetry
D	Diffusion coefficient
DEET	Direct extracellular electron transfer
DoE	Design of experiments
e^-	Electron
E^0	Standard potential at standard conditions
E_0	Amplitude of the applied potential
$E^{0'}$	Formal potential
ECIS	Electric Cell-substrate Impedance Sensing
ECM	Extracellular matrix
E_f	Forward potential

E_i	Initial potential
EIS	Electrochemical impedance spectroscopy
E_{pa}	Anodic peak potential
E_{pc}	Cathodic peak potential
E_s	Step potential
F	Faraday constant
f	Frequency
GBL	Gammabutyrolactone
GC	Glassy carbon
GPI	Glycosyl-phosphatidylinositol
H_2	Hydrogen
H_2O	Water
H_2O_2	Hydrogen peroxide
HCl	Hydrogen chloride
HF	Hydrogen fluoride
hMSCs	Human mesenchymal stem cells
HOMO	Highest occupied molecular orbital
IC	Integrated circuit
ICP-RIE	Inductively coupled plasma reactive ion etching
IHP	Inner Helmholtz plane
j	Unit imaginary number
LDH	Lactate dehydrogenase
LUMO	Lowest unoccupied molecular orbital
MEMS	Microelectromechanical systems
MTS	3-(4,5-dimethylthiazol-2-yl)-5-(3-carboxymethoxyphenyl)-2-(4-sulfophenyl)-2H-tetrazolium
MTT	3-(4,5-dimethylthiazolyl)-2,5-diphenyltetrazolium bromide
MWCNTs	Multi-walled carbon nanotubes
n	Number of electrons
n_c	Number of center points
N_2	Nitrogen
NADPH	Nicotinamide adenine dinucleotide phosphate
NH_4OH	Ammonium hydroxide
OHP	Outer Helmholtz plane

Ox	Oxidized species
pAP	P-aminophenol
pAPP	P-aminophenyl phosphate
PGMEA	Propylene glycol methyl ether acetate
PMMA	Poly(methyl methacrylate)
pNP	4-nitrophenol
pNPP	4-nitrophenylphosphate
pQI	P-quinone imine
PS	Polystyrene
PSA	Pressure sensitive adhesive
Pt	Platinum
PVP	Poly(vinylpyrrolidone)
R	Gas constant
R_{ct}	Charge transfer resistance
RE	Reference electrode
Red	Reduced species
R_s	Solution resistance
R_{seal}	Sealing resistance
RSM	Response surface methodology
RT-PCR	Reverse transcription polymerase chain reaction
SE	Secondary electrons
SEM	Scanning electron microscope
SHE	Standard hydrogen electrode
SWCNTs	Single-walled carbon nanotubes
SWV	Square wave voltammetry
T	Temperature
t	Time
WE	Working electrode
x	Independent variable
y	Response
Z_{CE}	Impedance of the counter electrode
Z_{imag}	Imaginary part of the impedance
Z_{real}	Real part of the impedance
Z_S	Impedance of the electrolyte solution

Z_{WE}	Impedance of the working electrode
α	Distance of the axial run from the design centre
α	Multiplication factor of the CPE
α_i	Regression coefficient i
β	Intercept
ΔE_p	Potential difference between the oxidation and reduction peaks
ϵ	Error term
τ	Time period
φ	Phase shift
ω	Radial frequency
ν	Scan rate

List of publications

Paper I   **Pyrolytic carbon microelectrodes for impedance based cell sensing**

Y. M. Hassan, C. Caviglia, S. Hemanth, D. M. A. Mackenzie, D. H. Petersen, S. S. Keller

ECS Transactions, vol. 72, no. 1, pp. 35–44, 2016

Paper II   **High temperature SU-8 pyrolysis for fabrication of carbon electrodes**

Y. M. Hassan, C. Caviglia, S. Hemanth, D. M. A. Mackenzie, T.S. Alstrøm, D. H. Petersen, S. S. Keller

Journal of Analytical and Applied Pyrolysis, vol. 125, pp. 91-99, Apr. 2017

Paper III   **Monitoring of Saos-2 cell differentiation on pyrolytic carbon electrodes**

Y. M. Hassan, C. Caviglia, L. Massa, S. S. Keller

Manuscript

Paper IV   **In situ monitoring of alkaline phosphatase activity in three-dimensional cell cultures**

C. Caviglia, R. Pimentel C., S. De Roni, Y. M. Hassan, S. Hemanth, M. Dufva, S. S. Keller

Manuscript

Contributions to the papers

Paper I	I designed, planned and performed the fabrication of the electrodes and analyzed the data. I wrote the paper.
Paper II	I designed, planned and performed all the experiments. I evaluated the results and wrote the manuscript.
Paper III	I contributed to the design of the experiments. I planned and performed all the experiments. I also analyzed the data and wrote the manuscript.
Paper IV	I fabricated the 2D electrodes and the 3D carbon pillar electrodes. I took care of the culturing and expansion of the cell culture used in the experiments with the 3D carbon pillar electrodes. I contributed with the writing of the part regarding the fabrication of the 3D carbon pillar electrodes.

List of conference contribution

I	**Pyrolysed carbon microelectrodes with improved performance for cyclic voltammetry and EIS**
	<u>Y. M. Hassan</u>, F. Gavin, C. Caviglia, S. Hemanth, D. M. A. Mackenzie, L. Amato, D. H. Petersen, S. S. Keller
	Electrochemical science and technology conference (Danish Electrochemical Society annual meeting), October 1-2, 2015, Copenhagen, Denmark
	(POSTER)
II	**Pyrolytic carbon microelectrodes for impedance based cell sensing**
	<u>Y. M. Hassan</u>, C. Caviglia, S. Hemanth, D. M. A. Mackenzie, D. H. Petersen, S. S. Keller
	229th Electrochemistry Society Meeting,, May 29-June 2, 2016, San Diego, USA
	(TALK)
III	**Optimized SU-8 pyrolysis for fabrication of pyrolytic carbon microelectrodes**
	<u>Y. M. Hassan</u>, C. Caviglia, S. Hemanth, D. M. A. Mackenzie, D. H. Petersen, T.S. Alstrøm, S. S. Keller
	42nd International conference on Micro and Nano Engineering, September 19-23, 2016, Vienna, Austria
	(TALK)
IV	**3D pyrolytic carbon pillar electrodes for bioelectrochemical applications**
	<u>Y. M. Hassan</u>, C. Caviglia, S. De Roni, R. Pimentel C., M. Dufva, S. S. Keller
	43rd International conference on Micro and Nano Engineering, September 18-22, 2017, Braga, Portugal
	(POSTER)
V	**Monitoring of Saos-2 cell differentiation on pyrolytic carbon electrodes**
	<u>Y. M. Hassan</u>, C. Caviglia, L. Massa, S. S. Keller
	17th *international conference on electroanalysis,* June 3-7, 2018, Rodos, Greece
	(POSTER)

VI	**Microfabrication of 3D pyrolytic carbon electrodes for electrochemistry** S.Hemanth, C. Caviglia, Y.M. Hassan, T.A. Anhøj, S.S. Keller *42nd International conference on Micro and Nano Engineering,* September 19- 23, 2016, Vienna, Austria (TALK)
VII	**Carbon Microelectrodes for Real Time Osteoporosis Drug Screenings** C. Caviglia, G. Panagia, S. Hemanth, Y. M. Hassan, S. S. Keller *229th Electrochemistry Society Meeting,*, May 29- June 2, 2016, San Diego, USA (TALK)
VIII	**3D *in vitro* system for bone cell studies** C. Caviglia, S. De Roni, R. Pimentel C., G. Panagia, Y. M. Hassan, S. Hemanth, S. S. Keller *EMBS Micro and Nanotechnology in Medicine conference,* December 12- 16, 2016, Waikoloa, Hawaii (POSTER)
IX	**Three-dimensional sensing scaffold for bone cells studies** C. Caviglia, S. Hemanth, Y. M. Hassan, G. Panagia, S. S. Keller *10th German BioSensor Symposium,*, March 20-23, 2017, Posdam, Germany (TALK)
X	**3D pyrolytic carbon microelectrodes for electrochemical sensing** S. Hemanth, C. Caviglia, Y.M. Hassan, J. Emnéus, S.S. Keller *10th German BioSensor Symposium*, March 20-23, 2017, Posdam, Germany (POSTER)

1. Introduction

1.1 Motivation

The study of cellular behaviour is a fundamental tool for the understanding of diseases related to cellular dysfunctions such as developmental disorders, neurodegeneration and cancer. Advances in this research field could help elucidate the molecular mechanisms and fundamental cellular processes and pave the way for improvements in the provided treatments and therapies. The complex mechanisms which regulate cellular functions can be investigated by using *in vitro* systems in order to monitor cellular dynamics. These cell culture models represent a powerful tool to obtain preliminary information about cell behaviour, even if they do not represent all the complex interactions to which cells are exposed to in the *in vivo* environment [1]. *In vitro* models have been used for years in the field of biology and biomedical research, finding their main applications in the fields of drug discovery and toxicity testing [2‑4]. Among the available techniques for the investigation of the physiological and morphological changes of cells, electrochemical methods represent an interesting approach. Exploiting the electrical properties of biological samples, it is possible to perform real-time, label-free, non–destructive, quantitative analysis of cellular dynamics [5,6]. The use of techniques such as amperometry, voltammetry or impedance spectroscopy allow the detection of various changes in the cell culture, e.g. cell morphology, cell membrane integrity, receptor-ligand interactions or the detection of chemical compounds released after external stimuli [7,8]. Typically, cells are incubated on 2D electrodes, or in their proximity, and the most used electrode materials are usually gold and platinum. However, flat surfaces poorly mimic the *in vivo* environment, and the results obtained with these electrodes might be misleading and inaccurate [1]. For this reason many efforts have been put into the development of 3D scaffolds, in order to combine the more realistic environment for cells with the integrated sensor functionality [9‑11]. Conductive scaffolds obtained

from various materials, such as metal [12,13], conductive polymers [14] or carbon [15‑17], have been previously produced. However, the fabrication process is still challenging, especially in terms of reproducibility, resolution and high throughput. Various approaches have been employed to fabricate 2D and 3D electrodes, such as electroplating [18], sputtering or evaporation [19] and screen printing [20,21]. Moreover, metal electrodes have a limited electrochemical potential window and can be easily affected by fouling [20,22,23]. In the last decades, to overcome these drawbacks, carbonaceous materials have emerged as valid option for the fabrication of electrodes. Various studies reported the use of electrodes obtained using graphene [24], carbon nanotubes [25], diamond-like carbon [26], carbon composites [27] and pyrolytic carbon.

Micro- and nanofabrication methods allowed the use of microelectrodes in different fields, enabling the miniaturization of analytical systems. The main advantages of these systems consist in reduced consumption of sample and reagents, lower fabrication costs, shorter response time and increased sensitivity [28,29]. In particular the carbon MEMS technique is used to fabricate pyrolytic carbon electrodes starting from a polymer precursor [30,31]. The process consists in the heat treatment of lithographically patterned photoresists at high temperature (above 900°C) in inert atmosphere. This technique is simple, highly reproducible and allows the customization of the final electrode design. The resulting pyrolytic carbon is structurally similar to glassy carbon and its advantageous electrochemical properties include wide electrochemical potential window [32], chemical inertness [33] and biocompatibility [34]. For these reasons, pyrolytic carbon electrodes have been used for different applications, such as for example the fabrication of micro-batteries [35,36], biosensors [37‑39] and cell culturing and differentiation studies [40]. The fabrication process allows tailoring the final properties of the electrodes, in terms of design and electrical and electrochemical properties. For example, depending on the polymer precursor and pyrolysis conditions the resistivity and the electrochemical behaviour can be tuned [41]. Hence, pyrolytic carbon electrodes represent a platform which depending on the application offers a high degree of freedom in the customization of the required properties.

1.2 Scope of the thesis

This Ph.D. project was part of the Young Investigator program funded by the Villum foundation. The project team was formed by two Ph.D. students (S. Hemanth and me) and one Postdoc (C. Caviglia). The project aimed at the development of a new generation of 3D cells scaffold with optimized properties for cell culturing and *in situ* electroanalysis of cell cultures. This was achieved through:

- advances in the fabrication of 3D carbon microelectrodes, in particular in the patterning of the polymer precursors for the achievement of various structures (e.g. suspended layers)
- optimization of the pyrolysis process in terms of electrical/electrochemical properties and investigation of the influence of the polymer template on the properties of pyrolytic carbon electrodes
- integration of the 2D/3D pyrolytic carbon electrodes with cell cultures for the establishment of *in vitro* models for viability/cytotoxicity studies

The main goals of this multidisciplinary Ph.D. project were the investigation of the material properties of pyrolytic carbon, the optimization of the pyrolysis process and the use of the obtained electrodes for bioelectrochemical applications in collaboration with C. Caviglia. The electrodes were used for the development of a 3D model for the support of bone diseases research and for preliminary studies of pyrolytic carbon as anode material in biophotovoltaic cells.

The project can be divided into three main parts:

1. **Pyrolysis process optimization:** Even if the C-MEMS process is an established technique to obtain pyrolytic carbon, a systematic study of the pyrolysis process parameters at high temperature was lacking. Previous studies showed an influence of the pyrolysis conditions on the graphitic content and thus on the electrical/electrochemical properties of the electrodes. However only few authors showed experiments performed at 1100°C, due to the limitations of

quartz based furnaces. Exploiting the features of the new pyrolysis oven installed at the beginning of my project, different pyrolysis parameters were systematically investigated in order to obtain electrodes with low resistivity and improved electrochemical performance.

2. **Investigation of new polymer templates and carbon structures:** In order to investigate new polymer precursors various fabrication methods were employed such as spray coating and electrospinning. Unfortunately, due to lack of furnaces outside the cleanroom facilities of Danchip, SU-8 remained the main polymer precursor used to obtain pyrolytic carbon. To fabricate electrodes with various structures and increased surface area colloidal photolithography and etching were used.

3. **Bioelectrochemical applications:** 2D pyrolytic carbon electrodes were used for the first time in an electrochemical assay for *in situ* monitoring and quantification of the bone differentiation marker alkaline phosphatase (ALP) combined with real-time electrochemical impedance monitoring of osteogenic differentiation. Using the same electrochemical assay, 3D electrodes were used to monitor and quantify *in situ* the ALP activity of Saos-2 cells embedded within a gelatin hydrogel.

Moreover, modified 2D and 3D electrodes were integrated in miniaturized biological photovoltaic systems (BPVs) for the investigation of current generation from photosynthetic microorganisms (cyanobacteria).

1.3 Organization of the thesis

The thesis is divided into eight main chapters which describe the research work carried out during the past three years. **Chapter 2** focuses on the fabrication of pyrolytic carbon electrodes, giving an overview of the carbon materials, explaining the techniques used to pattern the polymer precursors and describing the pyrolysis process. **Chapter 3** gives an overview of the techniques used for the characterization of the electrodes, as well as **Chapter 4** which mainly focuses on the electrochemical methods. **Chapter 5** describes

the use of pyrolytic carbon electrodes for the monitoring of bone cells differentiation. The specific design used for the cell studies is introduced and described. After a short introduction to bone and bone diseases, an overview of the electrochemical techniques applied for cell studies is given, focusing on impedance spectroscopy. **Chapter 6** introduces the 3D electrodes, discusses their advantages and describes their application for the development of a 3D cell culture model. **Chapter 7** describes the use of 2D and 3D pyrolytic carbon electrodes in biophotovoltaic cells. **Chapter 8** summarises the main conclusions and presents some future perspectives of the work. **Appendix A** contains the publications and manuscripts achieved during the Ph.D., while **Appendix B** provides experimental and fabrication protocols employed during my project.

2. Pyrolytic carbon electrode fabrication

This chapter provides a description of the structural properties of different carbon allotropes. The interesting and advantageous properties of carbon materials for electrochemical applications are described. Then, the structure of pyrolytic carbon is introduced and the different parameters affecting the pyrolysis process are discussed. The statistical method Design of Experiments is introduced and its use in the optimization of the pyrolysis process is explained. In conclusion, the techniques used to obtain pyrolytic carbon electrodes are presented, providing a description of the fabrication processes used.

2.1 Carbon allotropes and properties

Carbon (C) is the main element providing basis for life on earth. The ability to interact and combine with almost all elements gives carbon the possibility to form organic molecules and compounds with extraordinary structural diversity and a broad range of physical and chemical properties [42]. This is mainly due to the different types of bonds carbon atoms can form which is related to the different types of hybridization: sp^1, sp^2 and sp^3. Carbon is therefore available in different allotropes such as diamond, graphite, fullerene, graphene, carbon nanotubes, amorphous carbon and glassy carbon [43,44]. Depending on the inherent structure, surface bonds and functional groups, some of these carbon allotropes can be used as electrode materials for electrochemistry (Figure 2.1) [22,45].

Diamond is composed of sp^3 hybridized carbon atoms and is characterized by its hardness which originates from the strong covalent bond between the carbon atoms (C-C bond length of 1.54 Å). Its electrical conductivity is low, but can be improved by doping with materials such as nitrogen and boron [46]. Graphite has a planar structure characterized by different layers held together by van der Waals forces. Each of these layers is characterized by sp^2 hybridized carbon atoms arranged in a hexagonal lattice.

The distance between planes is 3.35 Å, with a lattice parameter of 1.42 Å [47]. It is one of the softest materials (hardness on the Mohs scale of 1), but has a good conductivity. In particular, randomly oriented graphite has a resistivity of 1×10^{-3} $\Omega\cdot$cm, while highly oriented pyrolytic graphite has a resistivity of 4×10^{-5} $\Omega\cdot$cm in the basal plane (a-axis) [22]. Fullerenes are a family of carbon allotropes which comprehend different structures such as the spherical fullerene (buckyball) and carbon nanotubes. Among these structures, carbon nanotubes have been used as electrode material [22,24,48,49]. They consist of single (SWCNTs) or multiple (MWCNTs) graphene sheets rolled up to form tubes with diameters of nanometers and different lengths [50].
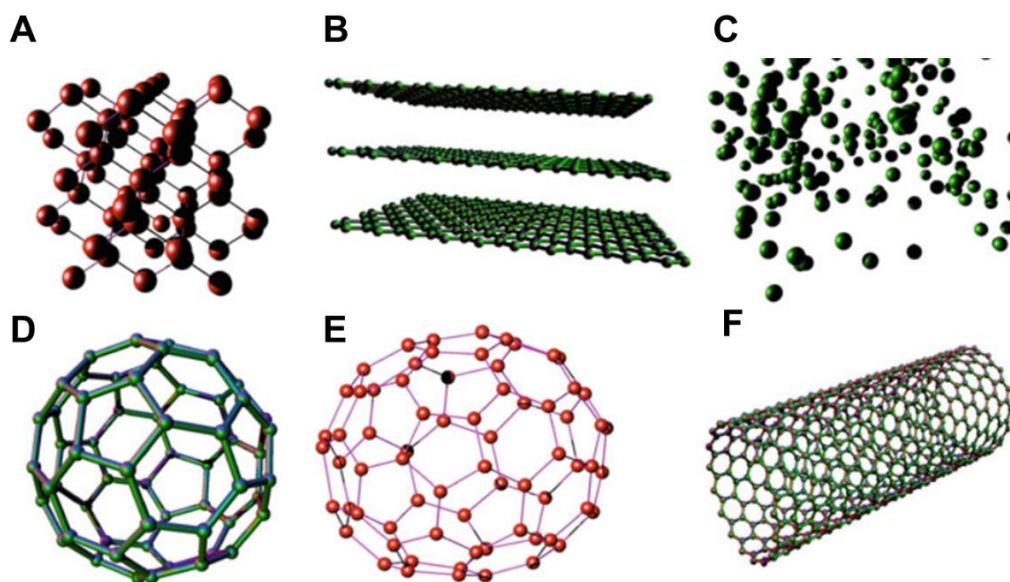
Figure 2.1: Allotropes of carbon: diamond (A), graphite (B), amorphous carbon (C), spherical fullerene C_{60} (D), Ellipsoidal fullerene C_{70} (E), single wall carbon nanotube (SWCNT) (F). Figure reproduced from [50].

Amorphous carbon is an allotrope in which carbon atoms are arranged in an irregular state without a crystalline macrostructure. In this case, short range order is present, but not comparable to diamond or graphite lattices.

Glassy carbon (GC), has a structure composed of both graphitic (sp^2 C-C bonds) and amorphous zones (sp^3 C-C bonds) [44,45,51]. It is derived from the thermal degradation of organic polymers such as polyacryonitrile, phenol/formaldehyde resins or furfuryl alcohol at 1000-3000 °C in an inert atmosphere. The structure of glassy carbon has been

at the centre of many discussions[51]. In 1971 Jenkins et al. introduced a model which described glassy carbon as a tangled and wrinkled aromatic ribbon of molecules held together by C-C covalent bonds (Figure 2.2A) [52]. Currently the most accepted theory is that GC is formed by graphitic planes with limited sizes, leading to a structure with ribbons of graphitic planes randomly intertwined [22]. Harris hypothesized that GC has a fullerene-related structure, with sp^2 hybridized carbons, and that different degradation temperatures lead to different amount of graphene sheets and thus different levels of microstructural disorder (Figure 2.2B and C) [51].
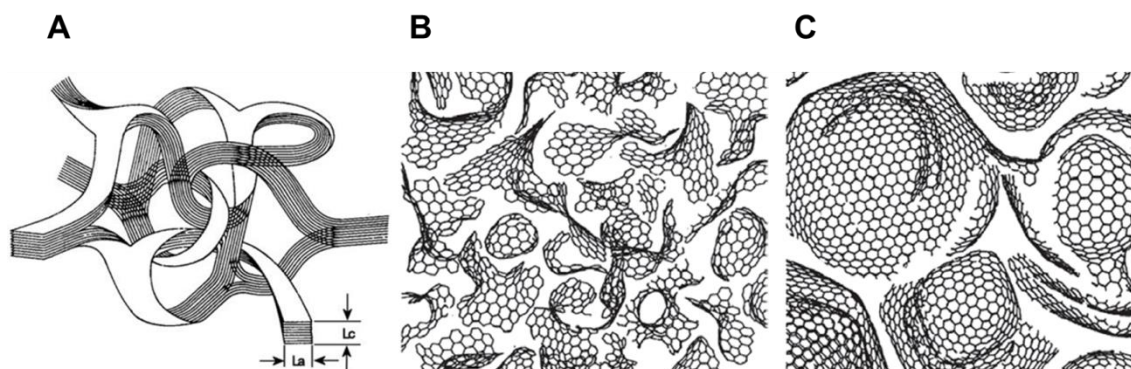
Figure 2.2: The Jenkins–Kawamura model of glassy carbon. L_a and L_c represent the lengths of the graphitic domains (A). Structure proposed for glass-like carbon obtained at low temperature (C) and high temperature (D). Figure reproduced from [52] and [51].

GC has a high chemical resistance towards strong acids, is impermeable to gases and is extremely inert. It has good mechanical properties, with a hardness of approximately 7 on the Mohs scale and a Young´s modulus in the range of 10-40 GPa. Glass-like carbon has a reported electrical resistivity $\sim 5 \times 10^{-3}$ $\Omega \cdot cm$ [53,54]. Due to these physical and chemical properties, glassy carbon has been widely employed as electrode material [22,54,55].

Due to their favourable chemical and physical characteristics carbon materials have been extensively investigated and used as electrodes for electrochemical applications. They have a wide electrochemical potential window, an electrocatalytic activity for many redox reactions, chemical inertness and low fabrications costs [22,45]. They have been used for different applications such as electrocatalysis studies, electroanalysis,

energy conversion and storage and enzymatic sensors [37,56‑60]. Most carbon electrodes are obtained from bulk materials such as glassy carbon or graphite, which are then shaped in order to expose the electrochemically active surface [22].

2.2 Pyrolytic carbon electrodes

A new class of carbon electrodes with interesting properties being structurally and electrochemically similar to glassy carbon is represented by pyrolyzed photoresists. In particular, phenol formaldehyde resins have been used to fabricate carbon structures with micro and nano dimensions through pyrolysis [61,62]. By pyrolyzing lithographically patterned photoresists it possible to obtain carbon electrodes with customized designs and well-defined geometries using a process that is simple and highly reproducible. As mentioned before, the structure of the resulting pyrolytic carbon is similar to GC, with graphitic and amorphous zones [30,31,45,63]. Microfabricated structures produced with this process were reported at the of the end 1990s, when Schueller *et al.* reported the use of PDMS moulds for the patterning of furfuryl alcohol-modified phenolic resins and phenol-formaldehyde resins and their subsequent carbonization [64]. Various studies on the electrochemical properties of carbon derived from positive photoresists were carried out, showing the near-atomic flatness of the obtained pyrolytic carbon [63,65]. SU-8, a negative photoresist, has been extensively used to fabricate both 2D and 3D carbon structures with high aspect ratios [35,66,67]. In general, carbon electrodes derived from pyrolyzed photoresists have been used for different applications such as fuel cells, lithium ion batteries, cell culturing substrates, dielectrophoresis and pathogen detection [34‑36,40,68‑71]. Depending on the pyrolysis conditions, the electrical and electrochemical properties of the pyrolytic carbon can vary due to the change in the graphitic content [41,63,71‑73].

2.3 Pyrolysis

2.3.1 Pyrolysis process

Pyrolysis is a thermal degradation process of materials performed at high temperature in an inert atmosphere. Glass-like pyrolytic carbon can be obtained through the pyrolysis of organic polymer photoresists. The process includes many reactions taking place at the same time: hydrogen transfer, isomerization, dehydrogenation and condensation. More generally, the pyrolysis of thermosetting resins can be divided into three steps (Figure 2.3) [74]:

- Pre-carbonization (T<300°C): Molecules of unreacted monomers and of solvent are removed from the polymer precursor.

- Carbonization (300°C <T<1200°C): Until 500°C halogens and heteroatoms such as oxygen are eliminated due to the rapid loss of mass. At the same time a network of conjugate carbon atoms forms. From 500°C to 1200°C nitrogen, hydrogen and more oxygen atoms are removed and the carbon network becomes interconnected.

- Annealing (T>1200°C): Sulphur and the remaining impurities are removed. The final pyrolysis temperature has a major importance on the degree of carbonization and level of residual impurities.
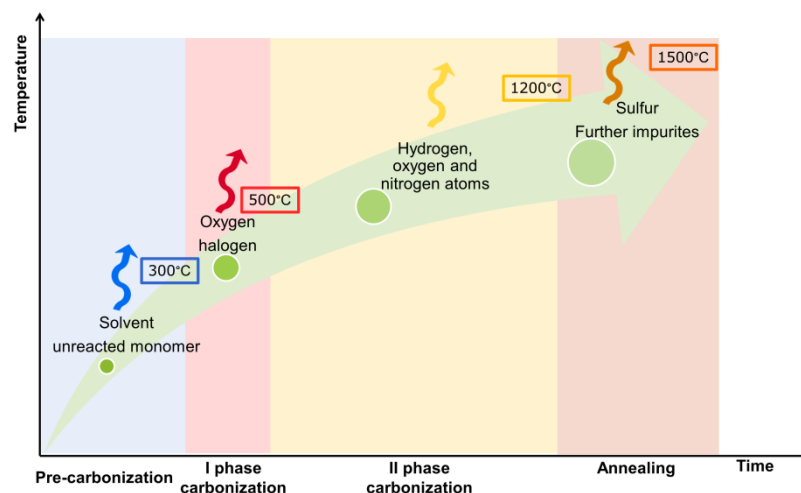
Figure 2.3: Schematic representation of the carbonization processes taking place during pyrolysis.

The parameters which can be changed during the pyrolysis process include the maximum pyrolysis temperature, the number of steps in the process, heating rate, dwell time at the maximum temperature and gas composition inside the furnace (Figure 2.4). In the following sections the different parameters will be introduced and discussed.
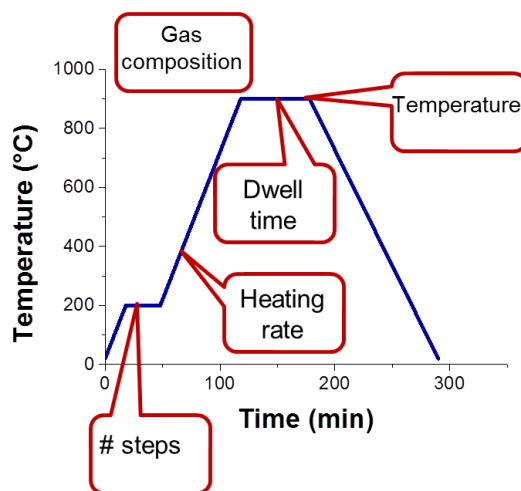
Figure 2.4: Schematic representation of a typical pyrolysis process and pyrolysis parameters.

2.3.2 Polymer precursors

The polymer precursor has a major influence on the properties of the obtained pyrolytic carbon. Polymers such as polyfurfuryl alcohols, polyvinyl chloride, cellulose, silk protein, polyimides and phenolic resins have been previously pyrolyzed in an inert atmosphere [30,72,75‑78]. Depending on the precursor used, different carbon yield and shrinkage degrees are obtained. However not all polymers are suitable for pyrolysis, and depending on the precursor the process may occur in three ways [74]. In the first case, the polymeric chain may degrade into small fragments and vaporize as H_2, CO_2 and CO together with other hydrocarbons. This happens for example for polyethylene. In the second case, polymers like polyvinylidene chloride form aromatic molecules, which may stack and form a lamellar plastic phase. Upon heating above 2700°C this phase forms graphitic regions. Finally, in the case of thermosetting polymers, the polymer chain may form a conjugated carbon structure without going through a fluid state. They release hydrogen and other heteroatoms and maintain the shape with a shrinkage from

50 to 90% [31,63]. The final glass-like carbon obtained does not graphitize when further heated to 3000°C [44].

In this work the negative epoxy-based photoresist SU-8 has been used as the main carbon precursor to fabricate pyrolytic carbon electrodes. However, in parallel other polymers have been investigated for the formation of glassy carbon in collaboration with Maxime Durocher, an internship student from the Grenoble institute of technology (Grenoble INP–PHELMA): Poly(vinylpyrrolidone) (PVP), Ethyl cellulose and EUDRAGIT ®, a commercial poly(meth)acrylate-based polymer. These polymers were deposited by spray coating on a substrate with 5µm SU-8. This was done in order to offer the different polymers anchoring points to the substrate during the pyrolysis process, as previously done in a study by Amato *et al.* [79].
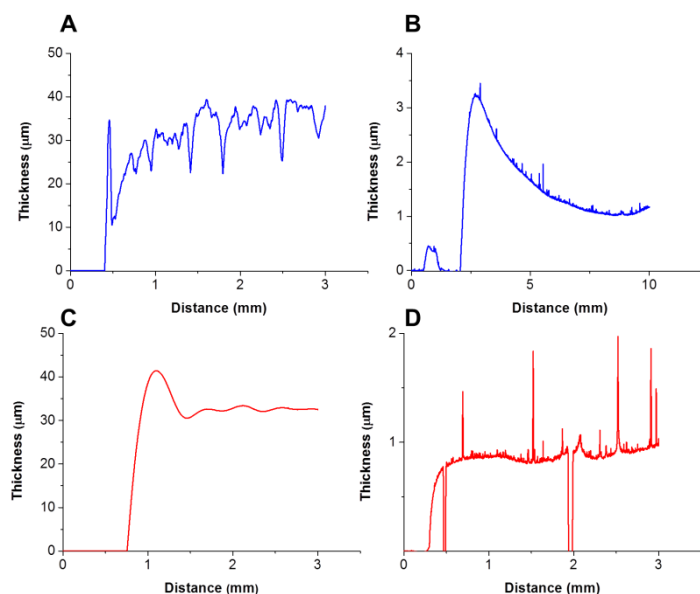
Figure 2.5: Thickness profile of EUDRAGIT before (A) and after (B) pyrolysis, and of PVP before (C) and after (D) pyrolysis on SU-8 layer.

The main result was that using spray coating it was possible to obtain uniform polymer films which after pyrolysis led to a conductive carbon layer (Figure 2.5). However, only PVP and EUDRAGIT ® exhibited a uniform layer, while ethyl cellulose displayed cracks after pyrolysis. As expected all the samples after pyrolysis shrank more than 90% (Table 2.1). Electrochemically, the addition of the various polymers did not

improve the performance when compared with the electrode obtained from the pyrolysis of SU-8 (chapter 4). For this reason, the work focused on SU-8 for most of the thesis.

Table 2.1: Thickness of precursor polymers investigated in this project before and after pyrolysis

Polymers	Thickness before pyrolysis	Thickness after pyrolysis
Eudragid	35.5 μm	1 μm
PVP	32.7 μm	0.93 μm
Ethyl cellulose	37.6 μm	0.3 μm
SU-8	16.5 μm	1.9 μm

2.3.3 Pyrolysis temperature

It has been shown that pyrolysis processes performed with higher temperatures lead to pyrolytic carbon with better electrochemical performance and improved conductivity [30,41,63]. The final temperature determines the level of carbonization and the amount of residual elements present in the final pyrolytic carbon. This is due to the fact that higher temperatures lead to higher shrinkage and increased level of graphitization [63]. Photoresists are typically pyrolyzed using a heat treatment at 900°C in an inert atmosphere. The temperature is often set to this value due to limitation in the temperatures reachable by some quartz-based furnaces. In this work I thoroughly investigated the pyrolysis of SU-8 at 1100°C, and studied the influence of various pyrolysis parameters at this temperature (Paper II).

2.3.4 Gas composition

The atmosphere inside the furnace during pyrolysis has an influence on the characteristics of the final pyrolytic carbon. In particular, the oxygen/carbon ratio on the surface of the carbon be varied [31]. The inert atmospheres usually used are: N_2, H_2, vacuum or forming gas. Processes run in vacuum and forming gas lead to pyrolytic carbon with lower oxygen content on the carbon surface. In this work, the influence of different atmospheres on the electrical and electrochemical performances was investigated (Paper I). No relevant differences were observed for processes run at 900°C

with N_2, H_2, vacuum or 50% N_2+50% H_2. However electrodes prepared in vacuum showed delamination, probably due to the more prominent outgassing during pyrolysis [32]. For these reasons, all the experiments were performed in N_2 atmosphere.

2.3.5 Heating rate

Typically the pyrolysis of patterned photoresists is carried out with a temperature ramp-up of 10°C/min and one hour dwell time[41]. Previous studies suggested that higher heating rates (above 25°C/min) led to pyrolytic carbon with an increased porosity [41,80]. Slower heating rates should in fact allow more time to the photoresist to release internal gases such as oxygen and hydrogen and consequently lead to the formation of pyrolytic carbon with a smooth surface [53]. Higher temperature would not allow this controlled gas release and therefore induce the formation of bubbles on the surface containing unreleased gases [80]. In this work three different heating rates were explored: 10°C/min, 30°C/min, 50°C/min (Paper II). The conclusion of this study was that the fastest heating rate of 50°C/min produced a surface that was just slightly rougher compared to the one obtained with slower heating rates. This heating rate also led to higher shrinkage values, probably due to the limited time available for the rearrangement of C atoms during the heating step.

2.3.7 Dwell time

The influence of dwell time for pyrolysis processes carried out at 1100°C was investigated. Previous studies performed at 900°C reported a decrease in terms of resistivity values when dwell time was increased, with the lowest resistivity value measured for a process with 4 hours dwell time [41]. In this work three different dwell times were chosen: 1 hour, 3 hours and 5 hours. The same trend was observed when the time was increased. This could be explained by the fact that longer dwell times may allow more time for the rearrangement of carbon atoms and the subsequent formation of larger or differently oriented graphitic areas [41,51].

14

2.3.8 Number of temperature steps

Typically pyrolytic carbon is obtained with a two-step process, with an intermediate temperature step around 200°C [41]. This is usually done to release residual tensile stresses in the SU-8 film and avoid delamination [32]. In this work, a one-step pyrolysis process was used since no delamination was observed. Moreover, in terms of resistivity the use of a one step process did not influence the resistivity when compared with the two-step process ($9 \cdot 10^{-3}$ $\Omega \cdot$cm and $10 \cdot 10^{-3}$ $\Omega \cdot$cm respectively).

2.4 Design of experiments

Pyrolysis is a complex process which has many parameters that can influence the electrical and electrochemical characteristics of pyrolytic carbon. During the optimization of this process the experiments were performed following the statistical approach called Design of Experiments (DoE) [81]. This approach refers to the procedure of planning experiments in order to appropriately collect data and analyse them by statistical methods obtaining a valid and objective conclusion [82]. When dealing with an experimental problem the key aspects are the design of the experiment itself and the statistical analysis of the acquired data. The core principles of the experimental design proposed by Fisher are: randomization, replication and blocking. Randomization consists in the random assignment of the order in which individual experiments are executed. If random assignment is used, then a correlation implies causation [83]. This helps to identify effects which depend on extraneous factors. Replication is obtained by performing replicate runs in a systematic manor of each chosen factor combination. This allows to estimate the experimental error and to obtain more reliable estimates of a certain parameter. Finally, blocking is a design technique which requires a set of homogeneous experimental conditions. It increases the precision with which comparisons between different factors are done and reduces the variability due to factors which may influence the experiments but are not of direct interest.

Since the final aim was the optimization of the pyrolysis process, the response surface methodology (RSM) was used (Figure 2.6). This technique is useful when the focus is the modelling and analysis of a problem in which a response is influenced by a series of variables and the objective is to optimize this response. Response surface methodology is a sequential procedure which uses successive steps to find the region of the optimum. Once this region has been located, a more elaborate model can be used to perform the analysis to find the optimum. When the relationship between the response y and the independent variables $[x_1, x_2, ..., x_k]$ is unknown, a first step towards finding a relationship between them consists in a screening experiment in some region of the independent variables using a first-order polynomial to analyse the data. If the linear function which models the response is satisfactory (measured by a goodness-of-fit measure, such as R^2), then the first-order model represents the approximating function:

$$y = \beta + \alpha_1 x_1 + \alpha_2 x_2 + \cdots + \alpha_k x_k + \epsilon \qquad \text{Equation 2.1}$$

where β is the intercept, the parameters α_j, j=1,…,k, are the regression coefficients and ϵ represents the error term [84]. In the case where there is a curvature in the system, then a second-order model must be used:

$$y = \beta_0 + \sum_{i=1}^{k} \alpha_1 x_1 + \sum_{i=1}^{k} \alpha_{ii} x_i^2 + \sum \sum_{i<j} \alpha_{ij} x_i x_j + \epsilon \qquad \text{Equation 2.2}$$

To estimate the parameters of the approximating function, the method of least squares is used and the fitted surface is employed to perform the response surface analysis. The least squares method estimates the values of α´s which minimize the sum of squares of the model errors. To have a more effective estimation of the model parameters the data must be collected using specific designs to fit the response surfaces.
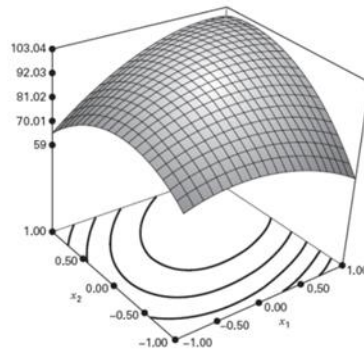
Figure 2.6: Response surface illustrating a surface with a maximum. Figure reproduced from [82].

In the specific case of the pyrolysis process optimization a central composite design (CCD) was used. This is a class of designs which is used to fit second-order models. For k factors it requires 2^k factorial runs, $2k$ axial runs and at least one center point n_c. The main feature of CCDs is that they are rotatable, meaning that the variance of the parameter estimates is the same for all points that are at the same distance from the design centre. This means that this design provides equal precision of estimation in all directions [82]. The difference between various central composite designs is determined by the choice of two parameters: α, which is the distance of the axial run from the design centre, and n_c (Figure 2.7).
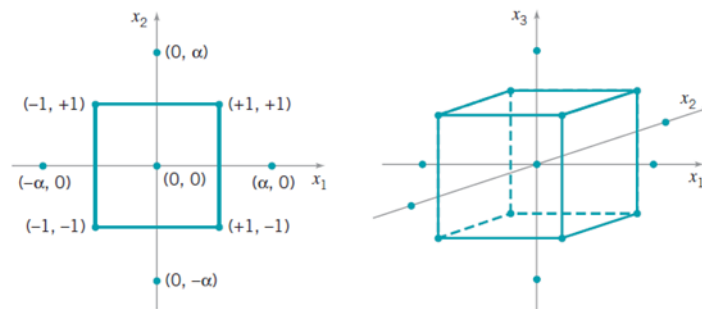
Figure 2.7: Central composite designs for $k = 2$ and $k = 3$. Figure reproduced from [84].

In this work a face centered central composite design ($\alpha=1$) was used. The chosen parameters for the design were the dwell time at the maximum pyrolysis temperature (t) and the heating rate (h) (Paper II). 10 experimental runs were performed (2 center points) and SAS JMP software was used to analyse the results. The responses measured

were resistivity and thickness, and in terms of electrochemical properties, peak potential separation and anodic peak current. Table 2.2 reports the P-values and the coefficients of determination adjusted R^2. Terms statistically significant exhibited P-values lower than 0.05.

Table 2.2: P-values of the DoE fit and R^2 values . The four measured responses were resistivity, peak current, potential difference between the oxidation and reduction peaks ΔEp and thickness after pyrolysis. Factors included in the model were time (t) and heating rate (h).

	t	*h*	*t*h*	*t²*	*h²*	*R²*
Resistivity	*0.04*	0.85	0.39	0.46	1.00	0.36
Peak current	0.09	0.88	0.78	0.99	0.25	0.19
ΔEp	*0.05*	0.62	0.40	0.45	*0.04*	0.62
Thickness	0.56	*0.0003*	0.87	0.44	0.26	0.94

2.5 2D carbon electrode fabrication

2.5.1 Chip design

2D electrode chips with a three electrode configuration and pyrolytic carbon working electrode (WE) were designed and fabricated. Based on a previous optimization study performed in our group, the optimal chip design in terms of carbon leads width and length was chosen [85]. The chips consist of a circular carbon WE with an area of 12.5 mm^2, a counter electrode (CE) with an area of 25.2 mm^2 and an Au reference electrode (RE) with and area of 0.8 mm^2 (Figure 2.8). The detailed process parameters are reported in Paper I and Paper II.
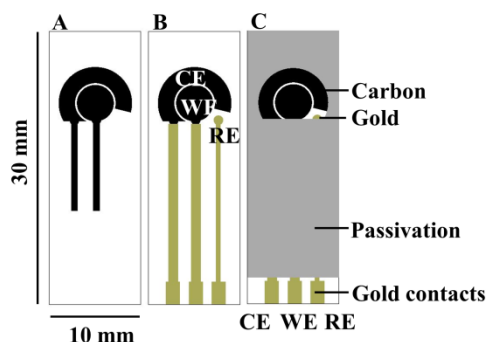
Figure 2.8: Overview of 2D carbon electrodes: carbon layer (A), gold contact leads and pads (B), SU-8 passivation layer (C).

The chip dimensions of 10mm×30mm were chosen to be similar to the commercially available Dropsens electrodes, and hence facilitate the interfacing with the potentiostat. The electrodes were used to investigate the electrochemical properties of pyrolytic carbon, optimize the pyrolysis process and to investigate ways to increase the WE surface area. In following sections the four different fabrication methods used to obtain the electrodes will be discussed. In particular, the colloidal templating, etching and colloidal lithography processes were developed in collaboration with Sebastiano Camelia for his master thesis project supervised by me [86].

2.5.2 Standard UV photolithography

UV photolithography consists in the transfer of a pattern on a substrate using ultraviolet light (360-410 nm). A mask is used to perform the pattern transfer onto the photoresist, a photosensitive polymeric material [87,88]. This technique is widely used in the integrated circuit (IC) industry and in the fabrication of microelectromechanical systems (MEMS). Generally, photolithography involves a series of steps: photoresist deposition, soft bake, exposure, post exposure treatment and development.

Photoresists represent a key factor in the fabrication process and have an influence on the quality and properties of the obtained structures. They are usually deposited through spin coating, and there are various commercially available photoresists. They are composed of a polymer (base resin), a solvent which enables the spin coating and a sensitizer (photoinitiator) which controls the chemical reaction in the polymer. Resists

which have all these components are called two-components systems [44]. Depending on the chemical composition photoresists react differently when exposed to UV light. Positive photoresists are weakened when exposed to light by rupture or scission of the main and side polymer chains, making the exposed part soluble in the developing solution. For negative photoresists, the exposed part crosslinks due to the photochemical reaction, making it less soluble.

In this study the negative epoxy-based photoresist SU-8 has been used to fabricate the pyrolytic carbon electrodes. SU-8 was developed by IBM, and it is mainly composed by the bisphenol-A novolac resin (EPON® SU-8 resin, Shell Chemical Company [89]). This resin is dissolved in an organic solvent (propylene glycol methyl ether acetate (PGMEA), gammabutyrolactone (GBL) or cyclopentanone) with up to 10% in weight of a photoacid generator (triarylsulfonium hexafluroantimonate salt). When SU-8 is exposed to UV light, the photoacid generator decomposes and forms an acid which starts and catalyses a series of crosslinking reactions [88]. The chemical structure of the epoxy oligomer contained in the SU-8 formulations has on average eight reactive epoxy sites, making the fully crosslinked SU-8 mechanically and thermally stable (Figure 2.9) [88]. Due to the low UV adsorption and to its low molecular weight (~7000 Da), SU-8 can be used to deposit thick films up to 500 μm in one coat and obtain lithographically patterned structures with high resolution [90].
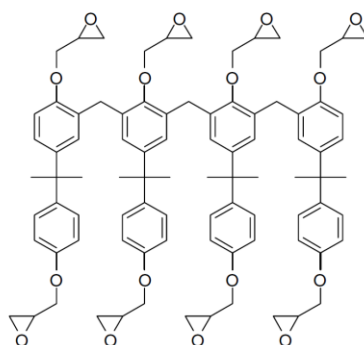

Figure 2.9: Chemical structure of bisphenol A novolak contained in SU-8. Figure reproduced from [88].

In the first step of the fabrication process, the carrier wafers were cleaned and subsequently dried by performing a process called RCA cleaning which uses H_2O,

20

NH$_4$OH, H$_2$O$_2$, HF and HCl at different stages. Then, 600 nm Si oxide were grown by wet oxidation and 17 μm of SU-8 were spin coated. The wafers were then placed on a hot plate for soft baking. This step is necessary to let the solvent evaporate before the exposure step [88]. The photoresist was then lithographically patterned and a post-exposure bake was performed to ensure the crosslinking of the photoresist. The non-exposed parts were removed in the development step with PGMEA. After a flood exposure step, the wafers were hard-baked to complete the crosslinking process and stabilize the exposed areas [32,88]. Finally, the wafers were placed in a furnace and pyrolyzed. The optimized pyrolysis process used after the study on the influence of the different pyrolysis parameters was 5 hours at 1100°C with a heating rate of 10°C/min. To define the contact leads and pads, an adhesion layer of chromium or titanium (10 nm) and a layer of gold (200nm) were deposited by e-beam evaporation through a shadow mask. A second photolithography step was used to pattern the 5µm passivation layer for the 2D electrode chips (Figure 2.10).
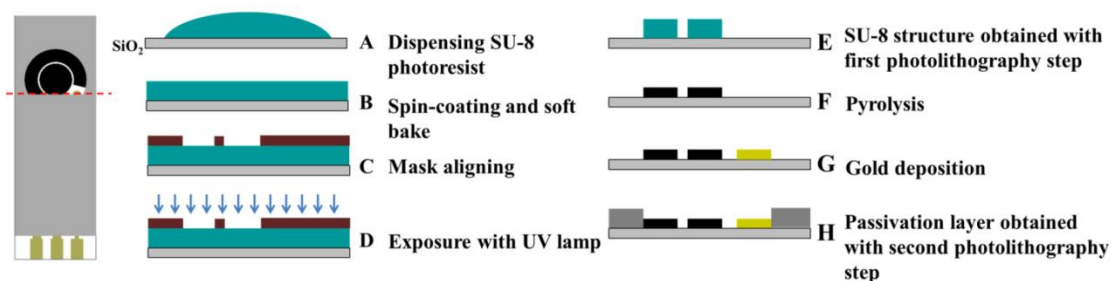
Figure 2.10: Process flow for the fabrication of pyrolytic carbon electrodes with standard UV photolithography.

2.5.3 Colloidal templating

In order to increase the area of the working electrode and achieve a porous 3D structure, a soft templating approach was used as additional step compared to the standard UV photolithography process. Polymer templates have been used previously to obtain porous carbon monoliths (Figure 2.11) [91‑94]. The most commonly used colloids are polystyrene (PS) and poly(methyl methacrylate) (PMMA) [93]. This technique allows

the fabrication of porous carbon monolith by using polymer colloids as soft template [93].
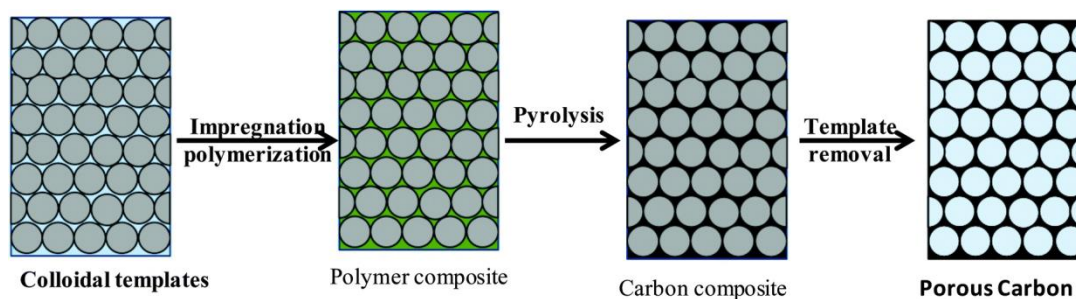
Figure 2.11: Schematic representation of ordered porous carbon-based materials obtained using PS or silica-based templates. Figure reproduced from [93].

Monodispersed spheres are assembled into periodic arrays and the void spaces are infiltrated with the precursor solution for carbon. The polymer spheres are subsequently removed simply through washing using a suitable solvent (e.g. toluene) or simultaneously by decomposition during the thermal treatment.

Gravitational settling can be used to form close packed array of polymer beads and obtain a colloidal template. When carbon precursors impregnate the template and are polymerized and pyrolyzed, porous carbon materials can be fabricated [93,95,96].

Gates *et al*. used PS beads to fabricate a 3D porous membrane. The beads were injected in a cell and collected between two glass surfaces. After the elimination of the aqueous solvent a UV polymer was introduced in the chamber to fill the voids left by the evaporated solvent. After the crosslinking of the polymer and the dissolution of the beads a three-dimensional membrane with well-defined structures was produced [97]. Other studies obtained a porous carbon membrane by dispensing silica spheres in SU-8. The photoresist was subsequently exposed to UV light and pyrolyzed and the silica spheres were selectively removed [98]. The main advantage of using polymer templates instead of hard templates such as silica beads is that soft templates can be removed by thermal decomposition during the pyrolysis process without any additional etching step.

The idea was to integrate the polymer bead deposition into the process flow for the fabrication of 2D pyrolytic carbon electrodes described in section 2.5.2. The design of the electrode chip was changed, with CE, RE and contact leads made in Pt, a suitable

material as CE and pseudo-RE [99]. This was done in order to keep the fabrication process simple and confine the templating only on the WE, which represents the electrode of interest where the electrochemical reactions take place. The templating step was added just before the pyrolysis step. PS beads with two different sizes (10 µm and 150 µm, Sigma Aldrich [100]) were used to define the template (Figure 2.12). 50 µL of a solution containing beads suspended in water were pipetted on the working electrode using a PDMS shadow mask. After water evaporation, SU-8 2005 was poured on top of the PS beads and UV photolithography was used to crosslink the resist. A two-step process was used to pyrolyze the electrodes in N_2: 30 min at 250°C and 1 hour at 900°C with a heating rate of 2°C/min. These parameters were chosen in order to allow enough time for the thermal decomposition of the PS beads. 20nm of Ti adhesion layer and 100 nm of Pt were deposited using e-beam evaporation. The passivation layer was fabricated with the same parameters used for the 2D electrode fabrication described previously.
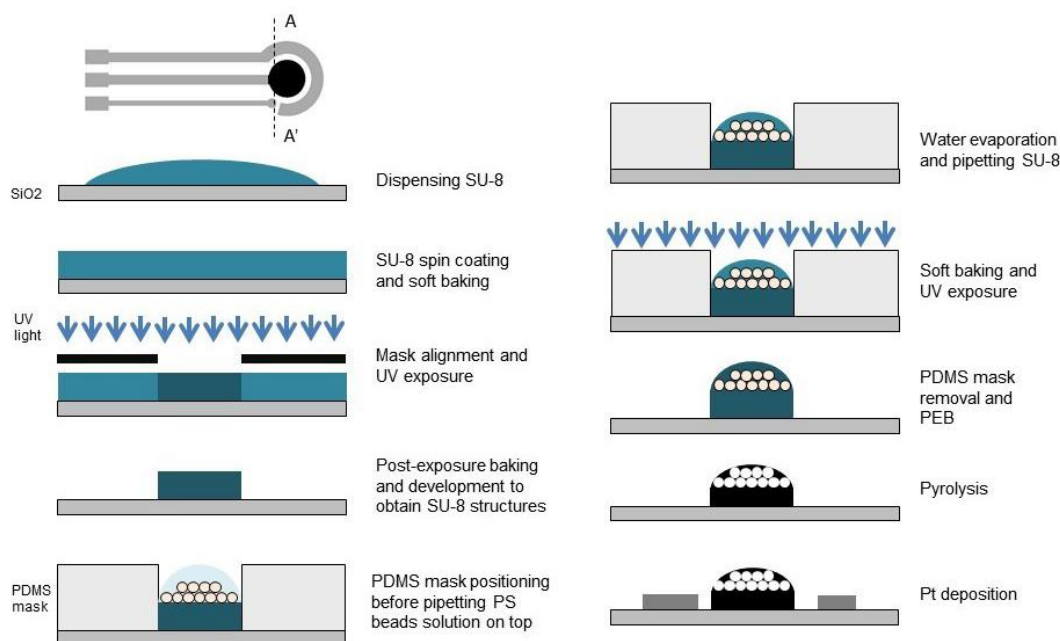
Figure 2.12: Process flow for the fabrication of porous pyrolytic carbon electrodes using colloidal templating.

As it can be seen in Figure 2.13, the manual deposition of the beads was difficult to control and not perfectly reproducible. Nonetheless, it was possible to let SU-8 impregnate and fill the voids between the beads.
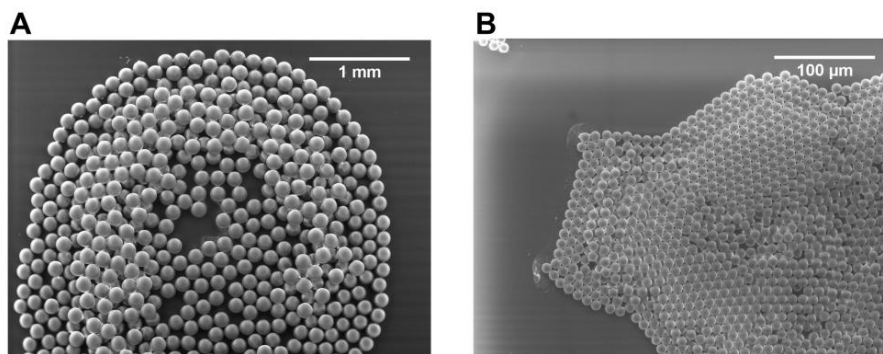
Figure 2.13: SEM images of the PS beads with a diameter of 150 µm (A) and 10 µm (B) deposited on the top of the SU-8 substrate.

During pyrolysis the polymer beads degraded and left empty voids in the pyrolytic carbon (Figure 2.14). However, after pyrolysis the surface of the WE showed major cracks, leading to a non-uniform pyrolytic carbon layer. This could be explained by the violent evaporation of the PS beads during the pyrolysis which probably occurs too fast to leave the SU-8 thin film smooth. Figure 2.14B shows a detail of one of the holes left by the evaporation of the PS beads. As it can be seen, the small holes represent the effect of the volatilization of the degradation products of PS, represented principally by gaseous styrene [101].
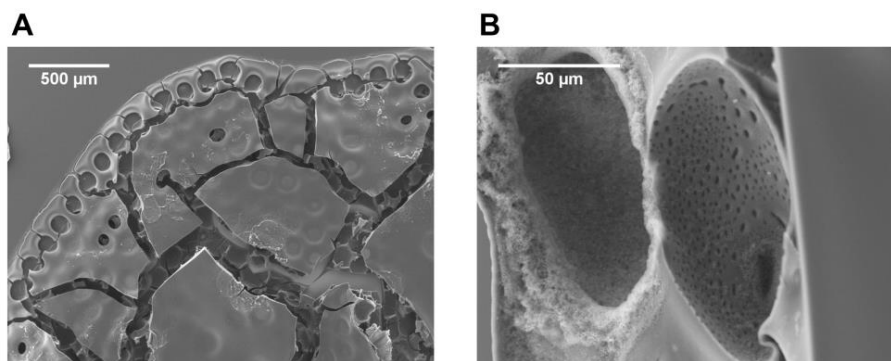
Figure 2.14: SEM images of the WE after pyrolysis: the empty spaces left due to the volatilization of the PS beads (A) and detail of the pores left by the PS beads with a diameter of 150 µm (B).

Unfortunately it was not possible to perform any electrochemical characterization on these electrodes due to the delamination of the working electrode. A possible explanation for this fact could be the non-uniform adhesion between the SU-8 used to fill the voids between the beads and the crosslinked SU-8 layer underneath.

2.5.4 Etching

In another attempt to order to obtain rough surfaces and increase the surface area of the WE, inductively coupled plasma reactive ion etching (ICP-RIE) was used before the pyrolysis of the SU-8 structures (Figure 2.15). With this particular technique it is possible to control separately the potential which generates the plasma and the one which is used to accelerate the ions towards the surface. In the ICP chamber a coil is positioned in the upper part of the chamber with an RF generator connected to it. The plasma is generated by introducing one or more gases into the plasma chamber, and when the RF potential is applied the electrons start to oscillate. Plasma consisting of electrons, neutral atoms and ions is created. The plasma generated does not have a preferred direction until the RF generator connected to the plate where the substrate is located attracts the ions from the plasma in order to etch the surface [102].

De Volder *et al.* showed that using plasma etching it was possible to produce nanowires in SU-8 [103]. In the described process, the accumulation at the surface of antimony contained in the SU-8 acted as local mask agent during the oxygen plasma etch and induced the formation of nanowires.

The influence of the various etching parameters on SU-8 roughness has been studied in a previous work [104]. In order to investigate the effect of the etching process on the final pyrolytic electrodes, different processes varying the time and the coil power were tested. The etching was performed at 20°C with an O_2 flow rate of 99 sccm, a pressure of 20 mTorr and platen power of 30 W. The time was varied between 15 and 30 minutes, while the coil power was varied between 1000 and 2000 W.
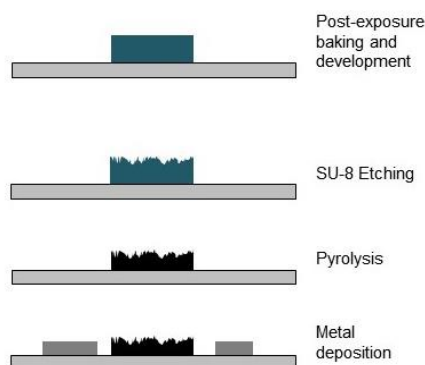
Figure 2.15: Process flow for the fabrication of pyrolytic carbon electrodes with rough surfaces using etching

Figure 2.16 shows the pyrolytic carbon surfaces. The etching process led to the formation of "nano grass" structures for all the processes performed. However the thickness of the remaining carbon film varied drastically depending on the process: when the etch time was set to 20 min and the power to 1000 W, the final height was ~1.3 µm, which is comparable with the height of 2 µm of the 2D flat carbon electrodes. On the contrary, for the process with t=30 min and power= 2000 µm, the final measured height was 0.2 µm. This could be explained taking into account the fact that longer and more powerful etching processes result in a more aggressive treatment on the SU-8 surface. The electrodes obtained with this fabrication technique did not delaminate and thus it was possible to continue with the electrochemical characterization, which will be discussed in chapter 4.
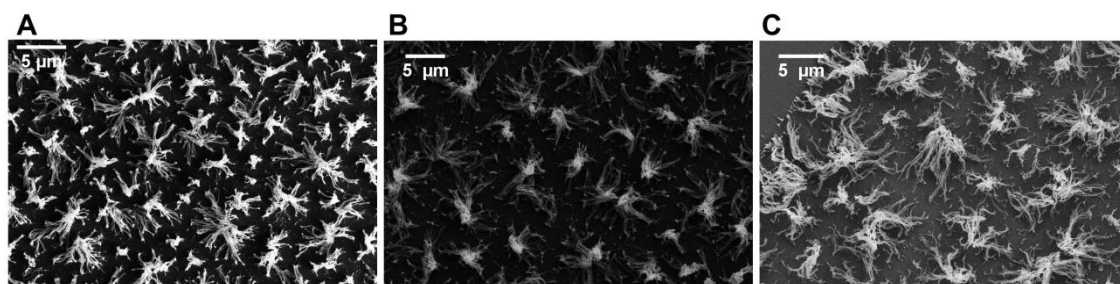
Figure 2.16: SEM images of three electrodes surfaces fabricated with different etching processes. Wafers fabricated with: (A) t=20min, power=1000W (B) t=15min, power=2000W and (C) t=30min, power=2000W.

2.5.5 Colloidal lithography

As final method to obtain an increased surface area on the WE, colloidal lithography technique was used. The deposition of the PS beads used for the colloidal templating has been used also in this case in order to obtain a layer of beads to use as mask during the anisotropic RIE etching process (Figure 2.17).
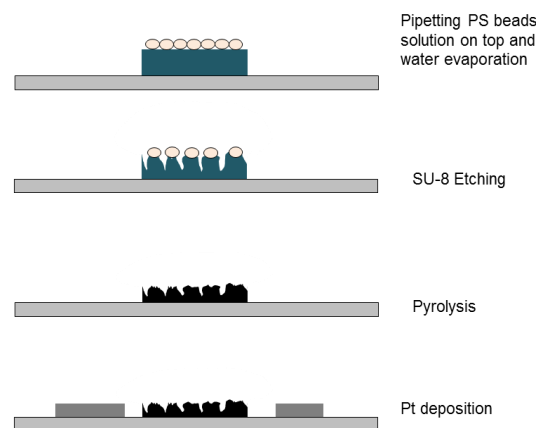
Figure 2.17: Process flow for the fabrication of porous pyrolytic carbon electrodes using colloidal lithography

This technique has been used previously to pattern for example polymer films or silicon surfaces [105‑107]. Basically, the layer of PS beads during the etching process protects the underneath SU-8 layer. In this way it is possible to achieve the formation of pillars with various diameters, depending on the size of the PS beads. Previous studies have used SU-8 and PS beads (diameter of 500 nm and 1µm) to obtain pillars using O_2 plasma treatment. By pyrolysing the structures, carbon nanopillar arrays were fabricated [108]. In this case the fabrication steps used were similar to the ones for the colloidal templating process flow described in section 2.5.3. Once the PS beads were deposited manually, the wafers were subjected to a plasma treatment. The etching parameters used were: 20 minutes of duration with a coil power of 2000 W. The wafers were then pyrolyzed with the optimized pyrolysis recipe: 5 hours at 1100°C with a heating rate of 10°C/min. The metal deposition and the passivation layer step were the same as the one used in the colloidal templating fabrication.

Also in this case, during the pyrolysis step, the PS thermally degraded. As expected, the process led to the formation of pillars with sizes comparable with the dimension of the PS beads taken into account the shrinkage due to the pyrolysis. Figure 2.18 shows the structure obtained with the 150 µm PS beads. The diameter of the pillar is around 100µm with a height of approximately 1.5 µm.
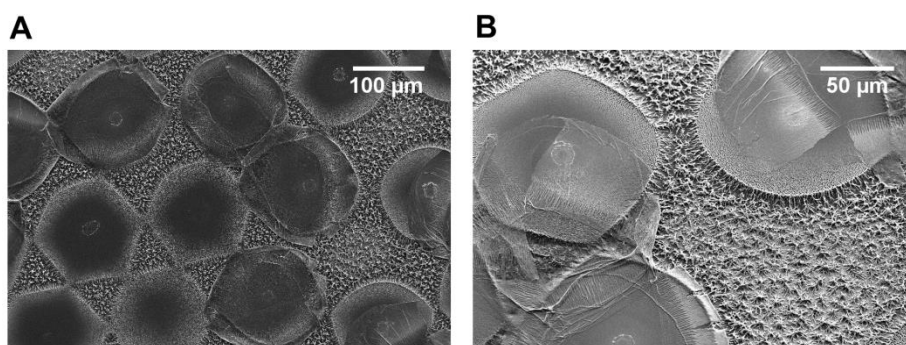
Figure 2.18: SEM images of the carbon WE surfaces obtained with colloidal lithography with the 150 µm PS beads.

For the structures obtained with the 10 µm beads, it was possible to achieve the fabrication of smaller pillars. In this case the pillar height was 3 µm with a diameter of around 1 µm. Also in this case, delamination did not occur and it was possible to continue with the electrochemical characterization (chapter 4).
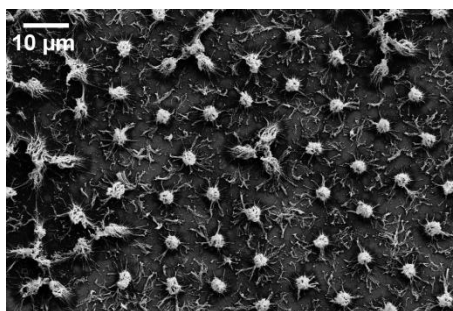
Figure 2.19: SEM image of the WE surfaces obtained with colloidal lithography with the 10 µm PS beads.

3. Material characterization and analysis

In order to characterize the surface, electrical and bulk properties of the fabricated carbon electrodes various techniques were used. From these analyses it was possible to understand the influence of the fabrication methods on the final performance of the electrodes more in depth. Furthermore, the mentioned material properties influence the electrode´s sensitivity, selectivity, and in general the interaction between the electrode and the electrolyte or cell substrate.

In this work, 4-point measurements were performed to investigate the electrical properties of pyrolytic carbon obtained with different processes. Raman spectroscopy was used to study the bulk properties and analyse the influence of the pyrolysis parameters on the graphitic content of the pyrolytic carbon. Surface characterization was performed using profilometry and scanning electrode microscopy (SEM). In the following sections these methods will be briefly introduced.

3.1 Electrical measurements

To investigate the electrical properties of pyrolytic carbon, four point probe measurements were performed. In this technique, a known current (I) is applied between two probes and the voltage drop (V) across the other two probes is measured. This method allows to perform more accurate measurements compared to the two point probe measurement, eliminating the influence of the lead and contact resistances [109]. The electrical properties of pyrolytic carbon have been previously tested using both two point and four point probe measurements [30,38,41,63]. In particular, Ranganathan *et al.* compared the sheet resistance (R_s) of pyrolyzed photoresists obtained at different temperatures using four point probe measurements [31].

In this work a custom-made four point resistance setup was used (Figure 3.1A) [110]. The Van der Pauw method was used to measure the R_s of the carbon thin films obtained through pyrolysis. This technique was introduced by L.J. Van der Pauw in 1958 to

measure the resistivity and the Hall coefficient of a sample [111]. It is one of the most effective and widely used methods of four-probe method for determining the resistivity of thin films [112]. It requires a two dimensional and homogeneous sample, with electrodes placed on its perimeter. Furthermore, the electrodes must have an area much smaller than the measured sample. Figure 3.1B shows the square device used for the electrical characterization obtained with the photolithography process reported in section 2.5.2. It consists of a 25 mm^2 area of pyrolytic carbon, surrounded by Au contacts.
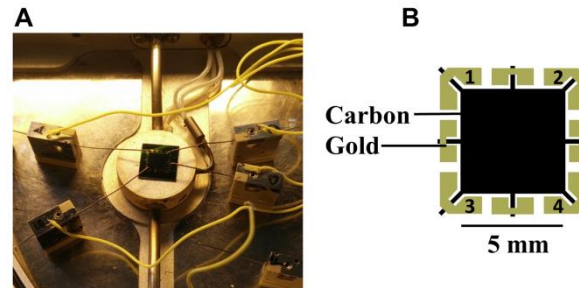
Figure 3.1: Van der Pauw device for four point probe measurements (A) and custom made 4-point probe resistance setup (B).

Using the electrode configuration reported in Figure 3.1B, the resistance R_A and R_C were measured as

$$R_A = \frac{V_{43}}{I_{12}}, \quad R_C = \frac{V_{31}}{I_{24}} \qquad\qquad \text{Equation 3.1}$$

Dual configuration measurements were performed to suppress geometrical errors in the calculation of the sheet resistance. In order to obtain a more precise measurement $R_{A'} = \frac{V_{21}}{I_{34}}$ and $R_{C'} = \frac{V_{42}}{I_{13}}$ were calculated and then averaged with R_A and R_C respectively. If all the conditions mentioned before are satisfied, Van der Pauw demonstrated that the following equation is valid:

$$e^{(-\frac{\pi R_A}{R_S})} + e^{(-\frac{\pi R_C}{R_S})} = 1 \qquad\qquad \text{Equation 3.2}$$

A Matlab script was used to caluclate R_s according to equation 3.2 [111]. The resistivity was calculated multiplying the sheet resistance value by the carbon film thickness.

Figure 3.2 reports the resistivity values measured for pyrolytic carbon obtained with an optimized process at 900°C (Paper 1) compared with carbon obtained from various pyrolysis processes at 1100°C. As it can be seen, the increase of pyrolysis temperature and longer dwell times lead to a decrease in resistivity (Paper II).
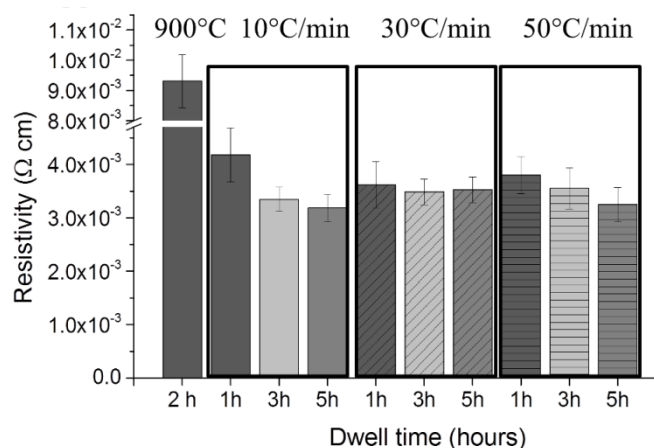
Figure 3.2: Resistivity measurements for pyrolytic carbon films obtained at 1100 °C using different dwell times in N_2 (1h, 3 h, 5 h) and different heating rates (10 °C/min, 30 °C/min, 50 °C/ min). Comparison with pyrolytic carbon obtained at 900 °C. Figure reproduced from [113].

3.2 Raman spectroscopy

Raman spectroscopy, discovered by Raman and Krishnan in 1928, is a technique used to investigate and study chemical and physical characteristics of materials [114]. It can be used to identify various compounds from specific spectral patterns (fingerprint) and to perform quantitative or qualitative analysis depending on the frequency or intensity of the scattered radiation respectively [115]. This technique is based on the inelastic scattering of incident radiation due to its interaction with vibrating molecules. During the measurements the sample is illuminated with a monochromatic laser beam which interacts with the molecules of the sample. The laser beam is basically an oscillating electromagnetic wave which induces an electric dipole moment when it interacts with the sample. Due to this perturbation molecules start to vibrate with a characteristic frequency v_m. This means that when the laser light with a frequency v_0 excites the

molecules, the oscillating dipoles can emit light in three different ways (Figure 3.3) [115,116]:

- Molecules with no Raman-active vibrational mode absorb the incident photon with frequency ν_0 and subsequently get back to the basic vibrational state emitting light with the same frequency ν_0. This kind of interaction is called Rayleigh scattering.

- When molecules in the basic vibration state have Raman-active modes, the photon with frequency ν_0 is absorbed, but the resulting frequency of the scattered light is reduced to $\nu_0 - \nu_m$, where ν_m is the frequency of the Raman-active mode. This shift to a lower frequency of the emitted photon is called Stokes shift

- If the molecule with Raman-active modes is already in an excited vibrational state, when the frequency of the incident photon is absorbed, the final basic vibration state will be less energetic compared to the initial one. In this case the frequency of the scattered light is shifted up (anti-Stokes shift).
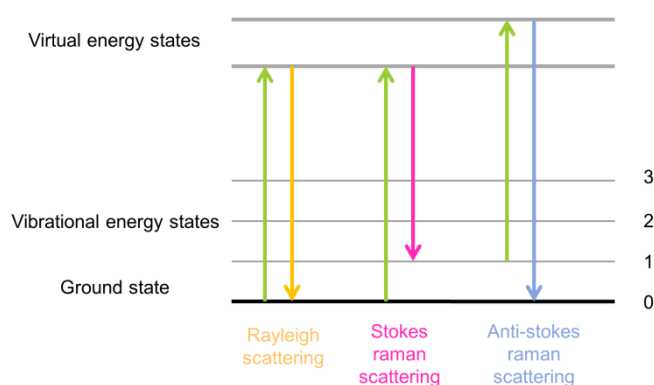
Figure 3.3: The energy level diagram and transitions responsible for Rayleigh, Stokes, and Anti-Stokes scattering

The intensity of the Stokes and anti-Stokes peaks in the Raman spectrum differs since they depend on the number or molecules present in the different vibrational states, which varies depending on temperature. At room temperature the ground state is more

populated than the first vibrational state, making the transition from the ground state to a higher vibrational state more frequent. For this reason the Stokes peaks appear stronger than the anti-Stokes scattering peaks [116].

In general, Raman has been used for the characterization of carbon. In this work, Raman spectroscopy was used to study the microstructure of pyrolytic carbon and to investigate the presence of possible variations in the graphitic content due to different pyrolysis processes. All the Raman spectra that were acquired showed two peaks characteristic for carbon materials (Figure 3.4)[117]: the G peak at 1590 cm^{-1} and the D peak at 1330 cm^{-1}. The G peak is due to the E_{2g} vibrational mode, which is related to the stretching of the bond between the sp^2 hybridized carbon atoms present in aromatic rings or olefinic chains [118]. The D peak instead is related to the A_{1g} mode which becomes active in presence of defects or disorder in the graphite lattice [118]. The ratio between the intensities of these two peaks I_d (D peak) and I_g (G peak) is inversely proportional to the crystallite size L_a [117]. An increase in the I_d/I_g ratio is an indication of the presence of an increasing disorder[118].
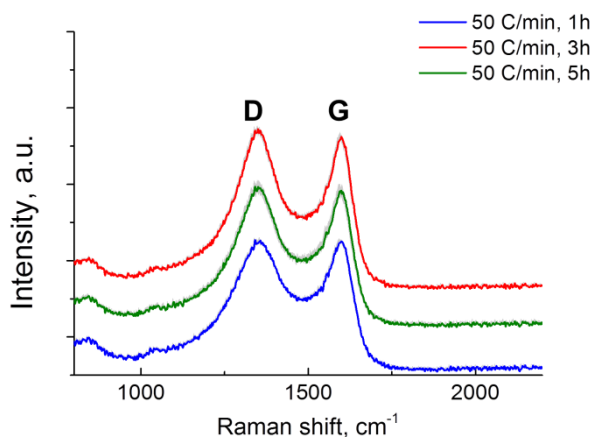
Figure 3.4: Raman spectra of samples pyrolyzed at 1100 °C using different dwell times in N_2 (1 h, 3 h, 5 h) and heating rate of 50 °C/min. The spectra show the D and G peaks. Data are presented as mean±standard deviation (n=3). Figure reproduced from [119].

In the comparison of different pyrolysis processes at 1100°C it was not possible to detect any significant variation in the I_d/I_g ratio (Paper II). The recorded differences were not comparable with the changes due to the increase of the final pyrolysis temperature [120].

3.3 Scanning electron microscopy (SEM)

In scanning electron microscopy (SEM) a focused beam of electrons is used to generate images which provide information regarding the composition and topography of the sample. From the interaction between the incident electrons and the sample different signals are generated, which are then collected in order to form an image used to analyse the surface of the sample [121]. The first scanning microscope was built by Knoll back in 1935. It had a resolution limit close to 100 μm but did not have demagnifying lenses to produce a fine probe. The first commercial SEM was developed by Cambridge Scientific Instruments in 1965 [122].

High vacuum SEM operates at pressures around to 10^{-4} Pa and requires the sample to be dry, clean and conductive (or coated with a conductive layer) in order to avoid surface charging. When the sample is exposed to the e-beam and scanned it is possible to gain information regarding the morphology, chemical composition and crystalline structure of the specimen from the signal generated from the electron-sample interaction. The collected signals consist of secondary electrons (SE), backscattered electrons (BSE), X-rays and cathodoluminescence (Figure 3.5).
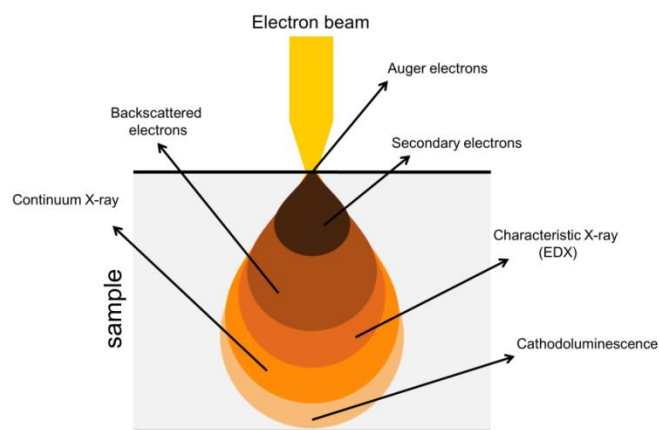
Figure 3.5: Interaction volume diagram and different types of signals generated by the sample.

Secondary electrons are emitted from the surface of the sample and are the result of inelastic collision between incident electrons and the substrate. These electrons have low energies (5-20 eV) and can only travel short distances through the sample. For this

reason secondary electrons originate from within 2-30 nm of the surface and are used to define morphology and topography. Backscattered electrons originate from the elastic scatter interaction of the positive nucleus with the incident beam, which causes the deflection of the electrons. The backscattered electrons have energies which span over a broad range. Their reflection is a function of the atomic number and they can come from a deeper area in the sample (up to almost 5µm) [121].

SEM was used to investigate the pyrolytic carbon structures obtained with colloidal lithography, colloidal etching, etching and to visualize 3D pillars structures (Figures 2.13, 2.14, 2.16, 2.18 and 2.19). Due to the conductivity of pyrolytic carbon, no coating was applied and the detection was made in high vacuum, using SE detectors and an acceleration voltage of 3 kV.

4. Electrochemical characterization

This chapter provides an overview of the electrochemical techniques used for the characterization of pyrolytic carbon elctrodes. In this thesis, electrochemistry was used to compare the performance of pyrolytic carbon produced with different fabrication techniques and pyrolysis processes. Cycling voltammetry (CV) and electrochemical impedance spectroscopy (EIS) were used to evaluate the electrochemical behaviour of the electrodes. EIS was also used to monitor adhesion, proliferation and differentiation of bone cells. Square wave voltammetry (SWV) was used for the electrochemical detection of the bone marker alkaline phosphatase (ALP). Chronoamperometry (CA) was used to monitor the photocurrent generated by cyanobacterial cells.

4.1 Electrochemical cell

Electrochemistry is the branch of chemistry which studies the relationship between electrical and chemical effects. Many of the studies related to this field investigate the production of electrical energy caused by chemical reactions and chemical changes due to the passage of an electric current. Electrochemical reactions are involved in various types of phenomena (corrosion and electrophoresis), technologies (e.g. electroplating) and devices (batteries, fuel cells and electroanalytical sensors) [80].

Electrochemical cells are formed by two half-cells, an anode and a cathode, separated by at least one electrolyte solution and in contact through an external conductor. The oxidation reaction takes place at the anode, while the reduction reaction occurs at the cathode. Electrochemical cells are classified either as galvanic or electrolytic cells. In a galvanic cell reactions occur spontaneously at the electrodes when there is an external connection through a conductor. In an electrolytic cell the reactions are affected by the imposition of an external voltage which is higher than the open circuit potential of the cell [123]. In this thesis all the experiments were performed using electrolytic cells. The

half-cell reactions are conventionally written as reduction reactions, as reported in Equation 4.1.

$$Ox + ne^- \rightleftarrows Red \qquad \text{Equation 4.1}$$

where *Ox* and *Red* are the oxidized and reduced species and *n* is the number of electrons transferred (e^-). Half-cell potentials can be recorded by measuring them in whole cells against the standard hydrogen electrode (SHE), which has a potential of 0 V at all temperatures at standard condition (activity $a_{H^+} = 1$, $p_{H^2} = 1$ atm and temperature T=298.15 K) . The Nernst equation furnishes the electrode potential vs. SHE as function of the oxidized and reduced species, and can be written as:

$$E = E^0 + \frac{RT}{nF} ln \frac{a_{Ox}}{a_{Red}} \qquad \text{Equation 4.2}$$

where a_{ox} is the activity of the oxidized species, a_{red} is the activity of the reduced species, E^0 is the standard potential at standard conditions ($a_i = 1$, pressure of 1 atm and T=298.15), n is the number of electrons, R is the gas constant (8.3145 J/mol K), F is the Faraday constant (96485 C/mol) and T is the temperature. Various E^0 can be found in literature for different redox reactions, and they define the tendency of a species to be reduced. Often, the standard potential is replaced by the formal potential $E^{0'}$, which incorporates the activity coefficients and some chemical effects of the medium . This quantity is the measured potential of the half-cell against SHE in presence of specific conditions concerning the concentration of the involved species, ionic strength and pH. In this case the Nernst equation correlates the electrode potential E with the concentrations of the oxidized ($[Ox]$) and reduced ($[Red]$) species taking part in the electrode process and can be rewritten as

$$E = E^{0'} + \frac{RT}{nF} ln \frac{[Ox]}{[Red]} \qquad \text{Equation 4.3}$$

In an electrochemical system, charge is transferred between an electronic conductor (electrode) and ionic conductor (electrolyte). The charge is transported through the electrode by the movement of electrons and holes, while in the electrolyte phase it is

37

transported by the movement of ions. When an external potential is applied, two types of processes can occur at the electrodes. Reactions where charges are transferred across the electrode/solution interface are called faradaic processes. In this kind of reactions the electron transfer is responsible for the oxidation or reduction of the species and the current is directly proportional to the number of molecules oxidised or reduced (Faraday´s law of electrolysis, Equation 4.4).

$$I = \frac{dQ}{dt} = nF\frac{dN}{dt} \hspace{3cm} \text{Equation 4.4}$$

where I is the faradaic current (in Ampere), Q is the total charge (in Coulomb), t is the time (in seconds), n is the number of electrons transferred, F is Faraday´s constant and N is the quantity (in moles) of species undergoing oxidation or reduction. When under certain conditions the electrode/solution interface shows a range of potentials without any charge-transfer reaction occurring because thermodynamically or kinetically unfavourable, then the process is called non-faradaic. In this case external currents can flow when the potential, electrode area or solution composition change.
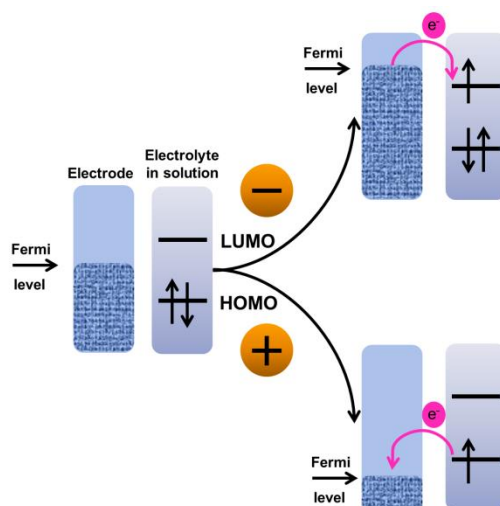
Figure 4.1: Reduction (top right) and oxidation (bottom right) processes of a species in solution happening when the equilibrium potential is perturbed by applying a negative or positive potential to the working electrode. An electron transfer between the electrode and molecular orbitals from the electroactive species takes place

When a negative potential is applied to an electrode, the energy of the electrons in the electrode material is raised, causing a flow of electrons from the Fermi level to the lowest unoccupied molecular orbital (LUMO) of the species in the electrolyte solution (Figure 4.1). In the same way, the energy of the electrons in the electrode can be lowered by applying a more positive potential, making it more favourable for some electrons of the solute species to transfer from the highest occupied molecular orbital (HOMO) to the conductive electrode material. The flow of electrons from the solution to the electrode is called oxidation current, while the current from the electrode to the solution is called reduction current.

When an electrode is immersed in an electrolyte solution, an array of charged species and oriented dipoles called electrical double layer is formed at the interface (Figure 4.2). The solution side of the double layer is formed mainly by two components: the inner layer, which contains adsorbed solvent molecules and ions and an outer layer consisting of solvated ions. The plane which crosses through the electrical centres of the specifically adsorbed ions is called inner Helmholtz plane (IHP), while the plane crossing through the centres of the nearest solvated ions is called outer Helmholtz plane (OHP). A three dimensional region of non-specifically adsorbed ions called diffusion layer is distributed from the OHP into the bulk of the solution due to thermal agitation in the solution.
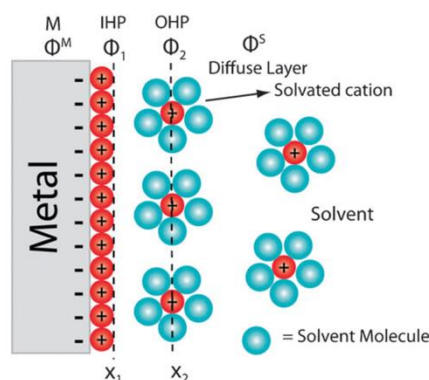
Figure 4.2: Double layer region with inner Helmholtz plane (IHP) and outer Helmholtz plane (OHP). Figure reproduced from [124].

Electrode reactions are distinguished between outer- and inner electron transfer reactions [123]. In an outer-sphere electrode reaction, the electron transfer between the oxidant or reductant species and the electrode takes place at the OHP. This means that this kind of interaction is weak and occurs always at a distance of at least a solvent layer from the electrode. The inner-sphere electrode reaction involves specific adsorption of species involved in the electrode reaction on the electrode surface. The electron transfer can take place through an adsorbed anion on the electrode at the IHP that serves as ligand bridge to a metal ion (Figure 4.3). Inner-sphere reactions are more dependent on the electrode material compared to the outer sphere ones [123,125]. An example of inner-sphere reaction is the one between Fe^{3+} and Fe^{2+} in hydrochloric acid, while the reaction between $[Fe(CN)_6]^{3-}$ and $[Fe(CN)_6]^{4-}$ is classified as outer-sphere electron transfer reaction [22].
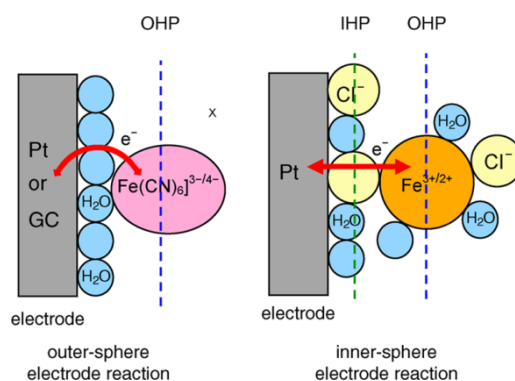
Figure 4.3: Outer- sphere (left) and inner-sphere (right) electron transfer mechanism. Figure reproduced from [125].

More generally, the overall electrode reaction is the result of a series of intermediate steps which are responsible for the conversion of the dissolved oxidized species to a reduced form (Figure 4.4). The electrode reaction rate is controlled by the rates of the following processes [123]:

- Mass transfer: for example the migration of the oxidized species from the bulk of the solution to the electrode surface
- Electron transfer at the electrode surface
- Chemical reactions taking place before or after the electron transfer reaction

- Surface reactions such as desorption, adsorption or crystallisation

Not all the listed processes take part in a general reaction sequence. When a steady-state current is reached, the reaction rates for all the processes involved are the same. The value of this current is limited by the slowest step of the sequence called the rate-limiting step.
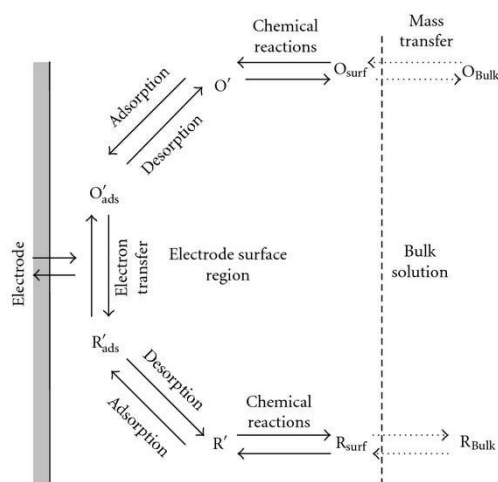
Figure 4.4: General electrode reaction pathway. Figure reproduced from [123].

4.2 Electrodes configuration and electrochemical setup

In an electrochemical system, the electrode where the reaction of interested takes place is called working electrode (WE), which is coupled with an electrode of known potential, such as the saturated calomel electrode, called reference electrode (RE). When small currents are being measured, a two-electrode configuration can be used. However, in most electrochemical experiments a three electrode configuration is used, where a counter electrode (CE) is introduced. The current is passed between the WE and the CE, and the CE must be chosen in a way that its electrochemical properties do not affect the behaviour of the WE. During the electrochemical measurements, depending on the technique used to perform the experiments, different electrode configurations were used (Table 4.1). In this thesis, all the working electrodes were made of pyrolytic carbon,

obtained with various fabrication techniques or pyrolysis processes. For the initial optimization of the pyrolysis process, the electrodes had also a pyrolytic carbon CE, while for the investigation of new 3D WE structures Pt was used. As CE, Pt is a commonly used material since it has fast electron transfer kinetics and is inert. Gold or Pt were used as pseudo-reference (pseudo-RE) electrodes. Pseudo-RE electrodes are commonly used in micro-fabricated electrodes due to the fact that they can be easily fabricated and integrated in the chip design. However they lack thermodynamic equilibrium and their potential shifts during the measurements depending on the applied current density. Moreover they can only operate over a limited range of conditions such as temperature and pH [99]. It is thus important to check the potential regularly and adjust it accordingly. The most used pseudo-REs are metal wires or deposited layers of Ag, Pt and Au. For the chip obtained with different precursors (section 2.3.2), external Pt CE and RE were used due to the impossibility to pattern these electrodes. For the other chips obtained through lithography (section 2.5), Au and Pt were deposited through e-beam evaporation using a shadow mask.

Table 4.1: Overview of the different electrodes and configurations used.

	Pt CE and RE	Au RE	Description
2D, photolithography	✓	✓	Paper I,Paper II
2D dots, photolithography		✓	Paper I,Paper III
2D, colloidal templating	✓		Section 2.5.3
2D, etching	✓		Section 2.5.4
2D, colloidal lithography	✓		Section 2.5.5
3D, photolithography	✓	✓	Paper IV and Section 6.4
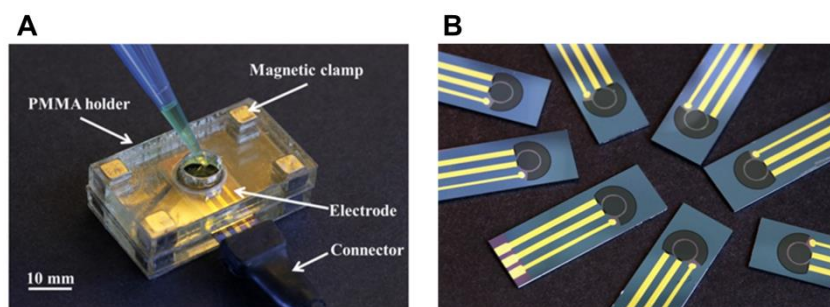
Figure 4.5: Magnetic clamp system (A) and electrochemical electrodes (B).

The electrode chips were placed in a poly-methyl-methacrylate (PMMA) based self-aligning magnetic clamping system fabricated in collaboration with PhD student Suhith Hemanth [126]. The batch system was fabricated using a CO_2 laser machine to cut different PMMA parts, which were subsequently bonded together with pressure sensitive adhesive (PSA). The final system had a reservoir of 300 µL (Figure 4.5A).

4.2 Cyclic voltammetry

Cyclic voltammetry is an electrochemical technique where a potential is applied to the WE and swept linearly from the starting potential E_i to the final potential E_f and then back to E_i. The current response of the forward and reverse potential scan can be plotted against the applied potential, obtaining the typical cyclic voltammogram. Usually during a measurement a series of potential scans (cycles) are recorded. The rate with which the potential is varied is called scan rate or sweep rate v (in V/s) and represents the slope of the potential vs time plot (Figure 4.6).
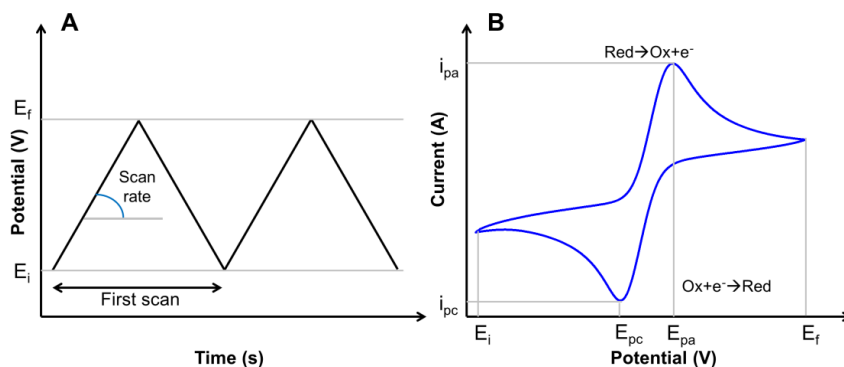
Figure 4.6: Potential triangular waveform (A) and typical current vs potential voltammogram for a reversible redox reaction (B). i_{pa} and i_{pc} represent the anodic and cathodic peak current, while E_{pa} and E_{pc} represent the anodic and cathodic peak potentials.

As the potential increases during the forward scan, it reaches the oxidation potential of the analyte and a faradaic current can be recorded. When the concentration of the analyte gets depleted close to the electrode surface, the current drops and the resulting peak is called oxidation peak current $i_{pa.}$ By reversing the applied potential, the reduction potential is reached and the reverse reaction of the previously formed product

takes place. The reduction peak i_{pc} has a similar shape compared to the oxidation peak, and for a reversible electron transfer process, i_{pc} is equal to i_{pa}. In this case, the theoretical potential difference between the oxidation and reduction peaks ($\Delta E_p = E_{pa} - E_{pc}$) is equal to $\frac{59}{n}$ mV at 298 K, where n is the number of exchanged electrons. This value is used as indicator of the electrochemical reversibility of the redox process. The formal potential $E^{0'}$ of the redox couple can be calculated as the average of the peak potentials through the expression $E^{0'} = \frac{E_{pa} + E_{pc}}{2}$.

The peak current for a reversible and diffusion controlled system at 25°C (298 K) is given by the Randles-Sevcik equation [123] (Equation 4.5):

$$i_P = (2.687 \times 10^5)AC\ n^{3/2}\ v^{1/2}\ D^{1/2} \qquad \text{Equation 4.5}$$

where A is the area of the electrode, C the concentration of the species, v the scan rate, n the number of electrons transferred per reactant molecule and D the diffusion coefficient. For a reversible reaction the peak currents are directly proportional to the concentration of the reactant and the square root of the scan rate.

Here, all the pyrolytic carbon electrodes were characterized with the $[Fe(CN)_6]^{3-/4-}$ redox couple, one of the most used for electrode characterization. It is a non-ideal outer sphere system since it is sensitive to surface impurities and other surface modifications (e.g. carboxylates) [127‑129]. For this reason all the electrodes were subjected to an oxygen plasma treatment for surface cleaning prior to measurements (0.5 bar, 50 W for 3 minutes). This treatment improved the electrochemistry of pyrolytic carbon, probably due to the removal of organic impurities (Figure 4.7A). CVs were recorded using a three electrode configuration, scanning the potential from -600 mV to 600 mV with a scan rate of 100 mV/s. Figure 4.7B shows the comparison between voltammograms of carbon electrodes obtained at 900°C and 1100°C. As expected, the temperature increase leads to higher peak currents and smaller ΔE_p. Figure 4.8 shows the CVs recorded with different scan rates or concentrations and the linear relations of peak current values with the square root of the scan rate and the redox probe concentration (PAPER II). Also the

44

ΔE_p remained constant as expected for a reversible reaction. This shows that the electrode reaction is diffusion controlled and that pyrolytic carbon film exhibits a similar behaviour as glassy carbon [130].
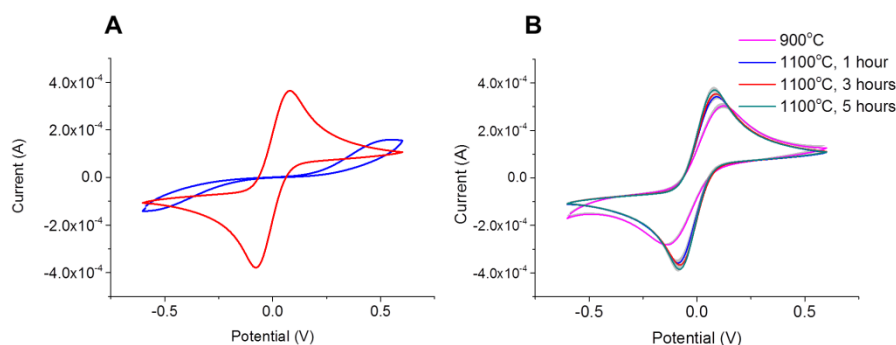
Figure 4.7: Voltammograms of pyrolytic carbon electrodes obtained at 1100°C before and after plasma treatment (A). Comparison between electrodes obtained at 900°C and 1100°C with a heating rate of 10°C/min acquired in 10mM ferri-ferrocyanide with a scan rate 100 mV/s. Data are presented as mean$\pm$ standard deviation (n=3). Figure reproduced from [113].
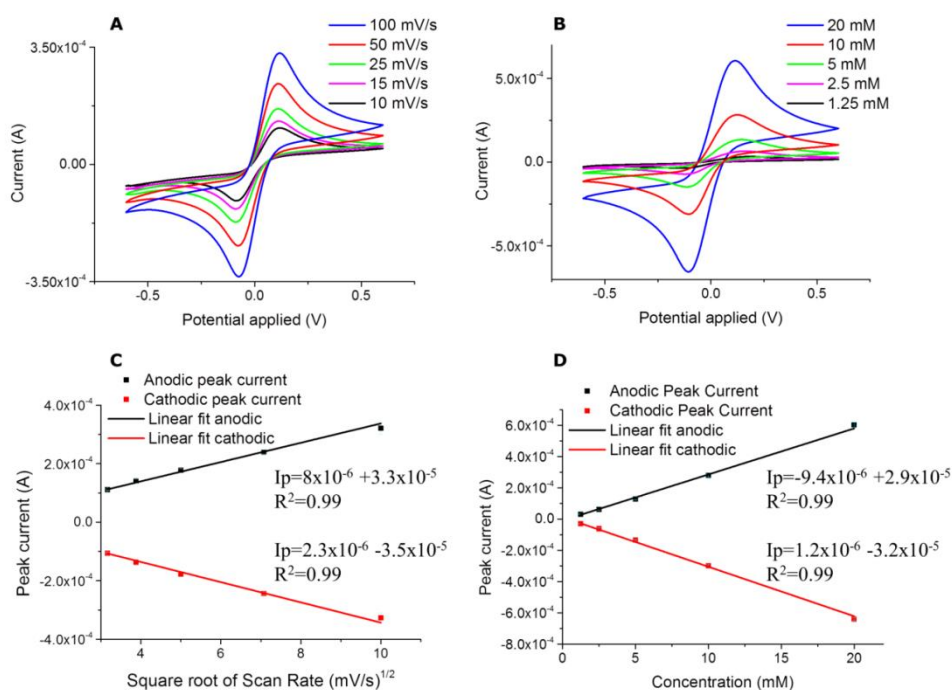
Figure 4.8: Voltammograms of pyrolytic carbon electrodes obtained at 1100 °C (h=50 °C /min, t=5 h) acquired in 10mM ferri-ferrocyanide varying scan rate (A) and concentration (B). Linear correlation between cathodic/anodic peak current and square root of scan rate (C) and the concentration (D). Figure reproduced from [113].

45

The electrodes fabricated with etching and colloidal lithography processes introduced in chapter 2, were compared with 2D electrodes using CV. Figure 4.9A shows the voltammograms obtained with electrodes with different structures on the WE presented in sections 2.5.3, 2.5.4 and 2.5.5. As it can be seen, the surfaces obtained through etching (t=25min and power=1000W) and colloidal lithography (bead size=150 μm) showed an improvement in the electrochemical behaviour, with smaller ΔE_p and higher peak currents compared to the 2D surfaces. Figure 4.9B shows the CVs obtained with different polymer precursors prepared as described in section 2.3.2. In this case the spray coating of other polymers did not lead to an improvement of the electrochemical performance, showing that SU-8 is the best precursor for the fabrication of pyrolytic carbon electrodes in these experiments.
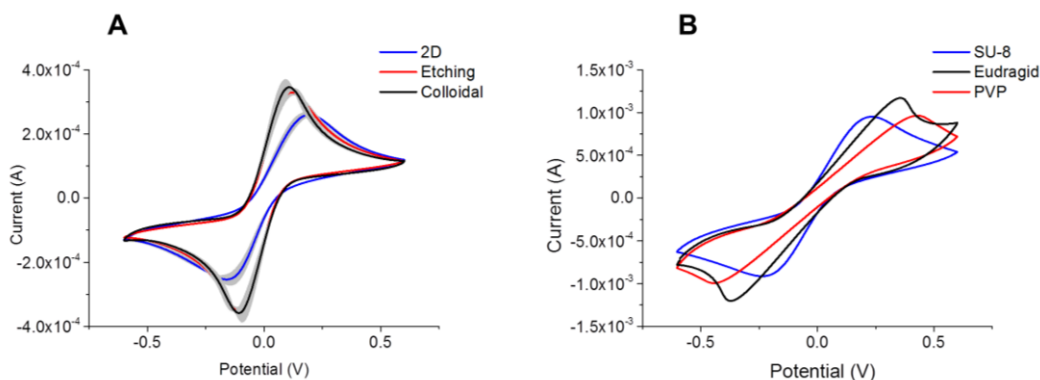
Figure 4.9: Voltammograms of pyrolytic carbon electrodes obtained at 1100°C with a various fabrication processes (A) and different polymer precursors (B) acquired in 10mM ferri-ferrocyanide with a scan rate 100 mV/s.

4.3 Square wave voltammetry

Square wave voltammetry (SWV) is a pulse voltammetric technique which consists of symmetrical square wave pulses with constant amplitude which are superimposed on a staircase-wave form. The applied voltage is alternated in a forward and reverse mode, but the final net potential measured is continuously increasing over time because of the potential stair case (Figure 4.10). The current is sampled at the end of the forward

potential pulse (forward current) and at the end of the reverse potential pulse (reverse current), just before the potential direction is reversed. The net current is obtained as the subtraction between the forward and backward currents [123,131]. When this current is plotted against the applied staircase potential a square wave voltammogramm is obtained, and the net peak current is directly proportional to the analyte concentration. The method of measurement used in SWV makes it one of the most sensitive electroanalytical techniques. One of the main advantages of this technique is the ability to distinguish between faradaic and charging currents. For all pulse techniques, there is a difference in the rate of the decay of the faradaic and charging currents after the potential steps. Faradaic currents decay with $t^{-1/2}$ in diffusion controlled electrode reactions, while capacitive currents decay exponentially. By sampling the currents at the end of the potential pulse, capacitive currents become negligible. This fact increases the sensitivity of the technique and the measured current will be almost exclusively due to the faradic current. In this thesis SWV was used to indirectly measure the bone differentiation biomarker alkaline phosphatase (chapter 5).
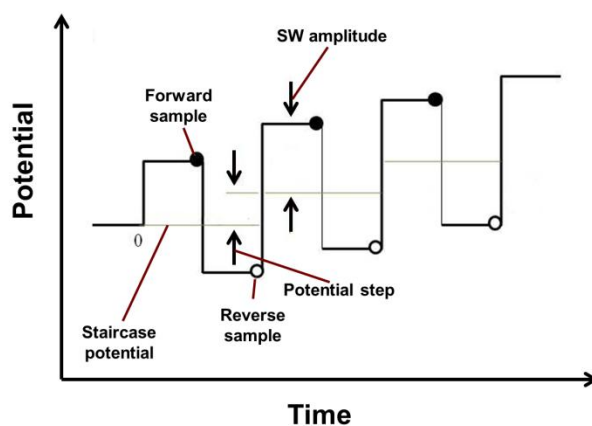
Figure 4.10: SWV potential scan and the characterizing parameters. Figure reproduced from [131].

4.4 Electrochemical impedance spectroscopy

Electrochemical impedance spectroscopy (EIS) is a technique used for the characterization of electrochemical systems which consists in applying a sinusoidal

excitation signal with small amplitude to a two electrode system (WE and CE) and measuring the response. The applied potential $E(t)$ can be expressed as:

$$E(t) = E_0 \sin(2\pi f t) = E_0 \sin(\omega t) \qquad \text{Equation 4.6}$$

where f is the frequency (Hz), ω is the radial frequency (rad/s) and E_0 represents the amplitude of the applied potential. The result is a current response composed of a sine wave with amplitude I_0 and the same frequency but shifted in phase (φ), depending on the resistive and capacitive components of the system (Figure 4.11):

$$I(t) = I_0 \sin(\omega t + \varphi) \qquad \text{Equation 4.7}$$

The impedance $Z(\omega)$ of the system can then be calculated with Ohm´s law:

$$Z(\omega) = \frac{E(t)}{I(t)} = \frac{E_0 \sin(\omega t)}{I_0 \sin(\omega t + \varphi)} = |Z| \frac{\sin(\omega t)}{\sin(\omega t + \varphi)} \qquad \text{Equation 4.8}$$
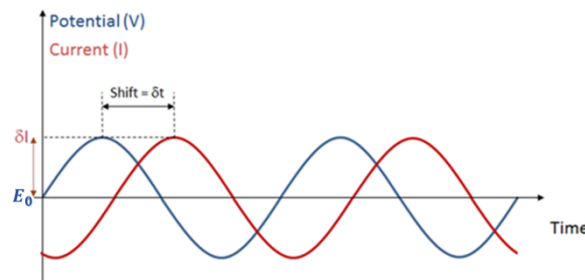
Figure 4.11: AC waveform for an applied potential and the resulting current. Figure reproduced from [132].

$Z(\omega)$ is a complex quantity and can be re-written using Euler´s relationship $e^{(j\varphi)} = \cos(\varphi) + j \sin(\varphi)$, where $j = \sqrt{-1}$:

$$Z(\omega) = \frac{E(t)}{I(t)} = \frac{E_0\, e^{(j\omega t)}}{I_0\, e^{(j\omega t - j\varphi)}} = |Z| e^{(j\varphi)} = |Z|(\cos(\varphi) + j \sin(\varphi)) = Z_{real}(\omega) + j Z_{imag}(\omega)$$

$$\text{Equation 4.9}$$

where $Z_{real}(\omega)$ is the real part of the impedance, $Z_{imag}(\omega)$ is the imaginary part.

In an electrochemical cell the electron flow can be slowed down by various phenomena which can be considered similar to the action of resistors, capacitors and inductors in an

electronic circuit. In direct current circuits, only resistors produce this effect, while in alternating current circuits also capacitors and inductors can impede the flow of the electrons.

The impedance of an ideal resistor does not depend on frequency, while an ideal capacitor is purely imaginary and depends on frequency:

$$Z_{resistor} = R$$

Equation 4.10

$$Z_{capacitor} = \frac{1}{j\omega C}$$

Equation 4.11

In case of a purely resistive behaviour from the circuit, no phase shift in the sinusoidal response current is detectable. For a purely capacitive behaviour, the response current is delayed by 90°[123]. To analyse the impedance response it is possible to use an equivalent electrical circuit model to fit the acquired data. One of the most frequently used circuits is the Randles equivalent circuit shown in Figure 4.12, used when a redox couple is present in the electrolyte.
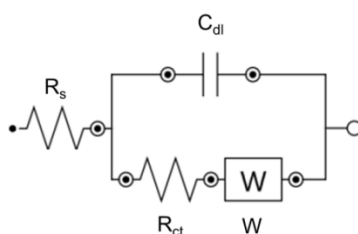
Figure 4.12: Randles equivalent circuit model.

The main contributions to the overall impedance of the electrochemical cell are: impedance of the electrolyte R_s and the impedance at the interface of the WE. R_s depends mainly on the ions present in the solution, on their concentration and on the temperature of the solution. The parallel part of the Randles circuit is used to take into account the fact that the total current that goes through the WE interface is formed by the current due to faradic and double layer charging processes. The double layer capacitance is almost a pure capacitance which is represented by C_{dl}. The faradic process can be modelled by a resistance, called charge transfer resistance (R_{ct}), and an

impedance element called Warburg element (W). R_{ct} represents the electron transfer limitation and is related to the surface area of the electrode, with rougher surfaces leading to lower R_{ct} values [133]. W represents a value used to take into account the mass transfer limitation caused by diffusion processes near the electrode. This element is characterized by having identical imaginary and real part components, resulting in a phase angle of 45°.

$$Z_W = \frac{A_W}{\sqrt{\omega}} + \frac{A_W}{j\sqrt{\omega}}$$ Equation 4.12

where A_W is the Warburg coefficient which describes the diffusion coefficient of ions in solution [123]. Impedance data are normally plotted using the Bode or Nyquist plots (Figure 4.13).
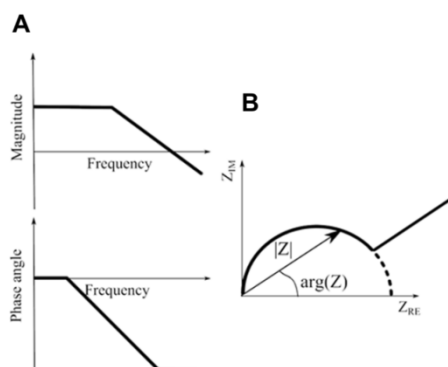
Figure 4.13: Schematic representation of Bode plot (A) and Nyquist plot (B). Figure reproduced from [134].

In the Bode plot the magnitude $|Z|$ and phase shift are plotted on the Y-axis in function of the frequency plotted on the X-axis. Using this representation it is possible to see how the impedance changes throughout the frequency range. The Nyquist graph plots the imaginary impedance component (Z_{imag}) against the real impedance component (Z_{real}) at each frequency. The main advantage of this plot is that is easy to visualise the effects of ohmic resistances. However, this representation does not explicitly show the frequency.
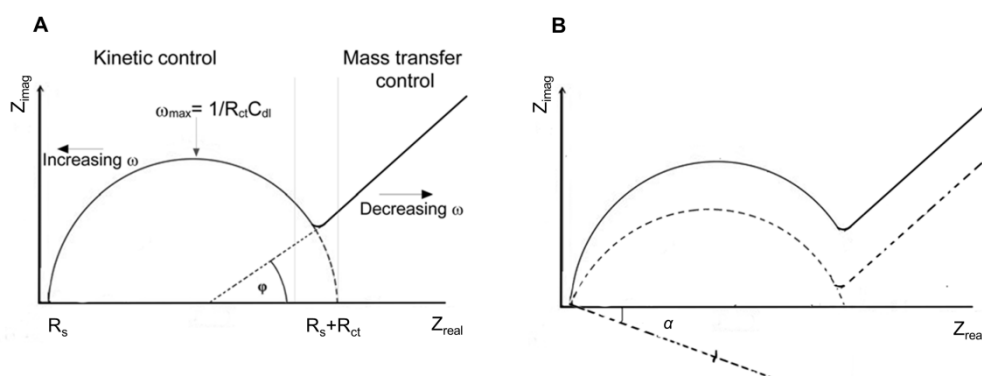
Figure 4.14: Nyquist plot for an electrochemical system with a redox probe. Regions of kinetic control and mass transfer are found at high and low frequencies respectively (A). Nyquist plot with n =1(solid line) and 0< n<1(dashed line). Figures modified from [108].

For an electrochemical system with a redox probe where polarization is due to the combination of kinetic and diffusion processes, the Nyquist plot usually consists of a semicircle and a linear part (Figure 4.14A). The semicircle is due to the electron transfer kinetics of the redox probe taking place at the electrode surface. The linear part at low frequency is the result of the diffusion-limited electron transfer process. The intercept of the semicircle with the real axis provides the value of R_s, while the diameter is used to evaluate the magnitude of the R_{ct}. The linear part ideally should form a 45° angle with the real axis due to diffusion controlled electrochemical reactions [135]. For real electrodes it is not always possible to model non-faradic components with a capacitor. Often this parameter is replaced by a constant phase element (CPE) which represents a pseudo-capacitive behaviour. In these systems, especially due to contaminations or roughness, the centre of the semicircle of the Nyquist plot is often located below the real axis (Figure 4.14B). This "non-ideal" behaviour can be represented by rotating the Nyquist plot for an "ideal" system by an angle $\varphi = \alpha \pi/2$. The CPE can be expressed as [131,135]:

$$Z_{CPE} = \frac{1}{Q(j\omega)^{\alpha}} \qquad \text{Equation 4.13}$$

where Q is the capacitance and α is the multiplication factor of the CPE. If α=1 the behaviour of the interface is purely capacitive, while if α=0 the behaviour is purely

resistive. A decreasing value of α can be associated with a more porous surface and a hence a different electron transfer mechanism. This parameter has been used previously to investigate surface roughness of pyrolytic carbon electrodes [66].

In this thesis, EIS was used to characterize more in the detail the electrochemical properties of pyrolytic carbon electrodes obtained with different pyrolysis processes (Paper II), and using etching and colloidal lithography as fabrication techniques (Figure 4.15). In particular, the wafers fabricated with the last two techniques showed as expected an electrochemical response typical for rough surfaces, with smaller R_{ct} and α values compared to 2D electrodes [133]. The measurements were acquired using a two electrode configuration (WE and CE) applying a sinusoidal potential of 10 mV, acquiring 10 points/decade in the frequency range of 0.1-106 Hz.

Furthermore, EIS was also used to monitor adhesion, proliferation and differentiation of Saos-2 cells (chapter 5 and Paper III).
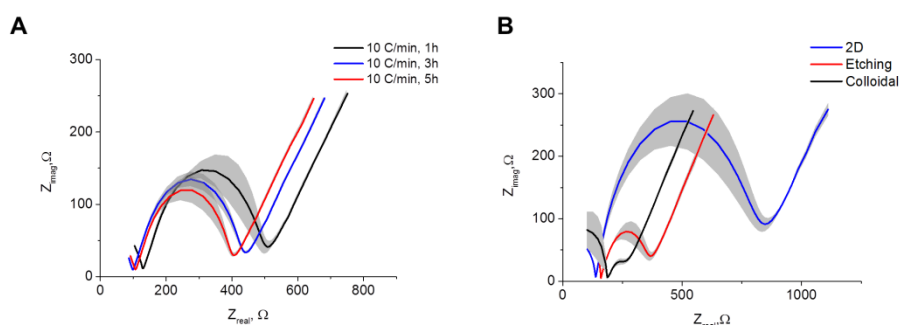
Figure 4.15:Impedance spectra of pyrolytic carbon electrodes obtained with different dwell times at 1100°C and a heating rate of 10°C/min (A) and with different fabrication processes (B) acquired in 10mM ferri-ferrocyanide. Data are presented as mean $\pm$ standard deviation (n=3).

Table 4.2: Values (average $\pm$ standard deviation, n=3) obtained from the fitting of the acquired impedance spectra for electrodes fabricated with different techniques. R_{ct} is the charge transfer resistance while α is the multiplication factor of the CPE.

Circuit element	2D	Etching	Colloidal lithography (150μm beads)
R_{ct} (Ω)	680.4±111.1	199.5±34.3	92.3±9.4
α	0.815±0.008	0.822±0.008	0.634±0.035

4.5 Chronoamperometry

Chronoamperometry is a technique in which either a single or double potential step is applied to a system for a time period τ at the step potential E_s and a current is measured. The potential applied to the WE is initially held at a value E_i where no faradic reaction occurs, before increasing it to E_s. When a single potential step is applied only the current resulting from the forward step is recorded, while in the double potential step the forward potential is returned to a final value $E_f = E_i$ and cathodic and anodic current can be recorded. This technique is used to study the diffusion processes, kinetics and adsorption of chemical reactions, but can also be used to monitor or detect events. The mass transport during the experiment is governed only by diffusion, and as the reactant gets depleted next to the electrode surface, a decrease of the concentration gradient can be observed over time [123,136]. The most used equation in chronoamperometry is the Cotrell equation, which expresses the recorded current over a period of time as a function of $t^{-1/2}$.

$$i_t = \frac{nFACD^{1/2}}{\pi^{1/2}t^{1/2}}$$
Equation 4.14

where n is the number of electrons involved in the reaction, F is Faraday´s constant, A is the surface area of the planar electrode (cm^2), C is the concentration of the electroactive species (mol/ cm^3), D is the diffusion coefficient of the species (mol cm^3) and t is the time (s). Chronoamperometry can be used for example to determine accurately one of the variables in Equation 4.14, such as the electrode surface area by using a well-known redox couple with defined n, D and C_0.

In this thesis, chronoamperometry was used in order to investigate the electrochemical performance of pyrolytic carbon as anode material in biophotovoltaic cells (chapter 7).
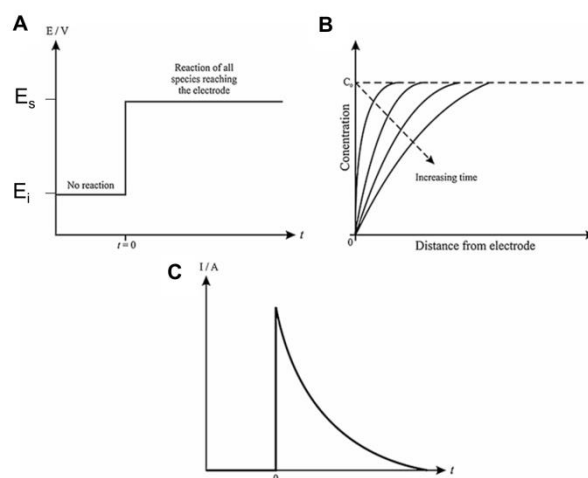
Figure 4.16: Chronoamperometry: potential-time waveform for single potential step (A), concentration gradient (B) and current-time response (C). Figure reproduced from [135].

5. Monitoring bone cell differentiation on 2D pyrolytic carbon microelectrodes

In this chapter 2D pyrolytic carbon electrodes with a modified design were used for the monitoring of bone cell differentiation using impedance spectroscopy and square wave voltammetry. The chapter starts with an introduction to bone tissue and its regeneration process. Then, *in vitro* cell-based viability assays are introduced and the use of electrochemical impedance spectroscopy for cell monitoring is described. The 2D dots electrodes used to perform the cell experiments are described and their electrochemical characterization is reported. Finally, the electrochemical assay used for the detection of the bone differentiation biomarker alkaline phosphatase (ALP) is described.

5.1 Introduction

Pyrolytic carbon is a material which due to its biocompatibility has been previously used as implantable material, for example such as heart valve [137,138]. In particular, due to this property, pyrolytic carbon obtained from the pyrolysis of photoresists has been used as substrate for cell culturing and differentiation and in the sorting and manipulation of bioparticles [34,40,68]. Due to their excellent electrochemical properties, pyrolytic carbon electrodes with various surface modifications have also been used for biosensing applications such as immunosensors, aptasensors and enzymatic sensors [37,38,45,139]. Pyrolyzed photoresists thus combine biocompatibility, electrical conductivity, remarkable electrochemical properties and a stable, easy and reproducible fabrication process. This in principle allows the development of a platform which can be used both as substrate for cell culturing and as electrochemical sensor. For example, Amato *et al.* demonstrated that neuronal stem cells cultured on a pyrolytic carbon substrate showed enhanced differentiation into

dopaminergic neurons and that the same carbon electrode could be used for the detection of dopamine release [40].

5.2 The bone

5.2.1 Bone tissue

Bone is a complex and dynamic connective tissue, characterized by its hardness, rigidity, and ability to regenerate and repair [140,141]. It is responsible for many functions such as protecting the vital organs, providing maintenance of mineral homeostasis and acid-base balance, being a reservoir of growth factors, containing bone marrow and being the main site for haematopoiesis, the process which leads to the formation of blood cellular components [142,143]. Bone tissue is composed of an organic matrix consisting of oriented collagen fibers and other non-collagenous proteins (such as osteonectin, osteocalcin, osteopontin, etc), a mineral matrix, mainly consisting in calcium hydroxyapatite, and water [143]. The two macroscopic components which form the bones are: i) the cortical bone, which is solid, dense and surrounds the marrow space and ii) the trabecular bone, a spongy structure formed by a network of plates and rods (trabeculae) dispersed in the bone marrow compartment.
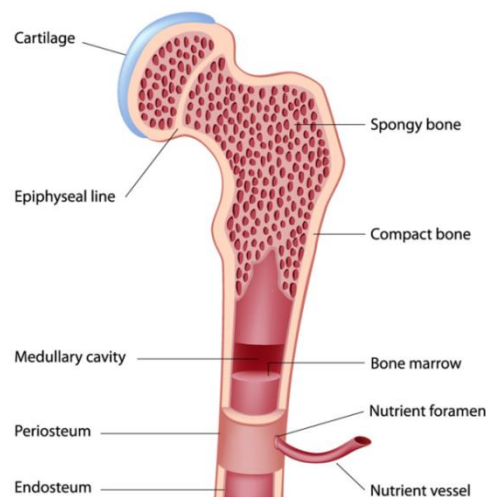
Figure 5.1: Cortical and trabecular (spongy) bone. Figure reproduced from [144].

Cortical bone, also called compact or lamellar bone, forms the outer shell of most bones. It has a hard and stiff structure and it consists of closely packed osteons, structures formed by the central Haversian canal which contains blood vessels and is surrounded by concentric rings (lamellae) of matrix. Osteons (or haversian systems) are tightly packed together and form a solid mass (Figure 5.2).
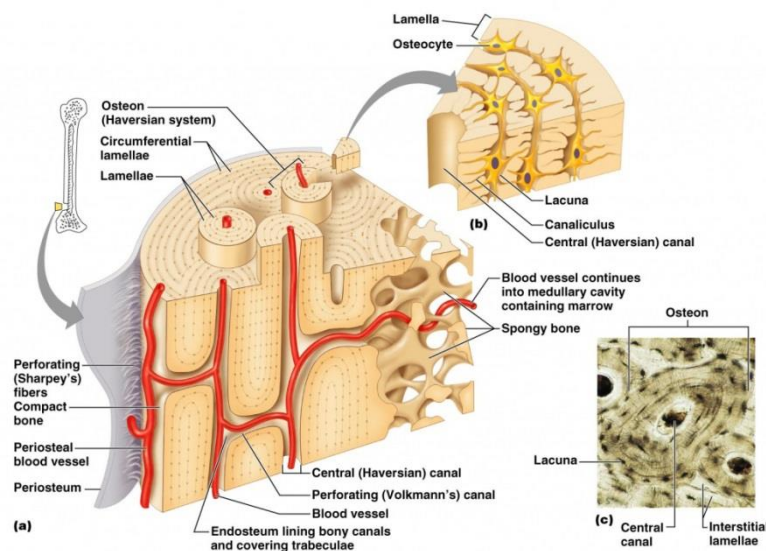
Figure 5.2: Structure of cortical bone and osteon unit. Figure reproduced from [145].

Trabecular bone consists of plates and bars organized in a honeycomb structure, which contains cavities filled with red bone marrow responsible for haematopoiesis. Adjacent cavities are connected by canaliculi, which provide blood supply and make trabecular bone a highly vascularized structure (Figure 5.3). This organization, which provides high surface area, is the reason why trabecular bone is also called spongy bone. It is highly porous and has a less dense and stiff structure[141,143]. Bone undergoes continuously a remodelling process in order to adapt to the changes in the biomechanical forces applied and to remove old or damaged bone, replacing it with new and mechanically stronger bone [140,146]. This process is mediated by two main types of bone cells: osteoblasts and osteoclasts. Osteoblasts are in charge of synthetizing the extracellular bone matrix during a process called osteogenesis, while osteoclasts are responsible for bone resorption in the remodelling phase [147]. Osteoblasts originate

from mesenchymal stem cells and are responsible for the secretion and mineralization of bone matrix. When they differentiate they acquire the ability to secrete an extracellular organic matrix, which is then mineralized. This process is characterized by three phases: cell proliferation, matrix maturation and matrix mineralization (Figure 5.4)[140,148].
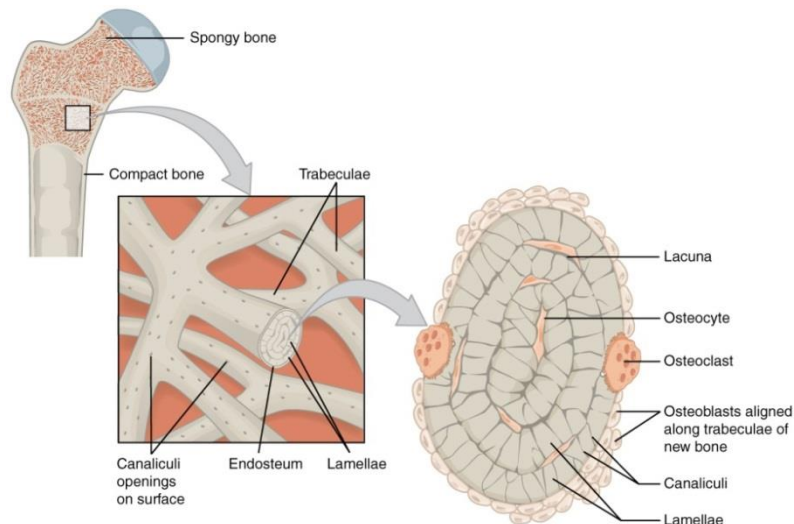
Figure 5.3: Structure of trabecular bone. Figure reproduced from [149].

During the matrix maturation phase the biomarker alkaline phosphatase (ALP) reaches its maximal expression [150]. Small membrane-bound vesicles that contain calcium and phosphate are released, and deposition of hydroxyapatite occurs [140,151]. The mineralization process starts approximately 30 days after organic matrix deposition. When osteoblasts remain trapped in the bone matrix, they gradually stop secreting osteoid (the organic, unmineralized matrix) and become osteocytes. This is the last stage of the osteoblast differentiation process and osteocytes are located in the inner part of the cortical and trabecular bone (in the lacunae and canaliculi). Osteocytes communicate with each other through the extensions of their plasma membrane and instruct osteoclasts on the resorption process [141]. Osteoclasts originate from hematopoietic stem cells and are responsible for the resorption process [146]. The degradation of hydroxyapatite occurs by the creation of a local acidic

microenvironment, while the remaining organic matrix is degraded by secreted enzymes.
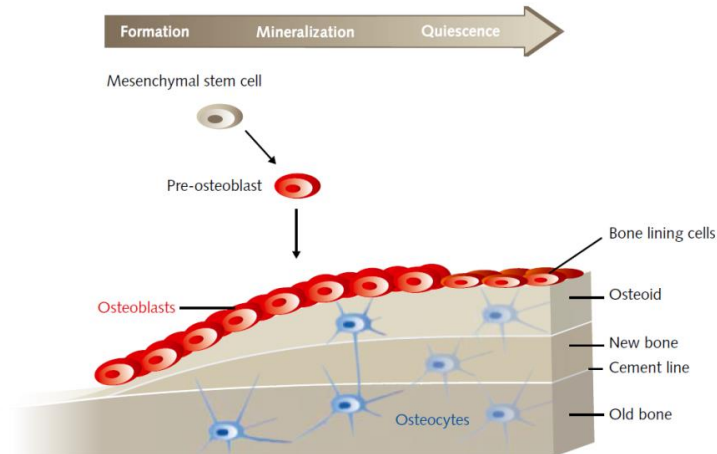
Figure 5.4: Osteoblasts differentiation process. Figure reproduced from [150].

5.2.2 Osteoporosis

An unbalance in the bone turnover process may cause excessive or inadequate mineralization. Osteoporosis is a metabolic disease related to anomalies in the bone regeneration process, in which the resorption process prevails over the formation of new bone. It is a degenerative skeletal disease, and during its progression bones lose their mass and modify their microarchitecture becoming more brittle and prone to fractures (Figure 5.5) [152]. Osteoblasts are unable to compensate the action of osteoclasts, which leads to a bone structure with lower mass and higher porosity [153].
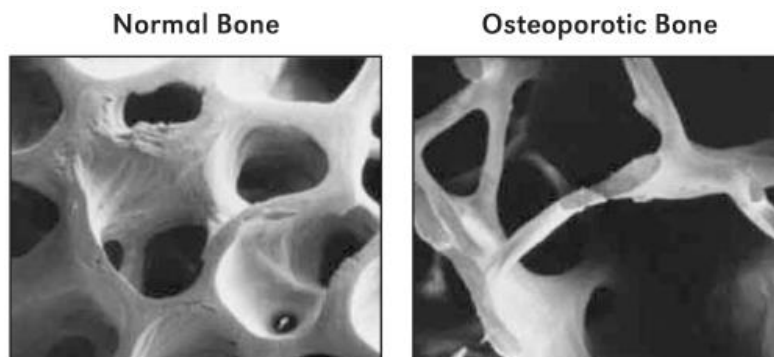
Figure 5.5: Scanning electron micrographs, from biopsies of a normal and an osteoporotic patient. Figure reproduced from [154].

It is estimated that about 40% of white postmenopausal women and 20% of men older than 50 years are affected by this disease [152,155]. The higher incidence for women is explained by the decrease of estrogen levels after menopause, the hormone being involved in the maintenance and development of bone mass [152]. Most fractures involve vertebral bodies, forearm and hip, and the occurrence of these events has an impact on the quality of life and mortality, making osteoporosis a global health-economic problem [155,156]. Only in the US, in 2010 the annual medical costs associated with osteoporosis ranged from 14 to 20 billion dollars [157]. The conventional treatments are based on estrogen replacement, bisphosphonates and calcitonins. However long-term side effects comprehend an increased risk of breast cancer, endometrial cancer and venous thromboembolic disorders [155].

In order to develop new compounds which may help treating osteoporosis and other bone metabolic diseases it is necessary to gain a deep understanding of the biology related to bone turnover mechanism [155]. *In vitro* studies are hence fundamental tools for the development of more selective and effective drugs.

5.3 *In vitro* cell-based viability assays

The drug development process is a long and expensive process which consists of several phases [158]. After the discovery and development phase, where new compounds or drug formulations have been identified in the laboratory, a preclinical research phase starts, where the drug is tested *in vitro* and subsequently *in vivo* in order to address basic safety issues. *In vitro* models offer the possibility to study cellular mechanism in order to develop new drugs and evaluate their therapeutic or toxic effect [159,160]. This approach consists in simplifying experimental variables in order to isolate different components of organ structures for studies under controlled and easily assessed conditions [160]. In the clinical phase studies or trials are done on people to test their effectiveness and define the optimal dosage [158,161,162]. In this scenario, *in vitro* cell-based screening assays are widely used to evaluate the interaction between the cell culture and the new compounds being tested. In this way it is possible to gather further

information on the potential new drug, such as toxicity and efficacy. Most of the cell-based assays are performed on two dimensional (2D) substrates. By observing cell activities, *in vitro* cytotoxicity and viability studies can assess if a compound is cytotoxic based on the variation of cell growth, proliferation, shape variation and apoptosis [163]. The standard techniques are based on the quantification of the number of cells and viability, and mainly rely on optical detection using luminescent, colorimetric or fluorescent methods. Typical colorimetric assays used to asses viability are for example the MTS (3-(4,5-dimethylthiazol-2-yl)-5-(3-carboxymethoxyphenyl)-2-(4-sulfophenyl)-2H-tetrazolium) assay and MTT ((3-(4,5-dimethylthiazolyl)-2,5-diphenyltetrazolium bromide)[163,164]. MTS consists in the incubation of a cell culture with a buffer saline solution containing tetrazolium, which gets reduced to purple formazan by mitochondrial activity and cytosolic enzymes [164]. Colorimetric assays are also used to assess cytotoxicity using for example lactate dehydrogenase (LDH) measurements [163]. All these measurements have various advantages, but their common disadvantage consists in the fact that they all are single end point measurements, which do not provide information about real-time kinetics of the events of interest. Moreover these techniques are labor intensive, require multiple labelling steps and can be invasive. To overcome these limitations and obtain minimally invasive, label-free and cost efficient measurement techniques able to provide a real-time monitoring, new technologies were introduced during the past years. Among various techniques, such as quartz crystal microbalance, optical waveguide light mode spectroscopy and refractive index based technologies, electrochemical methods have emerged as a valid alternative or complement to the standard techniques described previously [165‑167]. Electrochemical impedance measurements in particular have been used to monitor the effect of various compounds on cell viability [168‑170]. Furthermore, this technique allows the monitoring of the behavior of the same cell population and its dynamics.

5.4 Electrochemical impedance spectroscopy for cell monitoring

5.4.1 Introduction

The discovery of the resistive dielectric properties of cell membranes surrounding a conducting electrolytic interior dates back to 1911, when Rudolf Höber measured the electrical impedance of suspensions containing red blood cells or muscle cells [171]. From that date, further studies have been carried out in the field of impedance analysis of cell populations [172]. In 1984, Giaver and Keese applied for the first time impedance measurements on cells and demonstrated how this technique could be used to perform *in vitro* studies of cellular functions. In this study human lung fibroblasts were cultured on polystyrene culture dishes containing a counter electrode and multiple working electrodes. A small sinusoidal signal was applied and the influence of the cell morphology variation on the response was recorded [173].

Further studies were carried out in order to investigate for example the effect of protein coating on cell migration and the influence of changes in pH and temperature on cell morphology [174‑176]. As described previously, these systems can be used for pharmacological and cell biology studies. They have also been applied to demonstrate that cell adhesion and morphology are affected by the presence of cytotoxic compounds and drugs [169,177‑180]. Various systems have been designed for this kind of studies, and in 1991 Applied BioPhysics Inc. commercialized an impedance spectroscopy-based platform to perform cell studies called Electric Cell-substrate Impedance Sensing (ECIS®). An automated high-throughput screening system version has been developed by ACEA Biosciences (xCELLigence®) and applied in the fields of cancer research and drug discovery [181‑184]. These systems have also been used to monitor cell migration and stem cell differentiation [176,185]. However, new tailor-made systems were developed recently in order to investigate more in detail specific biological issues that were impossible to address using the commercially available systems [186].

5.4.2 Basic principle of ECIS

In cell-based impedance measurements cells are considered as dielectric particles due to the insulating properties of the membrane. During cell attachment to the substrate, various morphological changes occur which affect the electrode/electrolyte interface. The cells reaching the surface of the electrode have a spherical shape and over time the adhesion area increases, decreasing at the same time the free electrode area (Figure 5.6). Since the impedance value is inversely proportional to the free electrode area ($Z \propto 1/A$), cell adhesion and spreading causes an increase of the total measured impedance [187].
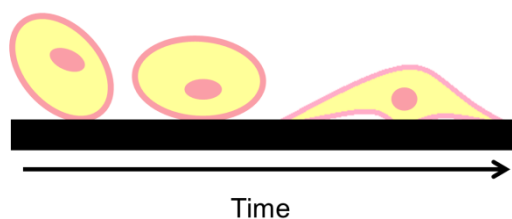
Figure 5.6: Time course cell adhesion and related increase of adhesion area.

To perform these experiments, a two-electrode setup consisting of WE and CE is used. The overall measured impedance consists of the impedance of the WE at the electrode/electrolyte interface (Z_{WE}), the impedance at the same interface at the counter electrode (Z_{CE}) and the impedance of the electrolyte solution (Z_S). If in the configuration used the CE is significantly larger than the WE, Z_{CE} can be considered negligible compared to Z_{WE}. This approximation cannot be applied in the case of interdigitated electrodes, where CE and WE have the same area.

When there are no cells, a current between WE and CE flows without any constriction (Figure 5.7A). When cells start to adhere to the electrode surface, due to their membrane properties, they behave as an insulator. The increasing coverage of the electrode leads to the increase of the impedance value (Figure 5.7B). Measurements can be performed over time either at a specific frequency or over a frequency range [187]. For low frequencies (~100-10000 Hz), most of the current is constrained to flow around cells, squeezing in narrow channels beneath and between them. In this case the impedance has a large resistive component, and measurements recorded at these

frequencies provide information about cell-cell and cell-substrate interaction (Figure 5.7C). At higher frequencies (>10000 Hz) most of the current flows through the cell membrane, and the monitoring of cell behavior at these frequencies is useful to gain information related to changes of the electrode coverage, due to cell proliferation, migration or apoptosis (Figure 5.7D) [188,187]. The recorded impedance thus depends on several parameters such as the degree of coverage of the electrode, the morphology, the cell doubling time and the level of cell adhesion.
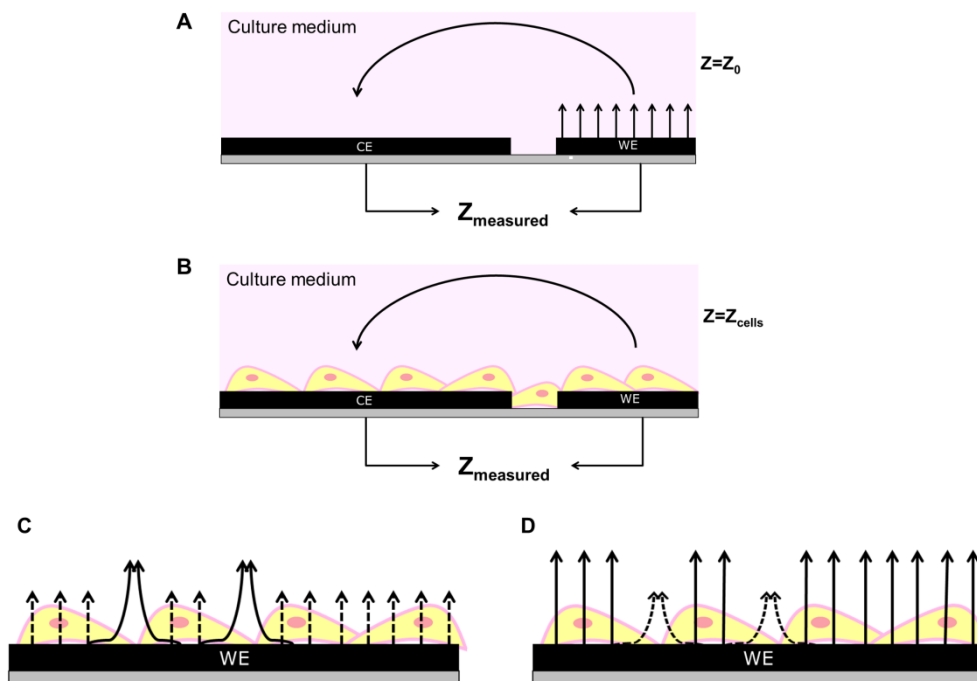
Figure 5.7: Schematic of WE and CE indicating the current flow through culture medium in absence (A) and in presence (B) of cells. Representation of current flow in presence of cells at low (C) and high (D) frequencies.

5.4.3 Cell-electrode impedance models

During cell based impedance measurements, the overall impedance value recorded $Z_{measured}$ consists of various contribution, including the cell impedance Z_{cells}. Parameters such as electrode material, surface roughness, adsorption of impurities, ions present in the electrolyte, etc. have also an influence on the measured impedance value. Parasitic effects are always present and they are mainly due to wire connections and stray

capacitances. They are unavoidable and must be taken carefully into account, especially when designing the electrodes and the measurement setup [189]. In order to distinguish various contributions, equivalent circuits containing different electrical components such as resistors and capacitors are used. As described previously (section 4.4) the solution resistance is modeled by a resistor R_s, which describes the losses due to the current flowing between WE and CE in the solution. In presence of cells there is an additional solution resistance component: R_{seal} [190,191]. R_{seal} represents the resistance between the electrode and the bulk electrolyte due to the thin layer of medium between the cells and the electrode. It models the level of adhesion of the cells to the electrodes surface [192]. To describe the interaction between cells and electrodes surface, various models have been discussed and proposed [189‑193]. The cell membrane is composed of a phospholipid bilayer which contains intra-membrane proteins. It can be modeled as a capacitor, due to the insulating properties of the plasma membrane (C_m), in parallel with a resistor representing the ion channels along the membrane (R_m) (Figure 5.8A) [190,192]. Two of these parallel circuits are used to model the above mentioned properties at the cell/electrode interface and at the top and sides of the cell. A simplified and commonly used model uses a single parallel circuit containing a resistor and capacitor (R_{cell} and C_{cell}) which models the resistive and capacitive properties of the whole cell (Figure 5.8B) [177].
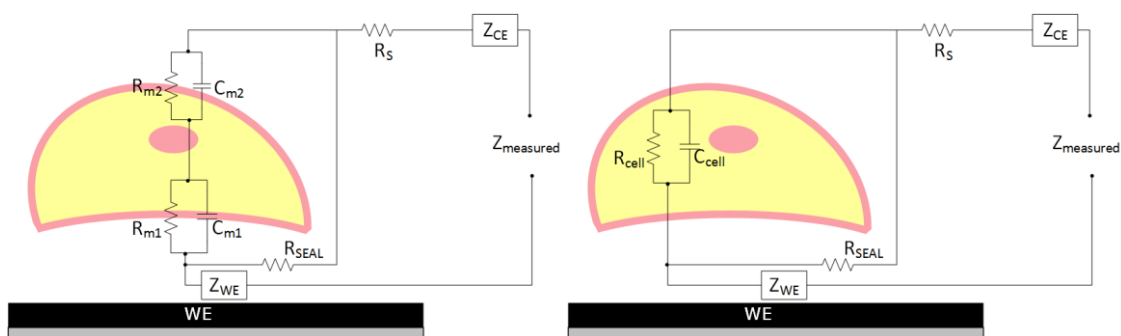
Figure 5.8: Schematic of equivalent circuit models of the cell-electrode impedance (not in scale). Z_{WE} is the working electrode impedance, R_S is the solution resistance, R_{SEAL} is the sealing resistance, Z_{CE} is the counter electrode impedance, R_m and C_m are the cell membrane resistance and capacitance (A). Simplified model with a parallel circuit containing a resistor and capacitor (R_{cell} and C_{cell}) (B).

5.4.4 Data analysis and cell index

Cell-based impedance experiments can be performed scanning through a range of frequencies in order to identify the spectral region where the major changes in the impedance values occur. In these regions the sensitivity to changes in cell coverage is the highest [168,177,187]. In order to analyze the acquired data, one of most used methods consists in tracking the impedance magnitude at a specific frequency over time. The dimensionless parameter used to express the relative variation of the impedance value is called Cell index (CI) [177,194,195]:

$$CI(t) = max_{i=1,....,N} \frac{|Z(t,f_i)|-|Z(0,f_i)|}{|Z(0,f_i)|}$$

Equation 5.1

where $|Z(t,f_i)|$ represents the magnitude of the impedance spectrum at a given frequency, $|Z(0,f_i)|$ represents the magnitude of the impedance recorded at the same frequency at the beginning of the experiment in absence of cell, while N is the total number of frequency points at which the impedance was recorded. Usually, the chosen frequency is where the cells mostly contribute to the overall impedance, which is the one where $|Z(t,f_i)| - |Z(0,f_i)|$ has the maximum value. This means that the CI provides information about the status of the cells covering the electrode. Under the same physiological conditions, morphology and cell density changes lead to variations in the CI values. In particular toxicity induced cell detachment and cell death, which are associated with cells rounding up, lead to smaller CI values.

5.5 2D pyrolytic carbon electrodes for cell-based impedance sensing

The electrode size and geometry is an important parameter which can be tuned in order to increase the sensitivity of the measurement towards the detection of the investigated biological events [187,196‑200]. The electrode configuration used in cell-based impedance studies depends on the areas of the working and counter electrodes. The model introduced by Giaever and Keese consists of an electrode with small WE and a

larger CE [173]. The other widely used configuration are the interdigitated electrodes, where WE and CE have the same dimensions. Both configurations are available in commercialized systems, such as the ECIS® and xCELLigence® platforms. In this study the configuration with smaller WE surface area was used. All the cell-based impedance experiments were performed using 2D pyrolytic carbon electrodes obtained with the optimized pyrolysis process (Paper II). The chips were produced using conventional UV-photolithography with the same fabrication process of the 2D electrodes introduced in section 2.5.2. The electrodes used for cell-based applications are characterized by an insulating layer of SU-8 partially covering the WE, with 19 circular openings with a diameter of 250 μm (Figure 5.9).
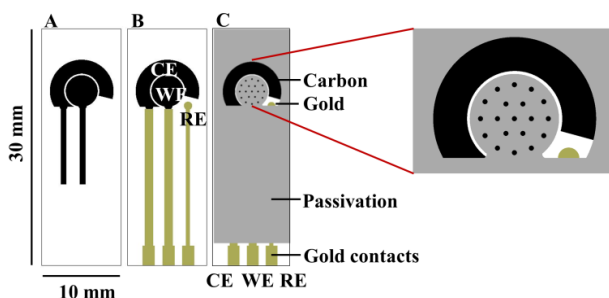
Figure 5.9: Overview of 2D dots carbon electrodes: carbon layer (A), gold contact leads and pads (B), SU-8 passivation layer (C).

The chips (2D dots) were characterized in the same way as the 2D electrodes without patterned passivation layer, using CV and EIS. As it can be seen in Figure 5.10, the reduction of the total WE sensing area is reflected in the electrochemical behaviour of the electrodes. The 2D electrodes show higher peak currents and lower charge transfer resistances R_{ct} values due to the higher surface area (Table 5.1). All these parameters are surface area dependent and are in agreement with the WE area calculations.

Table 5.1: Comparison 2D vs 2D dots electrodes: Surface area, anodic peak current and R_{ct} values (average $\pm$ standard deviation, n=3).

	2D	2D dots
WE surface area (mm^2)	12.56	0.93
Anodic peak current (μA)	374.9 $\pm$ 14.9	22.7$\pm$1.2
R_{ct} (Ω)	680.4±111.13	6019.3±1083.1
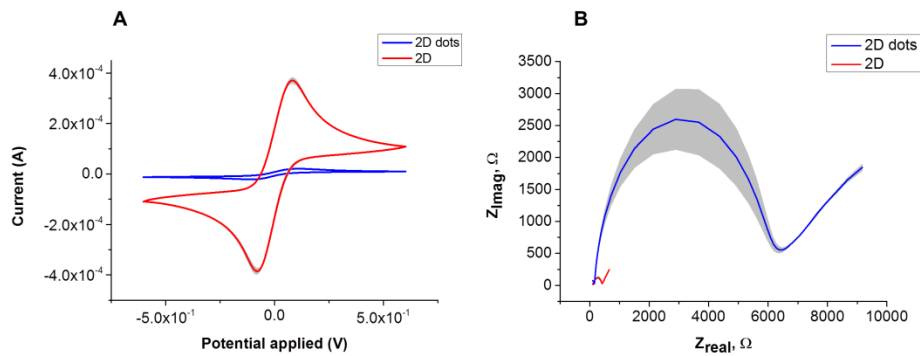
Figure 5.10: Cyclic voltammograms (A) and Nyquist plot (B) of 2D (red) and 2D (blue) dots pyrolytic carbon electrodes acquired in 10mM ferri-ferrocyanide. Data are presented as mean $\pm$ standard deviation (n=3).

The electric field distribution is affected by the electrode geometry (Figure 5.11) [201,202]. The area reduction of the WE creates a bottleneck effect for the current flow when identical potential are applied. The changes which occur at the smaller WEs dominate the impedance measurement compared to the larger CE [203].
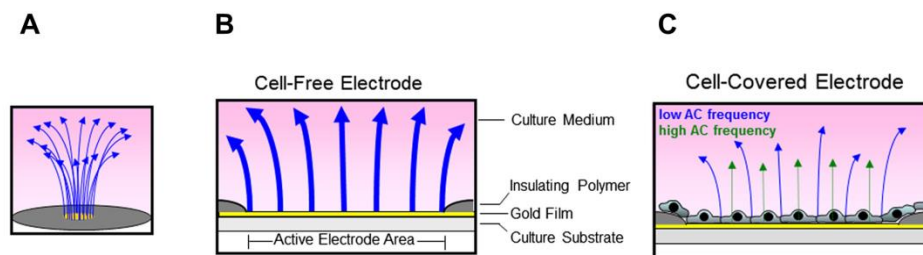
Figure 5.11: Schematic illustration of the electric field lines compression at the small opening on the WE (A). Electrode behaviour in absence (B) and presence of cells (C). Figure modified and reproduced from [203].

Initial experiments performed previously from our group showed that EIS-based monitoring with standard 2D electrodes was not possible. In this work, 2D dots pyrolytic carbon electrodes have been used to monitor the adhesion and proliferation of the human osteosarcoma cell-line Saos-2. This cell line was chosen since it exhibits the most mature osteoblastic labelling profile, being a good model for the study of osteoblast differentiation [142,204]. All the impedance monitoring of Saos-2 cells experiments were performed applying a sinusoidal perturbation potential of 0,1 mV and

recording 10 points/decade in the frequency range between 100 Hz and 100000 Hz. Parallel control experiments where no cells were seeded were run. As explained in detail in Paper III, EIS was first used to correlate cell density and CI values. Various Saos-2 cell densities (20000, 40000 and 60000 cells/cm^2) were seeded on fibronectin-coated 2D dots electrodes and monitored continuously for 40 hours in order to determine the optimal cell density range (Figure 5.12). Based on this information, 10 days an 21 days impedance experiments were performed to monitor cell behaviour during differentiation experiments.
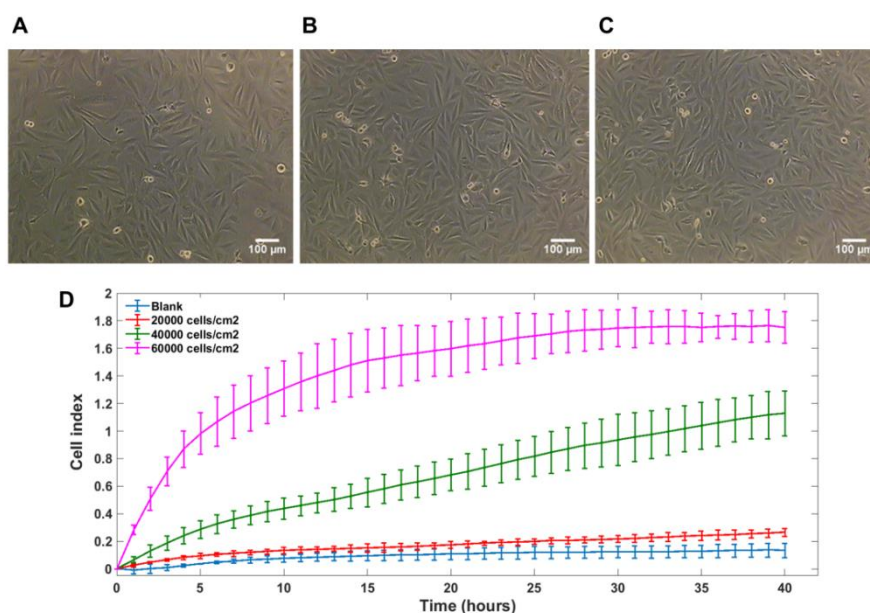
Figure 5.12: Optical microscopy images of Saos-2 cells: 40 h after seeding at a density of 20x103(A), 40x103 (B), 60x103 (C) cells/cm^2 on Fibronectin-coated PS, 10x magnification .Time evolution of the CI values for different Saos-2 cell densities recorded on Fibronectin-coated 2D dots chips (D). Data are presented as mean±standard deviation (n=3).

5.6 Electrochemical detection of ALP activity of Saos-2 cells

5.6.1 Alkaline phosphatase

As explained in section 5.2.1, the osteoblast differentiation process can be divided into three stages: proliferation, extracellular matrix production and mineralization. During

these stages various markers such as type I collagen, non-collagenous proteins and alkaline phosphatase are expressed [148,205]. In particular ALP expression occurs after type I collagen production, and reaches the maximum level of activity just before mineralization [148]. ALP is an enzyme attached to the external surface of the plasma membrane via a glycosyl-phosphatidylinositol (GPI) anchor [206‑208]. It is present in various mammalian cells and has a fundamental importance in the bone matrix mineralization process [206,207]. Besides from bone, in humans it is present in various other tissues, including intestine, kidney, liver and placenta. In the bone it represents a marker of the late differentiation process of osteoblasts. Its main functions consist in the hydrolysis or transphosphorylation of various phosphate compounds. The catalysis of the hydrolysis of phosphomonoesters ($R-O-PO_3$) occurs at alkaline pH in the catalytic sites, which consist of three metal ions, two Zn and one Mg [206,207]. The results of the reaction are alcohol and inorganic phosphate (Figure 5.13).

Phosphate monoester   **Alcohol**   **Phosphate**
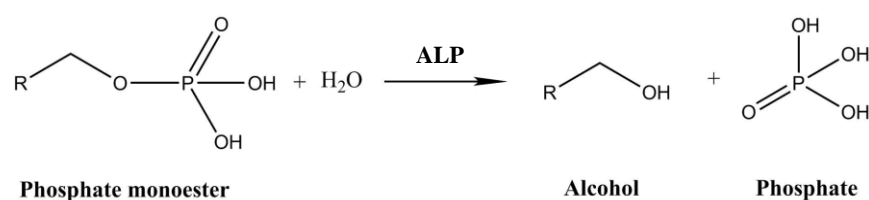
Figure 5.13: Hydrolysis of phosphate monoester catalyzed by alkaline phosphatase.

Physiologically, the role of ALP is to generate inorganic phosphate which is important for the hydroxyapatite crystallization in the bone matrix. Moreover ALP hydrolyses pyrophosphate, a mineralization inhibitor which prevents hydroxyapatite precipitation and growth [209,210]. Thus, ALP represents an osteoblastic differentiation marker, and its activity coincides with bone formation *in vivo* and *in vitro* [142,207,211]. For example it has been used to monitor the osteogenic status of human mesenchymal stem cells (hMSCs) in 2D and 3D cell cultures and to investigate the proliferation and differentiation behaviour of human bone marrow cells cultured in various osteogenic media [212,213]. Moreover, ALP monitoring was used in various cell-implant *in vitro* systems in order to study osteoblast attachment, secretion of extra cellular matrix proteins and mineralization [214,215].

5.6.2 Alkaline phosphatase detection techniques

The expression of ALP can be detected and assessed using various techniques. Reverse transcription polymerase chain reaction (RT-PCR) is based on the extraction of RNA from cells and the examination of gene expression [216]. Western blot consists in the use of an antibody specific for ALP in order to form an antibody-antigen complex and apply electrophoresis methods to detect the presence of ALP. These conventional techniques are time-consuming, labour-intensive and do not provide real-time observation since they require cell lysis [217]. ALP can also be detected *in vitro* with the use of colorimetric assays [218]. By using 4-nitrophenylphosphate (pNPP) as substrate, the compound can be catalytically hydrolysed to form 4-nitrophenol (pNP) (Figure 5.14). pNP can be then detected and quantified using a spectrophotometer to evaluate the absorption peak at 405 nm. ALP activity can be indirectly calculated using a calibration curve.
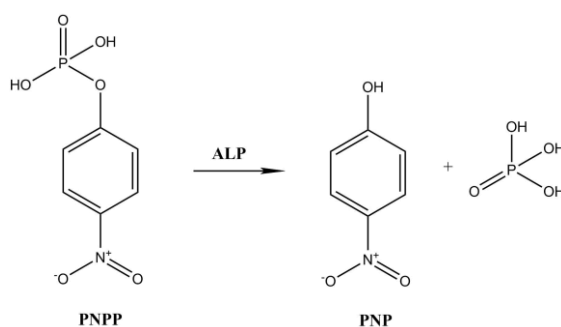
Figure 5.14: pNPP substrate converted in pNP through ALP action.

Another available technique is a staining which uses BCIP-NBT (5-bromo-4-chloro-3-indolyl phosphate/nitroblue tetrazolium) as substrate [219]. The assay is based on the reaction between ALP and BCIP. ALP separates the phosphate group from the BCIP and produces a proton which reduces NBT to an insoluble purple precipitate [150]. Fluorimetric assays use 4-methylumbelliferyl phosphate disodium salt, a sensitive substrate for ALP in ELISA procedures. When the phosphate group is divided from the salt by ALP, a fluorescent compound (4-Methylumbelliferone) is obtained, which can be quantified through the intensity of its signal using a microplate reader [220]. In

general, these techniques use either antibodies or various biomolecules, are difficult to automate and are time consuming. Electrochemical techniques offer the possibility to non-destructively measure ALP [221]. The assay consists in the use of p-aminophenyl phosphate (pAPP) as substrate for the reaction with ALP which catalytically hydrolyses it to p-aminophenol (pAP). pAP is then quantified using electrochemistry to detect the current obtained from the oxidation to p-quinone imine (pQI) (Figure 5.15). ALP is indirectly quantified from the obtained current value. The main advantage of this assay is the fact that compared to the previous techniques it is relatively fast, sensitive and offer the possibility to be automated [222].
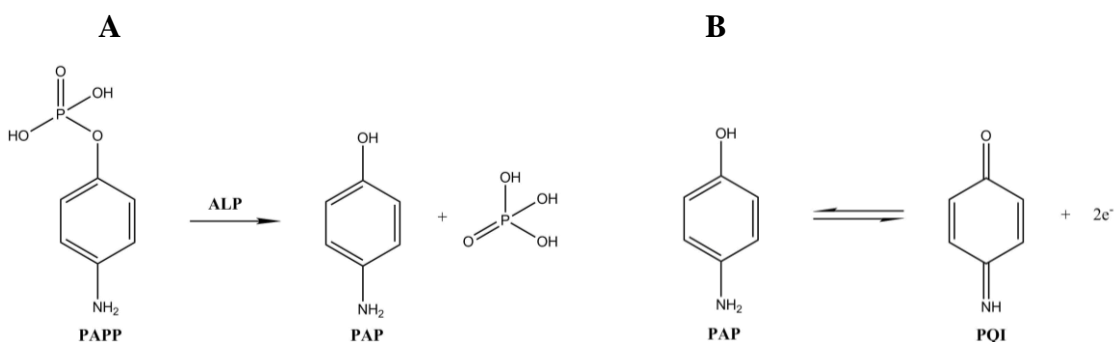
Figure 5.15: Electrochemical assay for ALP detection. Enzymatic reaction (A) and electrochemical reaction (B).

In this thesis, to monitor the ALP activity of Saos-2 cells during the differentiation process, the described electrochemical assay was used (Figure 5.16). The cells were seeded and cultured on 2D dots pyrolytic carbon electrodes. Subsequently, cells were incubated with pAPP to allow the enzymatic reaction to take place. Square wave voltammetry was used to measure the pQI oxidation peak and thus calculate the ALP activity with the use of a calibration curve. Cells were cultured in growth medium, and in medium supplemented with differentiation factors (Paper III).
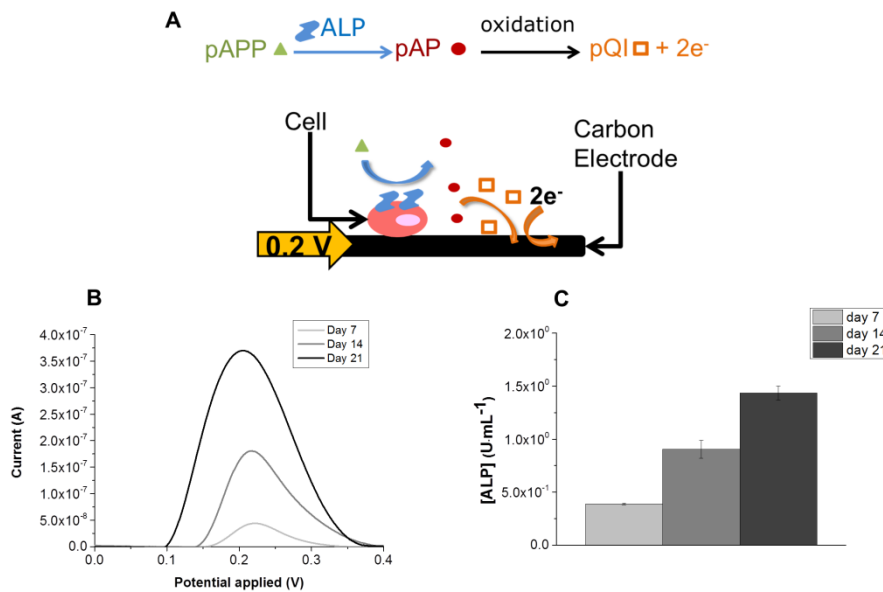
Figure 5.16: Electrochemical assay for ALP detection in 2D cells culture (A). Cells (in pink) express ALP on their outer membrane (in blue). P-aminophenyl phosphate (pAPP, in green) is introduced and catalytically hydrolyzed to p-aminophenol (pAP, in red) by ALP activity. The resulting pAP is oxidized to p-quinone imine (pQI, in orange) on the surface of the electrode (in black) and an oxidation current is measured. Representative SW voltammograms for Saos-2 cells grown in growth medium for recorded at day 7, 14, 21 (B) and time course of ALP (C).

6. Monitoring of 3D cell cultures

This chapter discusses the use of 3D pyrolytic carbon electrodes for the development of a 3D *in vitro* model similar to osseous tissue for bone diseases research and drug development applications. The electrodes were used for *in situ* monitoring and quantification of ALP activity of a 3D osteoblastic cell culture. The chapter starts with a description of the limitation of 2D *in vitro* systems, followed by an introduction to 3D cell culture models and the techniques used to monitor cellular dynamics in 3D cultures. Finally, the 3D pyrolytic carbon pillar electrodes are introduced and their use for the monitoring of ALP activity of Saos-2 spheroids embedded in gelatin is described.

6.1 Introduction

Within a tissue, cells interact with the neighbouring cells and the extracellular matrix (ECM) using mechanical and biochemical signals, creating a network which maintains the homeostasis and the specificity of the tissue [223]. The ECM is composed of proteins such as collagen, laminin and fibronectin interlaced with proteoglycans [9,224]. It has different functions in processes such as cell growth, proliferation, differentiation, spatial arrangement and tissue formation [9]. As introduced in chapter 5, nowadays cell-based assays are typically performed on traditional 2D *in vitro* systems. The main limitation is that this geometry poorly mimics the natural 3D environment which is experienced by cells in tissues where they are surrounded by other cells and extracellular matrix [9,10]. Even though the use of 2D systems has contributed tremendously to the field of cell biology, cells on a flat substrate grow flatter and more stretched compared to the behaviour observed *in vivo* [10]. The lack of a 3D environment could for example lead to wrong predictions of cell response when testing a new drug formulation due to the impossibility to model the complex behaviour of a biological system with various cells interaction [10,225‑227]. The use of 3D cell cultures could hence improve the physiological relevance of the *in vitro* assays and

increase the prediction accuracy of cell-based drug and toxicity screening [10,226,228,229].

6.2 3D cell culture models

Currently, 3D cell cultures are used in various research fields such as cell biology studies, cell adhesion, epithelial morphogenesis, cell migration and tumour biology [228]. 3D culture models, depending on their nature and function, can be classified into different groups: organotypic explant cultures, cell spheroids, tissue-engineered models and microcarrier cultures (Figure 6.1) [228,229]. Not all the techniques require a scaffold to recreate a 3D cellular microenvironment. For example, organotypic explant cultures consist in dissected organ slices placed on porous substrates supported by a metal grid and immersed in growth medium. This kind of model is used to acquire data when tissue-specific information is needed. Among the available models, cellular spheroids are particularly interesting. They form due to the tendency of
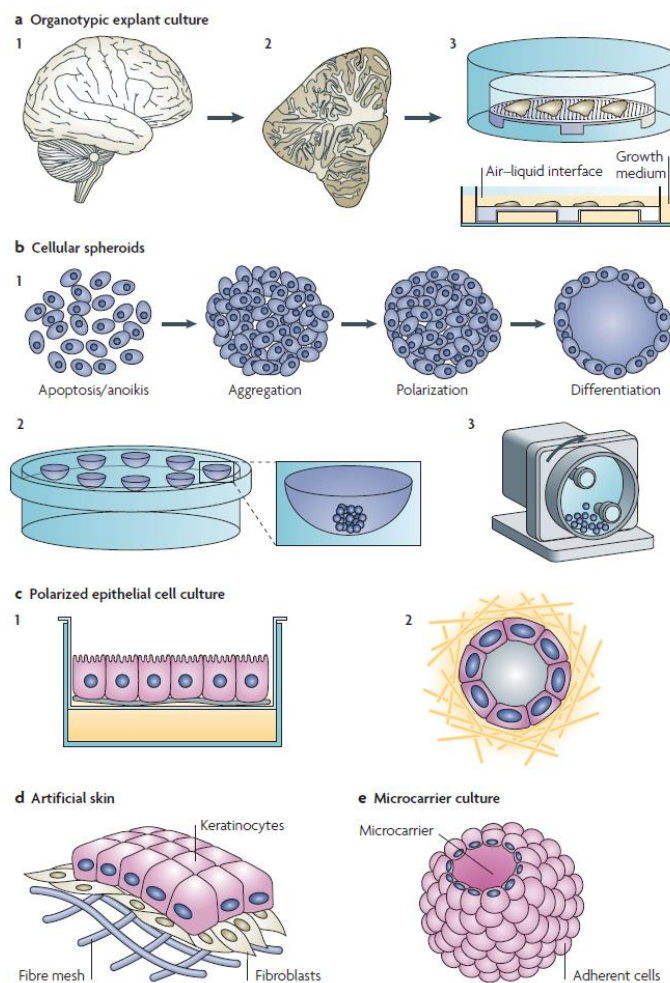
Figure 6.1: 3D culture models: Organotypic explant culture (a), cellular spheroids (b): endothelial cells cluster (1), "hanging drop" (2) and rotating-wall vessels (3) techniques. Polarized epithelial cell cultures (c), artificial skin (d) and microscaled materials (microcarrier) (e). Figure reproduced from [228].

aggregation of a wide range of cell types. With this arrangement, spheroids with dimensions of several hundreds of micrometres can be formed, and cells can again establish an environment which through mutual contacts allows them to express tissue-like characteristics. These structures can be obtained with various techniques. For example with forced floating methods, where cells aggregate spontaneously in a vessel with a surface covered with non-adhesive coatings, or techniques such as the "hanging drop" or the rotating-wall vessels, where cells cluster by gravity and aggregate [226]. In particular, the main advantage of cellular spheroids is that they do not require an external scaffold to aggregate. They can be obtained from single cultures or co-cultures and are widely used in the field of oncology, since they can simulate the behaviour of tumours more accurately than two dimensional cultures [230,231]. Spheroids can be produced in mass quantities and optimized for the selection of effective compounds in preclinical studies [232,233]. For this reason this model has also been used in high throughput screenings and is the model used in this work. Other used models are for example the polarized epithelial cell culture, artificial skin and microcarriers. These models will not be discussed since their description is beyond the scope of this thesis.

Various studies provide evidence of the advantages of 3D cell culture systems, especially when compared to 2D monolayer cultures. However, to move from 2D to 3D models, many aspects need to be optimized, such as imaging techniques or sample handling and vascularization in order to provide oxygenation, nutrients and waste removal [224,227,228].

6.3 Monitoring cell fate in 3D *in vitro* models

The evaluation of cell viability and metabolic activity within the 3D culture is still a challenging aspect. The traditional cytotoxicity assays represent simplistic methods which do not take into account spatial distribution of cells and do not provide temporal information [234]. More in general, traditional methods such as histological and biochemical assays are destructive, require various sample processing steps and are end point measurements [235]. A minimally invasive and non-destructive approach consists in the imaging of the 3D cell culture, which allows getting a dynamic quantitative

analysis of the biological structures. Even if improvements have been demonstrated in the field of optical microscopy, these techniques still have some limitations, which make them less suitable for the imaging of highly scattering samples that are hundreds of μm thick [228]. The state of the art technique is confocal fluorescence microscopy, which provides a better spatial resolution compared to other imaging techniques. However, its main drawbacks are the limited penetration depth, the photo bleaching and phototoxic effects caused by the excitation light which extends to all the analysed planes [228]. Moreover, the analyses carried out using this imaging technique require high quality images, involve complex processing algorithms and are generally time consuming [235]. Another example is two-photon microscopy, which allows a higher penetration depth. However, this technique has a lower resolution and requires a larger light intensity which can have phototoxic effects on the plane in focus [236]. Tomographic techniques can be also used to image the sample from different angles. The various images acquired are then merged to a final dataset [237]. Also in this case the main drawbacks are the spatial resolution and the time required for the acquisition of the images.

To overcome these limitations and to achieve a non-destructive monitoring of 3D cultures, cells can be incorporated with a biosensor. Among the available biosensors, electrochemical sensing platforms are the one most commonly used [227]. This method allows the non-invasive monitoring of cell fate, providing at the same time measurements with high accuracy and sensitivity [238]. As described in chapter 5, electrochemical techniques have several advantages compared to traditional methods for 2D cell cultures. Several attempts have been made to maintain these benefits also for 3D cell cultures, typically using spheroids and cells embedded in various matrixes as 3D culture models [227]. For example Lin *et al.* monitored cell growth with impedance by incorporating a 3D culture of fibroblasts in synthetic hydrogel on a 2D electrode (Figure 6.2A) [239]. Jeong *et al.* used a similar approach, growing lung cells embedded in alginate, Matrigel or collagen on a flat electrode, in order to monitor cell response to an anticancer drug [240]. Other studies focused on the direct measurement of the variation

of electrical properties of spheroids. For example, micro capillary systems were manufactured in order to measure the impedance of the spheroids by positioning electrodes on both open ends of the measuring setup (Figure 6.2B) [212,241]. In this case the measurement of electrical characteristics such as extracellular and intracellular resistance and cell membrane capacitance were used to investigate the behaviour of the spheroids. Another study demonstrated, through the use of micro cavity systems, that higher values of the spheroid impedance due to the changes in the morphology of the outer cells were associated with drug-induced apoptosis [242].
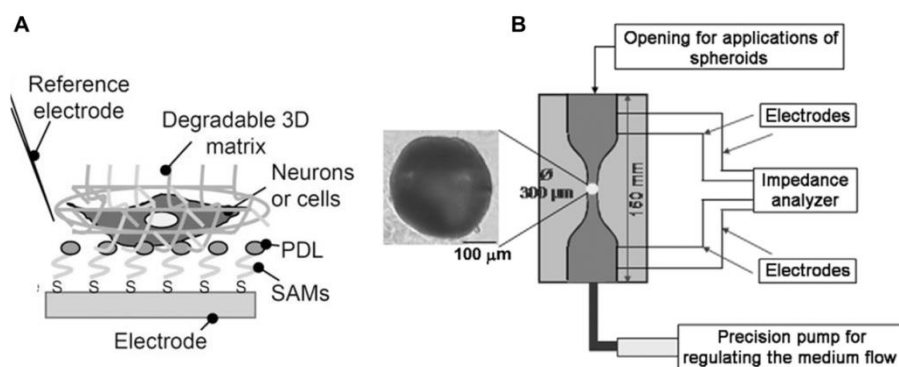
Figure 6.2: Schematic of flat electrode with 3D cell culture embedded in a degradable matrix (A) and the capillary-based device used for the characterization of human mesenchymal stem cells (hMSC) with integrated electrodes (B). Figures reproduced from [239] and [212] respectively.

In all the reported examples, the 3D culture was simply placed on top or in proximity of 2D electrodes. This leads however to a decrease in the sensing of events taking place in the "bulk" of the 3D cell culture, where the distance from the electrodes surface is higher compared to the cells closer to the electrode. Ideally, the electroanalytical sensor should be integrated in the 3D cell culture, combining both the structural support function and the electrochemical sensor for the *in situ* monitoring. Various studies have been carried out focusing on the investigation of 3D sensing scaffolds [243‑246]. In particular Amato *el al.* exploited the biocompatibility of pyrolytic carbon and its favourable properties as electrode material to fabricate 3D carbon scaffolds for the monitoring of human neural stem cell differentiation and the sensing of dopamine [40]. When compared to flat carbon electrodes, the electrochemical monitoring of the cells

was considerably improved. This could be mainly attributed to the enhanced interaction of the cells with the carbon microelectrode substrate combined with the increase in the surface area. However the used carbon structures were around 11 μm, which is not comparable to the several hundreds of μm of cell cultures in hydrogels. For this reason, in this thesis the fabrication process used to obtain 2D pyrolytic carbon electrodes was modified in order to obtain 200 μm carbon pillars on the WE. The 3D electrode was used to monitor and quantify *in situ* the ALP activity of Saos-2 cells embedded within a gelatin hydrogel. The 3D pyrolytic carbon structure was used to mimic the *in vivo* bone architecture (described in section 5.1). More precisely, pyrolytic carbon has a Young's modulus between 10 and 40 GPa [44], which is similar to one of cortical bone (around 20 GPa [247]). The hydrogel was used instead to recreate the *in vivo* cellular microenvironment (Paper IV). This allows the cells to experience more *in vivo* like spatial interactions, such cell-cell and cell-ECM interactions.

6.4 3D pyrolytic carbon pillar electrodes

The 3D pyrolytic carbon electrodes were designed in order to have a sufficient pillar height to allow cell growth within a gelatin layer of around 300 μm. Electrodes with different pillar spacing were fabricated in order to investigate the influence of the scaffold design on the formation of the spheroids.

The 3D carbon pillars on the WE were obtained by adding a UV photolithography step to the process flow used to fabricate the 2D electrodes (section 2.5.2). SU-8 2075 was spin coated in order to obtain a 500 μm thick layer. UV exposure followed by a post exposure bake was used to obtain pillars with a diameter of 100 μm. Three pitch distances between pillars were used to fabricate three designs: 400 μm (design 1, 64 pillars), 300 μm (design 2, 133 pillars) and 200 μm (design 3, 284 pillars). After pyrolysis, the average height of the pillars measured with an optical profilometer was 224.5±0.8 μm, while the diameter was 68.3±1.5 μm for all the wafers (Figure 6.3).
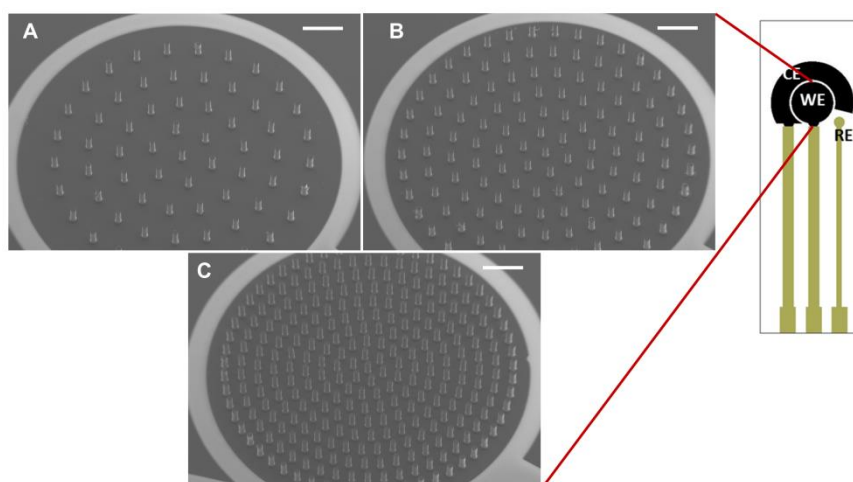
Figure 6.3: SEM images of 3D carbon pillars on the WE: Design 1 (A), Design 2 (B), and Design 3 (C). Scale bar: 500 μm.

Depending on the design, different surface areas were calculated, as reported in Table 6.1. The electrodes were electrochemically characterized using cyclic voltammetry and impedance spectroscopy with the standard redox probe $[Fe(CN)_6]^{3-/4-}$.

Figure 6.4A shows the acquired CVs for 2D and 3D pillar electrodes with carbon CE and Au RE. The 3D design with lower pitch distance and higher number of pillars showed a higher peak current (1.8 times higher) compared to the 2D one due to the increase of surface area. A trend related to surface area was observable also in the EIS measurement, where the 3D electrodes showed lower R_{ct} values (Figure 6.4).
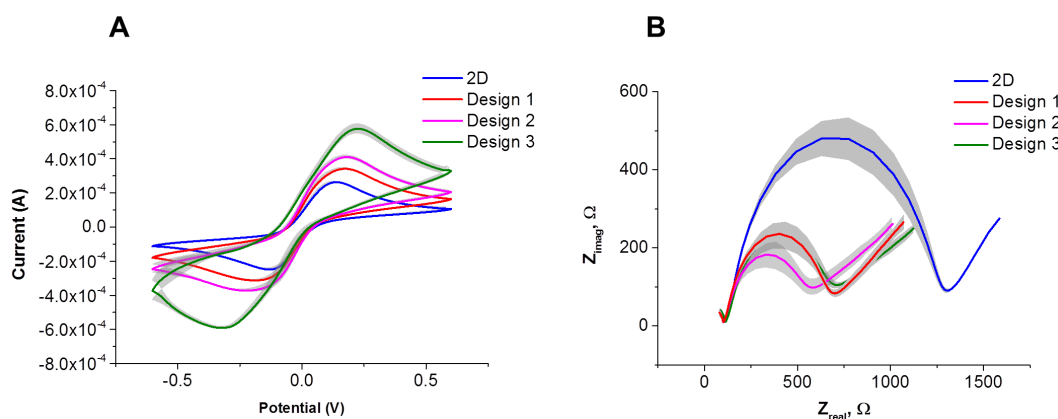
Figure 6.4: Voltammogram (A) and Nyquist plot (B) of 2D and 3D pyrolytic carbon electrodes acquired in 10mM ferri-ferrocyanide. Data are presented as mean $\pm$ standard deviation (n = 3).

Table 6.1: Surface area calculation and anodic peak currents of 2D and 3D carbon electrodes.

	2D	**design 1**	**design 2**	**design 3**
Number of pillars	/	64	133	284
WE Carbon area	12.56 mm^2	15.44 mm^2	18.54 mm^2	25.34 mm^2
Anodic peak current (μA)	254$\pm$6.8	311$\pm$10.7	371$\pm$14.3	459$\pm$23.2
R_{ct} (Ω)	1191.6$\pm$98.2	617.7$\pm$43.3	536.6$\pm$95.9	650.2$\pm$82.2

7. 3D pyrolytic carbon electrodes in miniaturized biophotovoltaic systems

In this chapter the use of 3D pyrolytic carbon electrodes in biophotovoltaic cells is described. A short introduction on the promising advantages of energy harvesting from photosynthetic organisms for the supply green energy is provided. Then, the electron transfer in a biophotovoltaic system is explained and the 3D pyrolytic carbon pillar electrodes with Pt CE and RE are described. Finally, the preliminary results of the recorded photocurrent generated from cyanobacterial cells using both 2D and 3D electrodes are presented.

The work reported in this chapter is the result of the work carried out during two external stays in the group of Prof. Chris Howe from the department of Biochemistry at the University of Cambridge.

7.1 Introduction

Nowadays, the growing need for energy from fossil fuels has had tremendous consequences on the environment, and the simultaneous depletion of fossil fuel reserves has drawn the attention to the research on alternative clean energy sources [249‑251]. Among the various renewable energies available, the field of biophotovoltaics represents a promising technology for the alternative generation of electricity [252‑254]. Systems such as microbial fuel cells (MFCs) and biological photovoltaic cells (BPV) use living organisms as catalyst to generate electrical energy through bioelectrochemistry. In particular these organisms are able to self-repair, reproduce and even store energy for power generation in the dark. However, BPVs still provide low conversion efficiencies of light into current and for this reason the research over the last few years has focused on their improvement and on the understanding of the reasons limiting their performance [252]. Here, the use of pyrolytic carbon electrodes as anode

material in miniaturized mediator-less biophotovoltaic cells was investigated. These systems could be used to investigate the processes limiting the performance of BPVs or to develop sustainable energy conversion and storage systems.

7.2 Energy generation using photosynthetic organisms

BPVs use oxygenic photosynthetic organisms which are able to harvest the energy from light and generate a current without the need of an organic feedstock [253]. The photosynthesis happens in the thylakoid membranes, placed inside the chloroplast [255]. The light reactions are performed by transmembrane protein complexes, which once triggered by light perform the water-splitting reaction and the synthesis of ATP and nicotinamide adenine dinucleotide phosphate (NADPH). In the dark reactions (Calvin cycle), ATP and NADPH are then used to fix CO_2 and synthetize
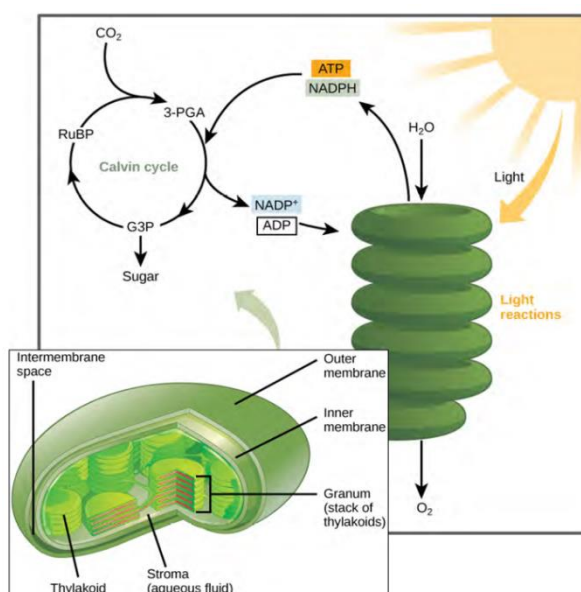
Figure 7.1: Schematic of light reactions responsible for the conversion of light energy into ATP and NADPH. Dark reactions (Calvin cycle) use ATP and NADPH to convert CO_2 into organic molecules. RuBP(ribulose-1,5-biphosphate), 3PG (3-phosphoglycerate) and G3P(glyceraldehyde 3-phosphate). Inset: schematic of chloroplast. Figure reproduced from [255].

other organic molecules such as sucrose, starch, proteins and fats (Figure 7.1) [256]. The development of a miniaturized BPV is interesting since it would allow high-throughput studies with small microbial cultures and operation without the use of a proton-exchange membrane, increasing the efficiency and the simplicity of the device [254]. Furthermore, the decrease in the length scale of charge transport might result in reduced resistive losses in the electrolyte. BPV cells usually consist of oxygenic photosynthetic organisms located on the anode, a cathode and typically a proton

permeable membrane. The biological components which can be used as photosynthetic systems are microorganisms such as algae [252] or cyanobacteria [254,257], thylakoid membranes extracts [258] or photosystems I and II [259,260]. In the case of cyanobacteria, the microbes are cultured on the anode, while the cathode consists of a catalytic material. Current production occurs once there is a potential difference between the reactions happening at the anode and at the cathode (Figure 7.2).
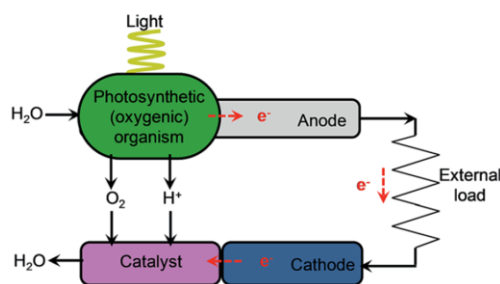
Figure 7.2: Electron transfer in a biophotovoltaic system. The catalyst at the cathode promotes the electron acceptor reaction. Figure reproduced from [253].

The extracellular electron transfer to the anode can take place directly or indirectly. In the direct extracellular electron transfer (DEET) based systems, the electron transport does not require a mediator. In this case, the formation of the biofilm on the anode is important because it ensures a physical contact and direct electrical connection between the microbes and the electrode. The advantage of these systems is that the lack of the mediator increases the simplicity of the device and reduces the costs in case of potential large-scale applications [254]. However, for the moment mediator-less BPVs are able to harvest only below 0.3% of the input energy [252,254]. In order to increase the efficiency of BPVs cells the research has focused mainly on three aspects: i) the genetic engineering of the cyanobacteria in order to improve the electron transfer, ii) the investigation of new mediators which allow more efficient electron transfer to the anode and iii) the study of new anode materials and geometries. Most of the efforts have been directed toward the first two research fields, while less attention was given to the electrode characteristics. The most used electrode material for the anode in BPVs is carbon, available for example as fibrous material (felt, cloth, paper, fibers, foam) and as glassy carbon [261]. Recent studies have shown that an improved efficiency was

achieved with the use of microporous reduced graphene oxide electrodes, probably due to an increased surface area. In fact, growing the bacterial films on 3D electrodes could facilitate the harvest of the electrons released by the microorganisms even in the bulk of the biofilm, due the proximity of the sensing electrodes. To our knowledge, the influence of 3D microfabricated electrodes on the electron harvesting efficiency in BPV systems has not been investigated. In this thesis, pyrolytic carbon electrodes were used for the investigation of current generation from photosynthetic microorganisms in miniaturized biophotovoltaic cells. First, modified 2D electrodes with Pt counter and reference electrode were used to investigate the interaction of cyanobacterial cells (*Synechocystis sp*. PCC 6803) with pyrolytic carbon substrates. Then, the performance of BPV systems using 2D and 3D electrodes was compared in order to assess if the presence of a three dimensional electrode can improve the electron harvesting process.

7.3 Photocurrent generation from cyanobacterial cells

The 3D pillars electrodes were fabricated also with Pt CE and RE for biophotovoltaic applications, since platinum catalyses the reduction of H^+ at the cathode and is one of the typical materials used in biophotvoltaic cells [254]. As expected, the same trend in the cyclic voltammograms reported for the 3D electrodes with Au RE (section 6.4) was observable for these electrodes when compared with 2D electrodes with Pt CE and RE (Figure 7.3).
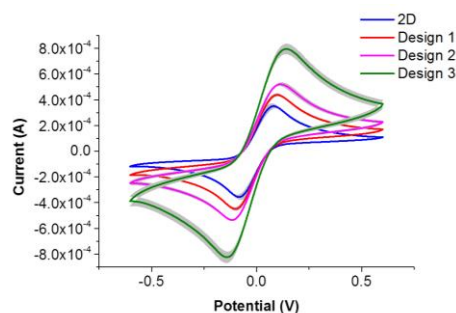
Figure 7.3: Voltammogram of 2D and 3D pyrolytic carbon electrodes with Pt CE and RE acquired in 10mM ferri-ferrocyanide. Data are presented as mean $\pm$ standard deviation (n = 3).

The experiments were performed by initially seeding 100 (nmol Chl)·ml^{-1} of cyanobacterial cells into the magnetic clamping system containing the carbon chip. BG11 medium was used as culture medium. 10 µl of concentrated cell suspension were placed on the working electrode and cells were allowed to sediment for approximately 2 hours. After sedimentation, 300 µl of BG11 medium were added into the chamber. In order to investigate the electrochemical performance of biotically modified anodes chronoamperometry measurements at 0.2 V were run in dark and light conditions. Artificial light was obtained by using a white LED bulb maintained at a constant output photon flux of 200 µmol·m^{-2}·s^{-1} (corresponding to a light intensity of 42 W/m^2) (Figure 7.4) [254].
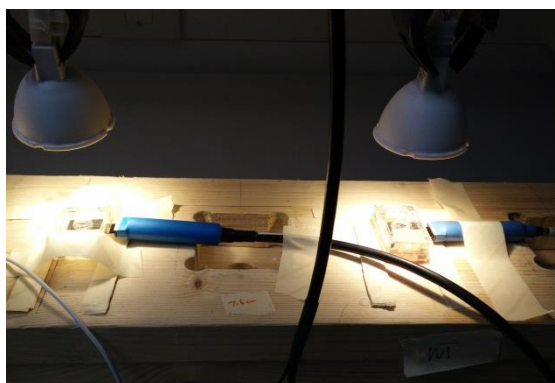
Figure 7.4: Setup used to perform the electrochemical measurements: the batch systems containing the chips were connected to the potentiostat through a connector (in blue) and positioned under a white LED bulb.

The light was switched on and off every two hours. Figure 7.5 shows the chronoamperometric anodic profile of the BPV system during the dark/light cycles using 2D carbon electrodes. As it can be seen, a light effect and the consequent current generation was observed, indicating that pyrolytic carbon electrodes are suitable for integration in miniaturized biophotovoltaic cells and for the investigation of current generation from photosynthetic microorganisms. When the light was switched on, the current increased instantly, after which it kept increasing very slowly. When the light was switched off, the current dropped to the value recorded before illumination. The same behavior was reported previously for *Synechocystis sp*. PCC 6803 embedded in a

microfluidic device [254], and more generally for other BPV systems containing photosynthetic microbes [262].
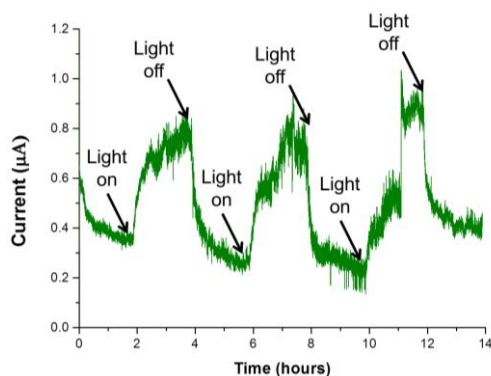
Figure 7.5: Chronoamperometric anodic current of BPVs during three dark/light cycles recoded on 2D pyrolytic carbon electrodes.

As a proof of concept, the same experiments were repeated using 3D carbon electrodes with Pt CE and RE, choosing the design 3 with most pillars in order to harvest as many electrons as possible from the biofilm (Figure 7.6). As it can be seen, a higher current was recorded by using the 3D electrode, indicating that the 3D carbon electrodes might represent a promising tool to improve the performance of BPV cells. Only few experiments were performed both for 2D and 3D electrodes and further experiments are required to confirm the results reported here.
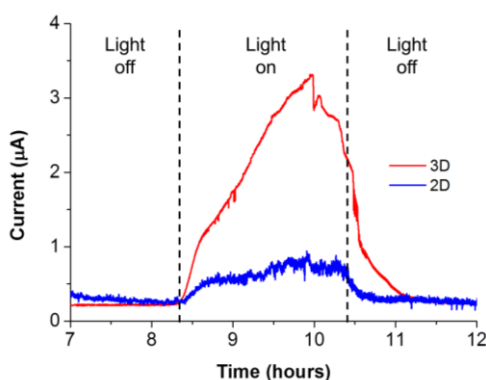
Figure 7.6: Comparison of chronoamperometric anodic current of BPVs during a dark/light cycle recoded on 2D and 3D pyrolytic carbon electrodes.

These preliminary experiments were included as proof of concept in a recently granted funding application for an ERC consolidator grant obtained by Associate Professor Stephan Sylvest Keller.

7.4 Electrospinning on 3D pillar electrodes

Finally, electrospinning was explored as fabrication method of hierarchical 3D polymer templates for the production of more random carbon scaffolds. This would allow more efficient electron transfer in BPV cells.

In order to obtain the carbon structure, PCL and chitosan fibers were electrospun on 3D SU-8 pillar electrodes before pyrolysis (Figure 7.7 A and C). An interesting structure consisting of suspended fibers was achieved before pyrolysis. However, the results after the heat treatment showed that the fibers did not survive the pyrolysis temperature of 900°C and thermally degraded, leaving just some traces on the top of the carbon pillars (Figure 7.7 B and D). The choice of polymer precursors for the fibers which are able to withstand temperatures of around 900°C could lead to the fabrication of complex 3D structures in carbon.
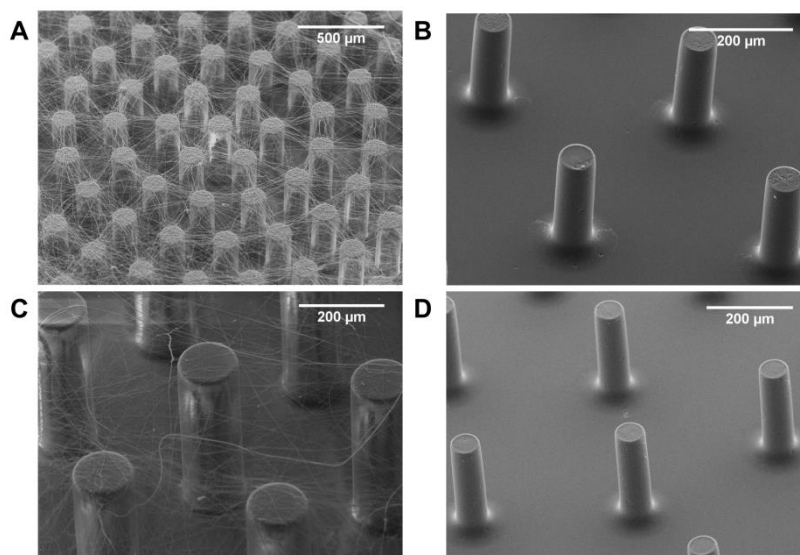
Figure 7.7: SU-8 pillars with PCL or chitosan fibers before (A and C) and after (B and D) pyrolysis.

8. Conclusions and outlook

The main focus of this multidisciplinary Ph.D. project consisted in the fabrication of 2D and 3D carbon electrodes obtained through pyrolysis, their optimization and their use in bioelectrochemical applications. 2D and 3D pyrolytic carbon electrodes represent a promising tool in the field of bioelectrochemistry. The possibility for customization in terms of shape and surface properties could enable the development of novel biosensors.

The research work focused firstly on the establishment of a stable, reproducible and optimized pyrolysis process for the fabrication of carbon electrodes. Once defined the optimal recipe through the analysis of the electrical and electrochemical properties of the carbon electrodes, the influence of various polymer precursors was investigated. The use of photoresists and lithographic techniques resulted to be the best method to obtain carbon electrodes with improved electrochemical properties. The fabricated electrodes showed excellent electrical properties, with resistivity values which are to our best knowledge the lowest ones reported for pyrolyzed photoresists films (Paper II).

Batch to batch variations with time were observed in terms of electrical and electrochemical performance. This can be mainly attributed to the ageing of carbon, demonstrating that the storage is an important parameter which influences the performance of the electrodes.

Pyrolytic carbon electrodes were then used for EIS monitoring of cell cultures. A human osteoblastic model cell line (Saos-2) was chosen to validate the electrodes for impedance-based cell assays. Adhesion and proliferation were assessed in real-time together with the monitoring and quantification of the activity of the bone differentiation biomarker ALP. Using the same electrochemical assay, 3D electrodes were used to monitor ALP activity in a three-dimensional cell culture (spheroids). The investigation of the properties of pyrolytic carbon electrodes and their application as *in vitro* cell model formed the basis for the development of the future generation of 3D cell scaffolds. An improvement that could be implemented in future studies is a more

reliable and stable batch system. The PMMA-based self-aligning magnetic clamping system was initially designed only for the electrochemical characterization of the electrodes, and not for long-term (3 weeks) cell experiments. The re-design of the batch system and the use of materials which can be autoclaved would avoid leaks and simplify the sterilization of the setup.

The studies performed on the 2D electrodes demonstrated the possibility to achieve a real-time monitoring of the differentiation of osteoblasts using pyrolytic carbon, both in terms of viability and expression of specific biomarkers (Paper III). The study performed on the 3D electrodes instead showed that using the same setup the monitoring and quantification of biomarkers can be achieved in a more *in vivo* like environment (Paper IV). This novel system could hence help the understanding of cellular dynamics, a key factor in the development of new therapies and drugs. More specifically, the results obtained with the study of the osteoblastic differentiation could support the investigation of the processes which control the complicated mechanism of bone resorption and regeneration, providing a deeper insight in the understanding and treatment of bone diseases.

Exploiting the freedom of the fabrication process, the design of the electrodes was modified in order to fulfil the requirements for their application in biophotovoltaic cells. For the first time pyrolytic carbon was used as anode in miniaturized BPV systems to investigate the current generation from cyanobacteria. As proof of concept, the interaction between 3D electrodes and biofilm was investigated. The introduction of a conductive scaffold allowed the recording of a higher photocurrent. This finding is very promising since it implies that the relative low efficiency of BPV systems can be improved by modifying the design of the electrode. Further studies need to be performed in order to understand the biofilm formation of the WE.

A possible application of the obtained BPV systems could for example be the fabrication of compact energy systems for portable devices. This idea will be further developed in the Pyrolysed Hierarchical Organic Electrodes for sustaiNable

Bibliography

[1]   J. El-Ali, P.K. Sorger, K.F. Jensen, Cells on chips, Nature. 442 (2006) 403–411. doi:10.1038/nature05063.

[2]   E. Michelini, L. Cevenini, L. Mezzanotte, A. Coppa, A. Roda, Cell-based assays: Fuelling drug discovery, Anal. Bioanal. Chem. 398 (2010) 227–238. doi:10.1007/s00216-010-3933-z.

[3]   K. Slater, Cytotoxicity tests for high-throughput drug discovery, Curr. Opin. Biotechnol. 12 (2001) 70–74. doi:10.1016/S0958-1669(00)00177-4.

[4]   N.J. Evans, T.L. Riss, High-throughput assays to assess different cytotoxicity assays for the assessment of cytotoxicity, in: High-Throughput Screen. Methods Toxic. Test., JohnWiley, 2013.

[5]   J. Wang, C. Wu, N. Hu, J. Zhou, L. Du, P. Wang, Microfabricated electrochemical cell-based biosensors for analysis of living cells in vitro, Biosensors. 2 (2012) 127–170. doi:10.3390/bios2020127.

[6]   L. Nyholm, Electrochemical techniques for lab-on-a-chip applications, Analyst. 130 (2005) 599. doi:10.1039/b415004j.

[7]   C. Spegel, A. Heiskanen, L.H.D. Skjolding, J. Emnéus, Chip based electroanalytical systems for cell analysis, Electroanalysis. 20 (2008) 680–702. doi:10.1002/elan.200704130.

[8]   K.L. Adams, M. Puchades, A.G. Ewing, In vitro electrochemistry of biological systems, Annu. Rev. Anal. Chem. (2010) 1–23. doi:10.1146/annurev.anchem.1.031207.113038.In.

[9]   T.P. Kraehenbuehl, R. Langer, L.S. Ferreira, Three-dimensional biomaterials for the study of human pluripotent stem cells, Nat. Methods. 8 (2011) 731–736. doi:10.1038/nmeth.1671.

[10]   H. Page, P. Flood, E.G. Reynaud, Three-dimensional tissue cultures: Current trends and beyond, Cell Tissue Res. 352 (2013) 123–131. doi:10.1007/s00441-012-1441-5.

[11]   J. Lee, D. Lilly, C. Doty, P. Podsiadlo, N. Kotov, In vitro toxicity testing of nanoparticles in 3D cell culture, Small. 5 (2009) 1213–1221. doi:10.1002/smll.200801788.

[12]   M. Shevach, B.M. Maoz, R. Feiner, A. Shapira, T. Dvir, Nanoengineering gold particle composite fibers for cardiac tissue engineering, J. Mater. Chem. B. 1 (2013) 5210. doi:10.1039/c3tb20584c.

[13]   T. Dvir, B.P. Timko, M.D. Brigham, S.R. Naik, S. Sandeep, O. Levy, H. Jin, K.K. Parker, R. Langer, S. Daniel, Nanowired three dimensional cardiac patches, Nat Nanotechnol. 6 (2012) 720–725. doi:10.1038/nnano.2011.160.Nanowired.

[14]   S.R. Laleh Ghasemi-Mobarakeh, M. P. Prabhakaran, M. Morshed , M. H. Nasr-Esfahani, H. Baharvand, S. Kiani, S. S. Al-Deyab, Application of conductive polymers, scaffolds and electrical stimulation for nerve tissue engineering, J. Tissue Eng. Regen. Med. 4 (2011) e17–e35. doi:10.1002/term.

[15]   C. Cha, S.R. Shin, N. Annabi, M.R. Dokmeci, A. Khademhosseini, Carbon-based nanomaterials: Multifunctional materials for biomedical engineering, ACS Nano. 7 (2013) 2891–2897. doi:10.1021/nn401196a.

[16]   X. Chen, Y. Wu, V.D. Ranjan, Y. Zhang, X. Chen, Y. Wu, V.D. Ranjan, Y. Zhang, Three-dimensional electrical conductive scaffold from biomaterial-based carbon microfiber sponge with bioinspired coating for cell proliferation and differentiation, Carbon N. Y. (2018). doi:10.1016/j.carbon.2018.03.064.

[17]   C. Lau, M.J. Cooney, P. Atanassov, Conductive macroporous composite chitosan-carbon nanotube scaffolds, Langmuir. 24 (2008) 7004–7010. doi:10.1021/la8005597.

[18]   J. Voldman, M.L. Gray, M. Toner, M.A. Schmidt, A microfabrication-based dynamic array cytometer, Anal. Chem. 74 (2002) 3984–3990. doi:10.1021/ac0256235.

[19]   J.N. Patel, B.L. Gray, B. Kaminska, B.D. Gates, Flexible three-dimensional electrochemical glucose sensor with improved sensitivity realized in hybrid polymer microelectromechanical systems technique, J. Diabetes Sci. Technol. 5 (2011) 1036–1043. doi:10.1177/193229681100500503.

[20]   J. Wang, B. Tian, V.B. Nascimento, L. Angnes, Performance of screen-printed carbon electrodes fabricated from different carbon inks, Electrochim. Acta. 43 (1998) 3459–3465. doi:10.1016/S0013-4686(98)00092-9.

[21]   S. Kim, J.H. Park, K. Kang, C.O. Park, I. Park, Direct metal micropatterning on needle-type structures towards bioimpedance and chemical sensing applications, J. Micromechanics Microengineering. 25 (2015). doi:10.1088/0960-1317/25/1/015002.

[22]   R.L. McCreery, Advanced carbon electrode materials for molecular electrochemistry, Chem. Rev. 108 (2008) 2646–2687. doi:10.1021/cr068076m.

[23]   R.P. Baldwin, Electrochemical determination of carbohydrates: enzyme electrodes and amperometric detection in liquid chromatography and capillary electrophoresis., J. Pharm. Biomed. Anal. 19 (1999) 69–81. http://www.ncbi.nlm.nih.gov/pubmed/10698569.

[24]   Q. Cheng, J. Tang, J. Ma, H. Zhang, N. Shinya, L.-C. Qin, Graphene and carbon nanotube composite electrodes for supercapacitors with ultra-high energy density, Phys. Chem. Chem. Phys. 13 (2011) 17615. doi:10.1039/c1cp21910c.

[25]   I. Heller, J. Kong, H.A. Heering, K.A. Williams, S.G. Lemay, C. Dekker, Individual single-walled carbon nanotubes as nanoelectrodes for electrochemistry, Nano Lett. 5 (2005) 137–142. doi:10.1021/nl048200m.

[26]   G.M. Swain, R. Ramesham, The Electrochemical Activity of Boron-Doped polycrystalline Diamond Thin Film Electrodes, Anal. Chem. 65 (1993) 345–351. doi:10.1021/ac00052a007.

[27]   A. Khosla, B.L. Gray, Preparation, characterization and micromolding of multi-walled carbon nanotube polydimethylsiloxane conducting nanocomposite polymer, Mater. Lett. 63 (2009) 1203–1206. doi:10.1016/j.matlet.2009.02.043.

[28]   D. Janasek, J. Franzke, A. Manz, Scaling and the design of miniaturized chemical-analysis systems, Nature. 442 (2006) 374–380. doi:10.1038/nature05059.

[29]   D.R. Reyes, D. Iossifidis, P.A. Auroux, A. Manz, Micro total analysis systems. 1. Introduction, theory, and technology, Anal. Chem. 74 (2002) 2623–2636. doi:10.1021/ac0202435.

[30]   J. Kim, X. Song, K. Kinoshita, M. Madou, B. White, Electrochemical studies of carbon films from pyrolyzed photoresist, J. Electrochem. Soc. 145 (1998) 2314–2319. doi:Doi 10.1149/1.1838636.

[31]   S. Ranganathan, R. McCreery, S.M. Majji, M. Madou, Photoresist-derived carbon for microelectromechanical systems and electrochemical applications, J. Electrochem. Soc. 147 (2000) 277. doi:10.1149/1.1393188.

[32]   C. Wang, G. Jia, L.H. Taherabadi, M.J. Madou, A novel method for the fabrication of high-aspect ratio C-MEMS structures, J. Microelectromechanical Syst. 14 (2005) 348–358. doi:10.1109/JMEMS.2004.839312.

[33]   F.C. Cowlard, J.C. Lewis, Vitreous carbon - A new form of carbon, J. Mater. Sci. 2 (1967) 507–512. doi:10.1007/BF00752216.

[34]   G.T. Teixidor, R. a Gorkin, P.P. Tripathi, G.S. Bisht, M. Kulkarni, T.K. Maiti, T.K. Battacharyya, J.R. Subramaniam, A. Sharma, B.Y. Park, M. Madou, Carbon microelectromechanical systems as a substratum for cell growth., Biomed. Mater. 3 (2008) 34116. doi:10.1088/1748-6041/3/3/034116.

[35]   G.T. Teixidor, C. Wang, M. Madou, Fabrication of 3D carbon microelectrodes for Li-Ion battery applications, Nanoscale Fabr. 3 (2006) 221–224.

[36]   C. Wang, L. Taherabadi, G. Jia, M. Madou, Y. Yeh, B. Dunn, C-MEMS for the manufacture of 3D microbatteries, Electrochem. Solid-State Lett. 7 (2004) A435. doi:10.1149/1.1798151.

[37]   H. Xu, K. Malladi, C. Wang, L. Kulinsky, M. Song, M. Madou, Carbon post-microarrays for glucose sensors, Biosens. Bioelectron. 23 (2008) 1637–1644. doi:10.1016/j.bios.2008.01.031.

[38]   J.A. Lee, S. Hwang, J. Kwak, S. Il Park, S.S. Lee, K.C. Lee, An electrochemical impedance biosensor with aptamer-modified pyrolyzed carbon electrode for label-free protein detection, Sensors Actuators, B Chem. 129 (2008) 372–379. doi:10.1016/j.snb.2007.08.034.

[39]   J.A. Lee, S.S. Lee, K.C. Lee, S. Il Park, B.C. Woo, J.O. Lee, Biosensor utilizing resist-derived carbon nanostructures, Appl. Phys. Lett. 90 (2007). doi:10.1063/1.2752719.

[40]   L. Amato, A. Heiskanen, C. Caviglia, F. Shah, K. Zór, M. Skolimowski, M. Madou, L. Gammelgaard, R. Hansen, E.G. Seiz, M. Ramos, T.R. Moreno, A. Martínez-Serrano, S.S. Keller, J. Emnéus, Pyrolysed 3D-carbon scaffolds induce spontaneous differentiation of human neural stem cells and facilitate real-time dopamine detection, Adv. Funct. Mater. 24 (2014) 7042–7052. doi:10.1002/adfm.201400812.

[41]   A. Mardegan, R. Kamath, S. Sharma, P. Scopece, P. Ugo, M. Madou, Optimization of Carbon Electrodes Derived from Epoxy-based Photoresist, J. Electrochem. Soc. 160 (2013) B132–B137. doi:10.1149/2.107308jes.

[42]   A. Hirsch, The era of carbon allotropes., Nat. Mater. 9 (2010) 868. doi:10.1038/nmat2885.

[43]   A.G. Whittaker, Carbon : A new view of its high-temperature behavior, Science (80-.). 200 (1978) 763–764.

[44]   S. Chakraborty, Microfluidics and microfabrication, 2010. doi:10.1007/978-1-4419-1543-6.

[45]   W. Zhang, S. Zhu, R. Luque, S. Han, L. Hu, G. Xu, Recent development of carbon electrode materials and their bioanalytical and environmental applications, Chem. Soc. Rev. 45 (2016) 715–752. doi:10.1039/C5CS00297D.

[46]   J. Xu, M.C. Granger, Q. Chen, J.W. Strojek, T.E. Lister, G.M. Swain, Boron-Doped Diamond Thin-Film Electrodes, Anal. Chem. 69 (1997) 591A–597A. doi:10.1021/ac971791z.

[47]   F. Tuinstra, J.L. Koenig, Raman Spectrum of Graphite, J. Chem. Phys. 53 (1970) 1126–1130. doi:10.1063/1.1674108.

[48]   P.J. Britto, K.S.V. Santhanam, P.M. Ajayan, Carbon nanotube electrode for oxidation of dopamine, Bioelectrochemistry Bioenerg. 41 (1996) 121–125. doi:10.1016/0302-4598(96)05078-7.

[49]   C. Niu, E.K. Sichel, R. Hoch, D. Moy, H. Tennent, C. Niu, E.K. Sichel, R. Hoch, D. Moy, H. Tennent, High power electrochemical capacitors based on carbon nanotube electrodes, Appl. Phys. Lett. 1480 (2016) 9–12. doi:10.1063/1.118568.

[50]   Z. Ren, Y. Lan, Y. Wang, Aligned Carbon Nanotubes: Physics, concepts, fabrication and devices, Nanosci. Technol. 5 (2013) 1–6. doi:10.1007/978-3-642-30490-3.

[51]   P.J.F. Harris, Fullerene-related structure of commercial glassy carbons, Philos. Mag. 84 (2004) 3159–3167. doi:10.1080/14786430410001720363.

[52]   G.M. Jenkins, K. Kawamura, L.L. Ban, Formation and Structure of Polymeric Carbons, Proc. R. Soc. A Math. Phys. Eng. Sci. 327 (1972) 501–517. doi:10.1098/rspa.1972.0060.

[53]   B.Y. Park, L. Taherabadi, C. Wang, J. Zoval, M.J. Madou, Electrical Properties and Shrinkage of Carbonized Photoresist Films and the Implications for Carbon Microelectromechanical Systems Devices in Conductive Media, J. Electrochem. Soc. 152 (2005) J136. doi:10.1149/1.2116707.

[54]   W.E. Van der Linden, J.W. Dieker, Glassy carbon as electrode material in electro- analytical chemistry, Anal. Chim. Acta. 119 (1980) 1–24. doi:10.1016/S0003-2670(00)00025-8.

[55]   A. Dekanski, J. Stevanović, R. Stevanović, B.Ž. Nikolić, V.M. Jovanović, Glassy carbon electrodes, Carbon N. Y. 39 (2001) 1195–1205. doi:10.1016/S0008-6223(00)00228-1.

[56]   D.A.C. Brownson, C.W. Foster, C.E. Banks, The electrochemical performance of graphene modified electrodes: an analytical perspective., Analyst. 137 (2012) 1815–23. doi:10.1039/c2an16279b.

[57]   Y. Zheng, Y. Jiao, Y. Zhu, L.H. Li, Y. Han, Y. Chen, A. Du, M. Jaroniec, S.Z. Qiao, Hydrogen evolution by a metal-free electrocatalyst, Nat. Commun. 5 (2014) 1–8. doi:10.1038/ncomms4783.

[58]   J. Liang, Y. Zheng, J. Chen, J. Liu, D. Hulicova-Jurcakova, M. Jaroniec, S.Z. Qiao, Facile oxygen reduction on a three-dimensionally ordered macroporous graphitic C3N4/carbon composite electrocatalyst, Angew. Chemie - Int. Ed. 51 (2012) 3892–3896. doi:10.1002/anie.201107981.

[59]   F. Bonaccorso, L. Colombo, G. Yu, M. Stoller, V. Tozzini, A.C. Ferrari, R.S. Ruoff, V. Pellegrini, Graphene, related two-dimensional crystals, and hybrid systems for energy conversion and storage, Science (80-.). 347 (2015) 12465011–12465019. doi:10.1126/science.1246501.

[60]   L.L. Zhang, R. Zhou, X.S. Zhao, Carbon-based materials as supercapacitor electrodes, J. Mater. Chem. 38 (2009) 2520–2531. doi:10.1039/c000417k.

[61]   C.C.M. Ma, C.Y. Chen, H.C. Kuan, W.C. Chang, Processability, thermal, mechanical, and morphological properties of novolac type-epoxy resin-based carbon-carbon composite, J. Compos. Mater. 38 (2004) 311–320. doi:10.1177/0021998304039267.

[62]   K.S. Chen, R.Z. Yeh, Pyrolysis kinetics of epoxy resin in a nitrogen atmosphere, J. Hazard. Mater. 49 (1996) 105–113. doi:10.1016/0304-3894(96)01779-7.

[63]   A. Singh, J. Jayaram, M. Madou, S. Akbar, Pyrolysis of negative photoresists to fabricate carbon structures for microelectromechanical systems and electrochemical applications, J. Electrochem. Soc. 149 (2002) 78–83. doi:10.1149/1.1436085.

[64]   O.J.A. Schueller, S.T. Brittain, C. Marzolin, G.M. Whitesides, Fabrication and characterization of glassy carbon MEMS, Chem. Mater. 9 (1997) 1399–1406. doi:10.1021/cm960639v.

[65]   S. Ranganathan, R.L. McCreery, Electroanalytical performance of carbon films with near-atomic flatness, Anal. Chem. 73 (2001) 893–900. doi:10.1021/ac0007534.

[66]   L. Amato, A. Heiskanen, R. Hansen, L. Gammelgaard, T. Rindzevicius, M. Tenje, J. Emnéus, S.S. Keller, Dense high-aspect ratio 3D carbon pillars on interdigitated microelectrode arrays, Carbon N. Y. 94 (2015) 792–803. doi:10.1016/j.carbon.2015.06.014.

[67]   S. Hemanth, C. Caviglia, S.S. Keller, Suspended 3D pyrolytic carbon microelectrodes for electrochemistry, Carbon N. Y. 121 (2017) 226–234. doi:10.1016/j.carbon.2017.05.090.

[68]   R. Martinez-Duarte, P. Renaud, M.J. Madou, A novel approach to dielectrophoresis using carbon electrodes, Electrophoresis. 32 (2011) 2385–2392. doi:10.1002/elps.201100059.

[69]   B.Y. Park, M.J. Madou, Design, fabrication, and initial testing of a miniature PEM fuel cell with micro-scale pyrolyzed carbon fluidic plates, J. Power Sources. 162 (2006) 369–379. doi:10.1016/j.jpowsour.2006.06.077.

[70]   P.C. Lin, B.Y. Park, M.J. Madou, Development and characterization of a miniature PEM fuel cell stack with carbon bipolar plates, J. Power Sources. 176 (2008) 207–214. doi:10.1016/j.jpowsour.2007.10.079.

[71]   S. Kassegne, B. Wondimu, M. Majzoub, J. Shin, High-efficiency microarray of 3D carbon MEMS electrodes for pathogen detection systems, Proc. SPIE. 7266 (2008) 726615, 1–6. doi:10.1117/12.806624.

[72]   O.J.A. Schueller, S.T. Brittain, G.M. Whitesides, Fabrication of glassy carbon microstructures by pyrolysis of microfabricated polymeric precursors, Adv. Mater. 9 (1997) 477–480. doi:10.1002/adma.19970090604.

[73]   M. Hirabayashi, B. Mehta, N.W. Vahidi, A. Khosla, S. Kassegne, Functionalization and characterization of pyrolyzed polymer based carbon microstructures for bionanoelectronics platforms, J. Micromechanics Microengineering. 23 (2013). doi:10.1088/0960-1317/23/11/115001.

[74]   G.M. Jenkins, K. Kawamura, Polymeric carbons--carbon fibre, glass and char, Cambridge University Press, 1976.

[75]   E. Fitzer, W. Schaefer, S. Yamada, The formation of glasslike carbon by pyrolysis of polyfurfuryl alcohol and phenolic resin, Carbon N. Y. 7 (1969) 643–648. doi:10.1016/0008-6223(69)90518-1.

[76]   K. Nishikawa, K. Fukuyama, T. Nishizawa, Structure change of glass-like carbon with heat treatment, studied by small angle X-ray scattering: I. Glass-like carbon prepared from phenolic resin, Japanese J. Appl. Physics, Part 1 Regul. Pap. Short Notes Rev. Pap. 37 (1998) 6486–6491. doi:10.1143/JJAP.37.6486.

[77]   K. Kawamura, S. Kimura, Glass-Like Carbon Made From Epoxy Resin Cured With 2,4,6-Trinitrophenol., Bull. Chem. Soc. Jpn. 56 (1983) 2499–2503. doi:10.1246/bcsj.56.2499.

[78]   S.Y. Cho, Y.S. Yun, S. Lee, D. Jang, K.-Y. Park, J.K. Kim, B.H. Kim, K. Kang, D.L. Kaplan, H.-J. Jin, Carbonization of a stable β-sheet-rich silk protein into a pseudographitic pyroprotein, Nat. Commun. 6 (2015) 7145. doi:10.1038/ncomms8145.

[79]   L. Amato, L. Schulte, A. Heiskanen, S.S. Keller, S. Ndoni, J. Emnéus, Novel Nanostructured Electrodes Obtained by Pyrolysis of Composite Polymeric Materials, Electroanalysis. 27 (2015) 1544–1549. doi:10.1002/elan.201400430.

[80]   S. Sharma, R. Kamath, M. Madou, Porous glassy carbon formed by rapid pyrolysis of phenol-formaldehyde resins and its performance as electrode material for electrochemical double layer capacitors, J. Anal. Appl. Pyrolysis. 108 (2014) 12–18. doi:10.1016/j.jaap.2014.05.025.

[81]   R.A. Fisher, The Design of Experiments., Am. Math. Mon. 43 (1936) 180. doi:10.2307/2300364.

[82]   D.C. Montgomery, Design and Analysis of Experiments, Eight edit, John Wiley & Sons, Inc., 2013.

[83]   L. Wasserman, All of Statistics. A concise course in statistical inference, Springer Science & Business Media, 2013.

[84]   D. Montgomery, Introduction to statistical quality control, 2009. http://scholar.google.com/scholar?hl=en&btnG=Search&q=intitle:Introduction+to+Statistical+Quality+Control#0.

[85]   S. Hemanth, Fabrication of three-dimensional carbon microelectrodes for electrochemical sensing Fabrication of three-dimensional carbon microelectrodes for electrochemical sensing, 2017.

[86]   S. Camelia, Pyrolytic carbon electrodes : a new geometry, Master thesis, 2017.

[87]   L.F. Thompson, An introduction to lithography, ACS Symp. Ser. Am. Chem. Soc. (1983).

[88]   A. Del Campo, C. Greiner, SU-8: A photoresist for high-aspect-ratio and 3D submicron lithography, J. Micromechanics Microengineering. 17 (2007). doi:10.1088/0960-1317/17/6/R01.

[89]   Momentive Specialty Chemicals Inc, EPON ™ and EPI-REZ ™ Epoxy Resins, 2013.

[90]   R. Martinez-Duarte, SU-8 Photolithography as a Toolbox for Carbon MEMS, Micromachines. 5 (2014) 766–782. doi:10.3390/mi5030766.

[91]   A. Vu, Y. Qian, A. Stein, Porous electrode materials for lithium-ion batteries-how to prepare them and what makes them special, Adv. Energy Mater. 2 (2012) 1056–1085. doi:10.1002/aenm.201200320.

[92]   A. Feinle, M.S. Elsaesser, N. Hüsing, Sol–gel synthesis of monolithic materials with hierarchical porosity, Chem. Soc. Rev. 45 (2016) 3377–3399. doi:10.1039/C5CS00710K.

[93]   A.D. Roberts, X. Li, H. Zhang, Porous carbon spheres and monoliths: morphology control, pore size tuning and their applications as Li-ion battery anode materials, Chem. Soc. Rev. 43 (2014) 4341–4356. doi:10.1039/C4CS00071D.

[94]   X.-Y. Yang, L.-H. Chen, Y. Li, J.C. Rooke, C. Sanchez, B.-L. Su, Hierarchically porous materials: synthesis strategies and structure design, Chem. Soc. Rev. 46 (2017) 481–558. doi:10.1039/C6CS00829A.

[95]   A.H. Lu, F. Schüth, Nanocasting: A versatile strategy for creating nanostructured porous

materials, Adv. Mater. 18 (2006) 1793–1805. doi:10.1002/adma.200600148.

[96]   D.B. Burckel, C.M. Washburn, A.K. Raub, S.R.J. Brueck, D.R. Wheeler, S.M. Brozik, R. Polsky, Lithographically defined porous carbon electrodes, Small. 5 (2009) 2792–2796. doi:10.1002/smll.200901084.

[97]   B. Gates, Y. Yin, Y. Xia, Fabrication and characterization of porous membranes with highly ordered three-dimensional periodic structures, Chem. Mater. 11 (1999) 2827–2836. doi:10.1021/cm990195d.

[98]   C. Shen, X. Wang, W. Zhang, F. Kang, Direct prototyping of patterned nanoporous carbon: A route from materials to on-chip devices, Sci. Rep. 3 (2013) 1–6. doi:10.1038/srep02294.

[99]   G. Inzelt, A. Lewenstam, F. Scholz, Handbook of Reference Electrodes, Springer, 2013.

[100]   Sigma-Aldrich, Micro particles based on polystyrene, 2018.

[101]   J.L. Gurman, L. Baier, B.C. Levin, Polystyrene- A Review of the Literature and on the products of Thermal Decomposition and Toxicity, Fire Mater. 11 (1987) 109–130.

[102]   K. Nojiri, Dry etching technology for semiconductors, Dry Etch. Technol. Semicond. (2015) 1–116. doi:10.1007/978-3-319-10295-5.

[103]   M.F.L. De Volder, R. Vansweevelt, P. Wagner, D. Reynaerts, C. Van Hoof, A.J. Hart, Hierarchical carbon nanowire microarchitectures made by plasma-assisted pyrolysis of photoresist, ACS Nano. 5 (2011) 6593–6600. doi:10.1021/nn201976d.

[104]   K.H. Rasmussen, S.S. Keller, F. Jensen, A.M. Jorgensen, O. Hansen, SU-8 etching in inductively coupled oxygen plasma, Microelectron. Eng. 112 (2013) 35–40. doi:10.1016/j.mee.2013.05.011.

[105]   F.A. Denis, P. Hanarp, D.S. Sutherland, Y.F. Dufrêne, Fabrication of Nanostructured Polymer Surfaces Using Colloidal Lithography and Spin-Coating, Nano Lett. 2 (2002) 1419–1425. doi:10.1021/nl025750g.

[106]   J.K. Chen, J.Q. Qui, S.K. Fan, S.W. Kuo, F.H. Ko, C.W. Chu, F.C. Chang, Using colloid lithography to fabricate silicon nanopillar arrays on silicon substrates, J. Colloid Interface Sci. 367 (2012) 40–48. doi:10.1016/j.jcis.2011.10.044.

[107]   A. Valsesia, T. Meziani, F. Bretagnol, P. Colpo, G. Ceccone, F. Rossi, Plasma assisted production of chemical nano-patterns by nano-sphere lithography: Application to bio-interfaces, J. Phys. D. Appl. Phys. 40 (2007) 2341–2347. doi:10.1088/0022-3727/40/8/S13.

[108]   L. Amato, Pyrolysed carbon scaffolds for bioelectrochemistry in life science, Ph.D thesis, 2013.

[109]   R. Brennan, D. Dickey, Determination of diffusion characteristics using two-and four-point probe measurements, Tech. Note Solecon Labs. (1984) 1–10. doi:10.1016/j.chroma.2010.04.043.

[110]   D.M.A. Mackenzie, J.D. Buron, P.R. Whelan, B.S. Jessen, A. Silajdźić, A. Pesquera, A. Centeno, A. Zurutuza, P. Bøggild, D.H. Petersen, Fabrication of CVD graphene-based devices via laser ablation for wafer-scale characterization, 2D Mater. 2 (2015) 45003. doi:10.1088/2053-1583/2/4/045003.

[111]   L.J. van der Pauw, A method of measuring the resistivity and Hall coefficient on lamellae of arbitrary shape, Philips Tech. Rev. 20 (1958) 220–224. doi:537.723.1:53.081.7+538.632:083.9.

[112] A.A. Ramadan, R.D. Gould, A. Ashour, On the Van der Pauw method of resistivity measurements, Thin Solid Films. 239 (1994) 272–275. doi:10.1016/0040-6090(94)90863-X.

[113] Y.M. Hassan, C. Caviglia, S. Hemanth, D.M.A. Mackenzie, T.S. Alstrøm, D.H. Petersen, S.S. Keller, High temperature SU-8 pyrolysis for fabrication of carbon electrodes, J. Anal. Appl. Pyrolysis. 125 (2017) 91–99. doi:10.1016/j.jaap.2017.04.015.

[114] C. V. Raman, K.S. Krishnan, A New Type of Secondary Radiation, Nature. 121 (1928) 501–502. doi:10.1038/121501c0.

[115] E. V. Efremov, F. Ariese, C. Gooijer, Achievements in resonance Raman spectroscopy. Review of a technique with a distinct analytical chemistry potential, Anal. Chim. Acta. 606 (2008) 119–134. doi:10.1016/j.aca.2007.11.006.

[116] P.K. Chu, L. Li, Characterization of amorphous and nanocrystalline carbon films, Mater. Chem. Phys. 96 (2006) 253–277. doi:10.1016/j.matchemphys.2005.07.048.

[117] F. Tuinstra, L. Koenig, Raman Spectrum of Graphite, J. Chem. Phys. 53 (1970) 1126–1130. doi:10.1063/1.1674108.

[118] A. Ferrari, J. Robertson, Interpretation of Raman spectra of disordered and amorphous carbon, Phys. Rev. B. 61 (2000) 14095–14107. doi:10.1103/PhysRevB.61.14095.

[119] Y.M. Hassan, C. Caviglia, S. Hemanth, D.M.A. Mackenzie, T.S. Alstrøm, D.H. Petersen, S.S. Keller, High temperature SU-8 pyrolysis for fabrication of carbon electrodes, J. Anal. Appl. Pyrolysis. (2017). doi:10.1016/j.jaap.2017.04.015.

[120] R. Kostecki, B. Schnyder, D. Alliata, X. Song, K. Kinoshita, R. Kötz, Surface studies of carbon films from pyrolyzed photoresist, Thin Solid Films. 396 (2001) 36–43. doi:10.1016/S0040-6090(01)01185-3.

[121] P.J. Goodhew, J. Humphreys, R. Beanland, Electron microscopy and analysis, Taylor & Francis, 2000. doi:10.1037/0022-006X.76.3.524.

[122] P.J. Breton, From Microns to Nanometers: Early Landmarks in the Science of Scanning Electron Microscope Imaging, Scanning Microsc. 13 (1999) 1–6.

[123] A.J. Bard, L.R. Faulkner, Electrochemical methods : fundamentals and applications, Wiley, 2001.

[124] R. Liu, J. Duay, S.B. Lee, Heterogeneous nanostructured electrode materials for electrochemical energy storage, Chem. Commun. 47 (2011) 1384–1404. doi:10.1039/C0CC03158E.

[125] S. Tanimoto, A. Ichimura, Discrimination of inner- and outer-sphere electrode reactions by cyclic voltammetry experiments, J. Chem. Educ. 90 (2013) 778–781. doi:10.1021/ed200604m.

[126] S. Hemanth, C. Caviglia, L. Amato, T.A. Anhoj, A. Heiskanen, J. Emneus, S.S. Keller, Pyrolytic 3D Carbon Microelectrodes for Electrochemistry, ECS Trans. 72 (2016) 117–124. doi:10.1149/07201.0117ecst.

[127] R.L. McCreery, K.K. Cline, C.A. McDermott, M.T. McDermott, Control of reactivity at carbon electrode surfaces, Colloids Surfaces A Physicochem. Eng. Asp. 93 (1994) 211–219. doi:10.1016/0927-7757(94)02899-0.

[128] K.K. Cline, M.T. McDermott, R.L. McCreery, Anomalously slow electron transfer at ordered graphite electrodes: Influence of electronic factors and reactive sites, J. Phys. Chem. 98 (1994)

5314–5319. doi:10.1021/j100071a023.

[129] P. Chen, R.L. McCreery, Control of Electron Transfer Kinetics at Glassy Carbon Electrodes by Specific Surface Modification, Anal. Chem. 68 (1996) 3958–3965. doi:10.1021/ac960492r.

[130] I. Hu, D.H. Karweik, T. Kuwana, Activation and deactivation of glassy carbon electrodes, J. Electroanal. Chem. 188 (1985) 59–72. doi:10.1016/S0022-0728(85)80050-4.

[131] F. Scholz, Electroanalytical Methods, Springer, doi:10.1007/978-3-642-02915-8.

[132] https://www.comsol.com/blogs/electrochemical-impedance-spectroscopy-experiment-model-and-app/.

[133] V.F. Lvovich, Impedance Spectroscopy, John Wiley & Sons, Inc., Hoboken, NJ, USA, 2012. doi:10.1002/9781118164075.

[134] C. Caviglia, Analysis Platform : Towards New Tools for Biomedical Research, Ph.D thesis, 2014.

[135] E. Barsoukov, Impedance Spectroscopy, John Wiley & Sons, Inc., Hoboken, NJ, USA, 2005. doi:10.1002/0471716243.

[136] D.A.C. Brownson, C.E. Banks, The Handbook of Graphene Electrochemistry, 2014. doi:10.1007/978-1-4471-6428-9.

[137] H. Rettig, U. Weber, H. Brückmann, U. Rosenblatt, K.J. Hüttinger, Carbon as an implant material in orthopaedic surgery, Arch. Orthop. Trauma. Surg. 94 (1979) 241–244. doi:10.1007/BF00383407.

[138] S.L. Goodman, K.S. Tweden, R.M. Albrecht, Platelet interaction with pyrolytic carbon heart-valve leaflets, J. Biomed. Mater. Res. 32 (1996) 249–258. doi:10.1002/(SICI)1097-4636(199610)32:2<249::AID-JBM15>3.0.CO;2-E.

[139] J. Lee, C.T. Bubar, A. Busnaina, S.J. Shefelbine, H. Lee, Standardization of a bone formation biomarker quantification using screen printed electrodes, Appl. Spectrosc. Rev. 51 (2016) 753–761. doi:10.1080/05704928.2016.1168828.

[140] B. Clarke, Normal bone anatomy and physiology., Clin. J. Am. Soc. Nephrol. 3 Suppl 3 (2008) 131–139. doi:10.2215/CJN.04151206.

[141] U.K. Nandeesh, B.N. Nandeesh, Physiology of Bone Formation, Remodeling and Metabolism, in: Springer (Ed.), Radionucl. Hybrid Bone Imaging, 2012: pp. 29–55.

[142] E.M. Czekanska, M.J. Stoddart, R.G. Richards, J.S. Hayes, In search of an osteoblast cell model for in vitro research, Eur. Cells Mater. 24 (2012) 1–17. doi:10.22203/eCM.v024a01.

[143] T.M. Keaveny, E.F. Morgan, O.C. Yeh, Bone Mechanics, Stand. Handb. Biomed. Eng. Des. (2004) 8.1-8.23. doi:10.1385/1-59259-366-6:369.

[144] Bone anatomy, http://www.alilamedicalimages.org/.

[145] E.N. Marieb, Essentials of Human Anatomy & physiology, 2009.

[146] R. Florencio-Silva, G. Rodrigues, S. Sasso, E. Sasso-Cerri, M. Simões, P.S. Cerri, Biology of Bone Tissue: structure, function, and factors that influence bone cells, Biomed Res. Int. 2015 (2015) 1–17. doi:10.1155/2015/421746.

[147] A. Rutkovskiy, K.-O. Stensløkken, I.J. Vaage, Osteoblast Differentiation at a Glance, Med. Sci. Monit. Basic Res. 22 (2016) 95–106. doi:10.12659/MSMBR.901142.

[148] T. Heino, T. Hentunen, Differentiation of Osteoblasts and Osteocytes from Mesenchymal Stem Cells, Curr. Stem Cell Res. Ther. 3 (2008) 131–145. doi:10.2174/157488808784223032.

[149] Cortical bone and cancellous bone, Http://boneandspine.com/cortical-bone-and-cancellous-bone/.

[150] PromoCell, Osteoblast Differentiation and Osteoblast Differentiation and Mineralization, PromoCell. 5.

[151] C. Liu, Y. Cui, J. Luan, X. Zhou, Z. Liu, J. Han, Fibroblast growth factor-2 inhibits mineralization of osteoblast-like Saos-2 cells by inhibiting the functioning of matrix vesicles, Drug Discov. Ther. 8 (2014) 42–47. doi:10.5582/ddt.8.42.

[152] T.D. Rachner, S. Khosla, L.C. Hofbauer, Osteoporosis: Now and the future, Lancet. 377 (2011) 1276–1287. doi:10.1016/S0140-6736(10)62349-5.

[153] J.R.R. Stotf, The mechanical properties of bone in osteoporosis, Society. 63 (2006) 233–238. http://web.jbjs.org.uk/content/63-B/2/233.full.pdf.

[154] US Department of Health and Human Services, Bone health and osteoporosis: a report of the Surgeon General, US Heal. Hum. Serv. (2004) 437. doi:10.2165/00002018-200932030-00004.

[155] L. Gennari, S. Rotatori, S. Bianciardi, S. Gonnelli, R. Nuti, D. Merlotti, Appropriate models for novel osteoporosis drug discovery and future perspectives, Expert Opin. Drug Discov. 10 (2015) 1201–1216. doi:10.1517/17460441.2015.1080685.

[156] S.R. Cummings, L.J. Melton, Osteoporosis I: Epidemiology and outcomes of osteoporotic fractures, Lancet. 359 (2002) 1761–1767. doi:10.1016/S0140-6736(02)08657-9.

[157] D.J. Becker, M.L. Kilgore, M.A. Morrisey, The societal burden of osteoporosis, Curr. Rheumatol. Rep. 12 (2010) 186–191. doi:10.1007/s11926-010-0097-y.

[158] C.G. Begley, L.M. Ellis, Drug development: Raise standards for preclinical cancer research, Nature. 483 (2012) 531–533. doi:10.1038/483531a.

[159] D.D. Allen, R. Caviedes, A.M. Cárdenas, T. Shimahara, J. Segura-Aguilar, P.A. Caviedes, Cell lines as in vitro models for drug screening and toxicity studies, Drug Dev. Ind. Pharm. 31 (2005) 757–768. doi:10.1080/03639040500216246.

[160] A. Astashkina, B. Mann, D.W. Grainger, A critical evaluation of in vitro cell culture models for high-throughput drug screening and toxicity, Pharmacol. Ther. 134 (2012) 82–106. doi:10.1016/j.pharmthera.2012.01.001.

[161] The Drug Development Process, https://www.fda.gov/ForPatients/Approvals/Drugs/default.htm.

[162] S. Kummar, R. Kinders, L. Rubinstein, R.E. Parchment, A.J. Murgo, J. Collins, O. Pickeral, J. Low, S.M. Steinberg, M. Gutierrez, S. Yang, L. Helman, R. Wiltrout, J.E. Tomaszewski, J.H. Doroshow, Compressing drug development timelines in oncology using phase "0" trials, Nat. Rev. Cancer. 7 (2007) 131–139. doi:10.1038/nrc2066.

[163] A.L. Niles, R.A. Moravec, T.L. Riss, Update on *in vitro* cytotoxicity assays for drug development, Expert Opin. Drug Discov. 3 (2008) 655–669. doi:10.1517/17460441.3.6.655.

[164] T. Riss, R. Moravecs, A. Niles, S. Duellman, H. Benink, T. Worzella, L. Minor, Cell viability assays, Assay Guid. Man. (2016) 1–31. doi:10.1016/j.acthis.2012.01.006.

[165] K.A. Marx, Quartz crystal microbalance: A useful tool for studying thin polymer films and complex biomolecular systems at the solution - Surface interface, Biomacromolecules. 4 (2003) 1099–1120. doi:10.1021/bm020116i.

[166] T.S. Hug, J.E. Prenosil, M. Morbidelli, Optical waveguide lightmode spectroscopy as a new method to study adhesion of anchorage-dependent cells as an indicator of metabolic state, Biosens. Bioelectron. 16 (2001) 865–874. doi:10.1016/S0956-5663(01)00204-4.

[167] J. Yoon, K. Kim, H. Park, C. Choi, S. Jang, Y. Park, Label-free characterization of white blood cells by measuring 3D refractive index maps, Biomed. Opt. Express. 6 (2015) 3865. doi:10.1364/BOE.6.003865.

[168] L. Ceriotti, J. Ponti, P. Colpo, E. Sabbioni, F. Rossi, Assessment of cytotoxicity by impedance spectroscopy, Biosens. Bioelectron. 22 (2007) 3057–3063. doi:10.1016/j.bios.2007.01.004.

[169] C. Xiao, J.H.T. Luong, Assessment of cytotoxicity by emerging impedance spectroscopy, Toxicol. Appl. Pharmacol. 206 (2005) 102–112. doi:10.1016/j.taap.2004.10.025.

[170] S. Arndt, J. Seebach, K. Psathaki, H.J. Galla, J. Wegener, Bioelectrical impedance assay to monitor changes in cell shape during apoptosis, Biosens. Bioelectron. 19 (2004) 583–594. doi:10.1016/S0956-5663(03)00269-0.

[171] R. Pethig, I. Schmueser, Marking 100 years since Rudolf Höber's discovery of the insulating envelope surrounding cells and of the beta-dispersion exhibited by tissue, J. Electr. Bioimpedance. 3 (2012) 74–79. doi:10.5617/jeb.401.

[172] H.P. Schwan, Electrical Properties of Tissue and Cell Suspensions, ACADEMIC PRESS INC., 1957. doi:10.1016/B978-1-4832-3111-2.50008-0.

[173] I. Giaever, C.R. Keese, Monitoring fibroblast behavior in tissue culture with an applied electric field, Proc. Natl. Acad. Sci. U. S. A. 81 (1984) 3761–3764. doi:10.1073/pnas.81.12.3761.

[174] C.-M. Lo, C.R. Keese, I. Giaever, pH changes in pulsed CO2 incubators cause periodic changes in cell morphology., Exp. Cell Res. 213 (1994) 391–7. doi:10.1006/excr.1994.1214.

[175] I. Giaever, C.R. Keese, Micromotion of mammalian cells measured electrically., Proc. Natl. Acad. Sci. U. S. A. 88 (1991) 7896–7900. doi:10.1073/pnas.88.17.7896.

[176] P.O. Bagnaninchi, N. Drummond, Real-time label-free monitoring of adipose-derived stem cell differentiation with electric cell-substrate impedance sensing, Proc. Natl. Acad. Sci. 108 (2011) 6462–6467. doi:10.1073/pnas.1018260108.

[177] K. Solly, X. Wang, X. Xu, B. Strulovici, W. Zheng, Application of Real-Time Cell Electronic Sensing (RT-CES) Technology to Cell-Based Assays, Assay Drug Dev. Technol. 2 (2004) 363–372. doi:10.1089/adt.2004.2.363.

[178] H. Yin, F.L. Wang, A.L. Wang, J. Cheng, Y. Zhou, Bioelectrical impedance assay to monitor changes in aspirin-treated human colon cancer HT-29 cell shape during apoptosis, Anal. Lett. 40 (2007) 85–94. doi:10.1080/00032710600952424.

[179] C. Xiao, J.H.T. Luong, On-Line Monitoring of Cell Growth and Cytotoxicity Using Electric Cell - Substrate Impedance Sensing (ECIS), Biotechnol. Prog. (2003) 1000–1005.

doi:10.1021/bp025733x.

[180] Q. Liu, J. Yu, L. Xiao, J.C.O. Tang, Y. Zhang, P. Wang, M. Yang, Impedance studies of bio-behavior and chemosensitivity of cancer cells by micro-electrode arrays, Biosens. Bioelectron. 24 (2009) 1305–1310. doi:10.1016/j.bios.2008.07.044.

[181] W. Roa, X. Yang, L. Guo, B. Huang, S. Khatibisepehr, S. Gabos, J. Chen, J. Xing, Real-time cell-impedance sensing assay as an alternative to clonogenic assay in evaluating cancer radiotherapy, Anal. Bioanal. Chem. 400 (2011) 2003–2011. doi:10.1007/s00216-011-4934-2.

[182] J. Hong, K. Kandasamy, M. Marimuthu, C.S. Choi, S. Kim, Electrical cell-substrate impedance sensing as a non-invasive tool for cancer cell study, Analyst. 136 (2011) 237–245. doi:10.1039/C0AN00560F.

[183] S. Diemert, A.M. Dolga, S. Tobaben, J. Grohm, S. Pfeifer, E. Oexler, C. Culmsee, Impedance measurement for real time detection of neuronal cell death, J. Neurosci. Methods. 203 (2012) 69–77. doi:10.1016/j.jneumeth.2011.09.012.

[184] L.R. Arias, C.A. Perry, L. Yang, Real-time electrical impedance detection of cellular activities of oral cancer cells, Biosens. Bioelectron. 25 (2010) 2225–2231. doi:10.1016/j.bios.2010.02.029.

[185] P. Linderholm, T. Braschler, J. Vannod, Y. Barrandon, M. Brouard, P. Renaud, Two-dimensional impedance imaging of cell migration and epithelial stratification, Lab Chip. 6 (2006) 1155. doi:10.1039/b603856e.

[186] K. Zór, A. Heiskanen, C. Caviglia, M. Vergani, E. Landini, F. Shah, M. Carminati, A. Martínez-Serrano, T.R. Moreno, M. Kokaia, D. Benayahu, Z. Keresztes, D. Papkovsky, U. Wollenberger, W.E. Svendsen, M. Dimaki, G. Ferrari, R. Raiteri, M. Sampietro, M. Dufva, J. Emnéus, A compact multifunctional microfluidic platform for exploring cellular dynamics in real-time using electrochemical detection, RSC Adv. 4 (2014) 63761–63771. doi:10.1039/C4RA12632G.

[187] J. a. Stolwijk, K. Matrougui, C.W. Renken, M. Trebak, Impedance analysis of GPCR-mediated changes in endothelial barrier function: overview and fundamental considerations for stable and reproducible measurements, Pflugers Arch. Eur. J. Physiol. 467 (2014) 2193–2218. doi:10.1007/s00424-014-1674-0.

[188] J. Wegener, C.R. Keese, I. Giaever, Electric cell-substrate impedance sensing (ECIS) as a noninvasive means to monitor the kinetics of cell spreading to artificial surfaces, Exp. Cell Res. 259 (2000) 158–166. doi:10.1006/excr.2000.4919.

[189] M. Carminati, M. Vergani, G. Ferrari, L. Caranzi, M. Caironi, M. Sampietro, Accuracy and resolution limits in quartz and silicon substrates with microelectrodes for electrochemical biosensors, Sensors Actuators, B Chem. 174 (2012) 168–175. doi:10.1016/j.snb.2012.08.021.

[190] F. Asphahani, M. Zhang, Cellular impedance biosensors for drug screening and toxin detection, Analyst. 132 (2007) 835. doi:10.1039/b704513a.

[191] N. Joye, A. Schmid, Y. Leblebici, Electrical modeling of the cell-electrode interface for recording neural activity from high-density microelectrode arrays, Neurocomputing. 73 (2009) 250–259. doi:10.1016/j.neucom.2009.09.006.

[192] D. a Borkholder, Cell Based Biosensors using Microelectrodes, PhD Thesis. (1998) 1–253. doi:10.1017/CBO9781107415324.004.

[193] E. Sarró, M. Lecina, A. Fontova, C. Solà, F. Gòdia, J.J. Cairó, R. Bragós, Electrical impedance

spectroscopy measurements using a four-electrode configuration improve on-line monitoring of cell concentration in adherent animal cell cultures, Biosens. Bioelectron. 31 (2012) 257–263. doi:10.1016/j.bios.2011.10.028.

[194] Y.A. Abassi, B. Xi, W. Zhang, P. Ye, S.L. Kirstein, M.R. Gaylord, S.C. Feinstein, X. Wang, X. Xu, Kinetic Cell-Based Morphological Screening: Prediction of Mechanism of Compound Action and Off-Target Effects, Chem. Biol. 16 (2009) 712–723. doi:10.1016/j.chembiol.2009.05.011.

[195] E. Urcan, U. Haertel, M. Styllou, R. Hickel, H. Scherthan, F.X. Reichl, Real-time xCELLigence impedance analysis of the cytotoxicity of dental composite components on human gingival fibroblasts, Dent. Mater. 26 (2010) 51–58. doi:10.1016/j.dental.2009.08.007.

[196] L. Wang, H. Wang, L. Wang, K. Mitchelson, Z. Yu, J. Cheng, Analysis of the sensitivity and frequency characteristics of coplanar electrical cell-substrate impedance sensors, Biosens. Bioelectron. 24 (2008) 14–21. doi:10.1016/j.bios.2008.03.018.

[197] A.R. Abdur Rahman, D.T. Price, S. Bhansali, Effect of electrode geometry on the impedance evaluation of tissue and cell culture, Sensors Actuators, B Chem. 127 (2007) 89–96. doi:10.1016/j.snb.2007.07.038.

[198] R. Pradhan, M. Mandal, A. Mitra, S. Das, Monitoring cellular activities of cancer cells using impedance sensing devices, Sensors Actuators, B Chem. 193 (2014) 478–483. doi:10.1016/j.snb.2013.12.003.

[199] R. Pradhan, A. Mitra, S. Das, Impedimetric characterization of human blood using three-electrode based ECIS devices, J. Electr. Bioimpedance. 3 (2012) 12–19. doi:10.5617/jeb.238.

[200] J. Yang, W. Li, Q. Li, S. Wu, B. Yu, X. Jing, W. Li, Oxygen adsorption by carbon nanotubes and its application in radiotherapy, IET Nanobiotechnology. 1 (2007) 10–14. doi:10.1049/iet-nbt.

[201] D.P. Poenar, C. Iliescu, M. Carp, A.J. Pang, K.J. Leck, Glass-based microfluidic device fabricated by parylene wafer-to-wafer bonding for impedance spectroscopy, Sensors Actuators, A Phys. 139 (2007) 162–171. doi:10.1016/j.sna.2006.10.009.

[202] J.W. Wang, M.H. Wang, L.S. Jang, Effects of electrode geometry and cell location on single-cell impedance measurement, Biosens. Bioelectron. 25 (2010) 1271–1276. doi:10.1016/j.bios.2009.10.015.

[203] J. a Stolwijk, K. Matrougui, C.W. Renken, M. Trebak, Impedance analysis of GPCR-mediated changes in endothelial barrier function: overview and fundamental considerations for stable and reproducible measurements., Pflugers Arch. (2014). doi:10.1007/s00424-014-1674-0.

[204] C. Pautke, M. Schieker, T. Tischer, A. Kolk, P. Neth, W. Mutschler, S. Milz, Characterization of osteosarcoma cell lines MG-63, Saos-2 and U-2 OS in comparison to human osteoblasts, Anticancer Res. 24 (2004) 3743–3748. doi:10.1016/j.bone.2013.01.009.

[205] J.E. Aubin, Bone stem cells, J. Cell. Biochem. 72 (1998) 73–82. doi:10.1002/(SICI)1097-4644(1998)72:30/31+<73::AID-JCB11>3.0.CO;2-L.

[206] J.L. Millán, Alkaline phosphatases, Purinergic Signal. 2 (2006) 335–341. doi:10.1007/s11302-005-5435-6.

[207] E.E. Golub, K. Boesze-Battaglia, The role of alkaline phosphatase in mineralization, Curr. Opin. Orthop. 18 (2007) 444–448. doi:10.1097/BCO.0b013e3282630851.

[208] Y. Sugawara, K. Suzuki, M. Koshikawa, M. Ando, J. Iida, Necessity of enzymatic activity of alkaline phosphatase for mineralization of osteoblastic cells., Jpn. J. Pharmacol. 88 (2002) 262–269. doi:10.1254/jjp.88.262.

[209] W.E.G. Müller, X. Wang, B. Diehl-Seifert, K. Kropf, U. Schloßmacher, I. Lieberwirth, G. Glasser, M. Wiens, H.C. Schröder, Inorganic polymeric phosphate/polyphosphate as an inducer of alkaline phosphatase and a modulator of intracellular Ca2+ level in osteoblasts (SaOS-2 cells) in vitro, Acta Biomater. 7 (2011) 2661–2671. doi:10.1016/j.actbio.2011.03.007.

[210] W.N. Addison, F. Azari, E.S. Sørensen, M.T. Kaartinen, M.D. McKee, Pyrophosphate inhibits mineralization of osteoblast cultures by binding to mineral, up-regulating osteopontin, and inhibiting alkaline phosphatase activity, J. Biol. Chem. 282 (2007) 15872–15883. doi:10.1074/jbc.M701116200.

[211] M.J. Weiss, P.S. Henthorn, M. a Lafferty, C. Slaughter, M. Raducha, H. Harris, Isolation and characterization of a cDNA encoding a human liver/bone/kidney-type alkaline phosphatase., Proc. Natl. Acad. Sci. U. S. A. 83 (1986) 7182–7186. doi:10.1073/pnas.83.19.7182.

[212] C. Hildebrandt, H. Büth, S. Cho, Impidjati, H. Thielecke, Detection of the osteogenic differentiation of mesenchymal stem cells in 2D and 3D cultures by electrochemical impedance spectroscopy, J. Biotechnol. 148 (2010) 83–90. doi:10.1016/j.jbiotec.2010.01.007.

[213] M.J. Coelho, M.H. Fernandes, Human bone cell cultures in biocompatibility testing. Part II: effect of ascorbic acid, B-glycerophosphate and dexamethasone on osteoblastic differentiation, Biomaterials. 21 (2000) 1095–1102. doi:10.1016/S0142-9612(99)00192-1.

[214] M. Ahmad, M. McCarthy, G. Gronowicz, An in vitro model for mineralization of human osteoblast-like cells on implant materials, Biomaterials. 20 (1999) 211–220. doi:10.1016/S0142-9612(98)00152-5.

[215] G. Longo, C.A. Ioannidu, A.S. D'Abusco, F. Superti, C. Misiano, R. Zanoni, L. Politi, L. Mazzola, F. Iosi, F. Mura, R. Scandurra, Improving osteoblast response in vitro by a nanostructured thin film with titanium carbide and titanium oxides clustered around graphitic carbon, PLoS One. 11 (2016) 1–22. doi:10.1371/journal.pone.0152566.

[216] Q. Zhou, P. Yang, X. Li, H. Liu, S. Ge, Bioactivity of periodontal ligament stem cells on sodium titanate coated with graphene oxide, Sci. Rep. 6 (2016) 2–11. doi:10.1038/srep19343.

[217] P.S. Hung, Y.C. Kuo, H.G. Chen, H.H.K. Chiang, O.K.S. Lee, Detection of Osteogenic Differentiation by Differential Mineralized Matrix Production in Mesenchymal Stromal Cells by Raman Spectroscopy, PLoS One. 8 (2013) 1–7. doi:10.1371/journal.pone.0065438.

[218] Abnova kit instructions, Alkaline Phosphatase Assay Kit, (2017) 1–2. http://www.abnova.com/protocol_pdf/KA1642.pdf.

[219] P. Valerio, M.M. Pereira, A.M. Goes, M.F. Leite, The effect of ionic products from bioactive glass dissolution on osteoblast proliferation and collagen production, Biomaterials. 25 (2004) 2941–2948. doi:10.1016/j.biomaterials.2003.09.086.

[220] Sigma-Aldrich, 4-Methylumbelliferyl phosphate disodium salt - Product Information sheet, 17 (2016) 8168. http://www.sigmaaldrich.com/content/dam/sigma-aldrich/docs/Sigma/Product_Information_Sheet/1/m8168pis.pdf.

[221] C. Yildirim-Semerci, D. Benayahu, M. Adamovski, U. Wollenberger, An electrochemical assay for monitoring differentiation of the osteoblastic cell line (MBA-15) on the sensor chip,

Electroanalysis. 27 (2015) 1350–1358. doi:10.1002/elan.201400684.

[222] C. Yildirim-Semerci, D. Benayahu, M. Adamovski, U. Wollenberger, An Electrochemical Assay for Monitoring Differentiation of the Osteoblastic Cell Line (MBA-15) on the Sensor Chip, Electroanalysis. 27 (2015) 1350–1358. doi:10.1002/elan.201400684.

[223] H.K. Kleinman, D. Philp, M.P. Hoffman, Role of the extracellular matrix in morphogenesis, Curr. Opin. Biotechnol. 14 (2003) 526–532. doi:10.1016/j.copbio.2003.08.002.

[224] L.G. Griffith, M.A. Swartz, Capturing complex 3D tissue physiology in vitro, Nat. Rev. Mol. Cell Biol. 7 (2006) 211–224. doi:10.1038/nrm1858.

[225] N. Sánchez-Romero, C.M.S. Schophuizen, I. Giménez, R. Masereeuw, In vitro systems to study nephropharmacology: 2D versus 3D models, Eur. J. Pharmacol. 790 (2016) 36–45. doi:10.1016/j.ejphar.2016.07.010.

[226] S. Breslin, L. O'Driscoll, Three-dimensional cell culture: The missing link in drug discovery, Drug Discov. Today. 18 (2013) 240–249. doi:10.1016/j.drudis.2012.10.003.

[227] R. Edmondson, J.J. Broglie, A.F. Adcock, L. Yang, Three-Dimensional Cell Culture Systems and Their Applications in Drug Discovery and Cell-Based Biosensors, Assay Drug Dev. Technol. 12 (2014) 207–218. doi:10.1089/adt.2014.573.

[228] F. Pampaloni, E.G. Reynaud, E.H.K. Stelzer, The third dimension bridges the gap between cell culture and live tissue, Nat. Rev. Mol. Cell Biol. 8 (2007) 839–845. doi:10.1038/nrm2236.

[229] J.W. Haycock, 3D cell culture: a review of current approaches and techniques., 2011. doi:10.1007/978-1-60761-984-0_1.

[230] M. Sutherland, Cell and environment interactions in tumor microregions: The multicell spheroid model, Science, 240 (1988) 177–184. doi:10.1126/science.2451290.

[231] K.M. Yamada, E. Cukierman, Modeling Tissue Morphogenesis and Cancer in 3D, Cell. 130 (2007) 601–610. doi:10.1016/j.cell.2007.08.006.

[232] X. Zhang, W. Wang, W. Yu, Y. Xie, X. Zhang, Y. Zhang, X. Ma, Development of an in vitro multicellular tumor spheroid model using microencapsulation and its application in anticancer drug screening and testing, Biotechnol. Prog. 21 (2005) 1289–1296. doi:10.1021/bp050003l.

[233] A. Ivascu, M. Kubbies, Rapid generation of single-tumor spheroids for high-throughput cell function and toxicity analysis, J. Biomol. Screen. 11 (2006) 922–932. doi:10.1177/1087057106292763.

[234] V.E. Santo, S.P. Rebelo, M.F. Estrada, P.M. Alves, E. Boghaert, C. Brito, Drug screening in 3D in vitro tumor models: overcoming current pitfalls of efficacy read-outs, Biotechnol. J. 12 (2017). doi:10.1002/biot.201600505.

[235] M.S.R. Gudur, R.R. Rao, A.W. Peterson, D.J. Caldwell, J.P. Stegemann, C.X. Deng, Noninvasive quantification of in vitro osteoblastic differentiation in 3D engineered tissue constructs using spectral ultrasound imaging, PLoS One. 9 (2014) 1–10. doi:10.1371/journal.pone.0085749.

[236] R.J. Gilbert, M. Hoffman, A. Capitano, P.T.C. So, Imaging of three-dimensional epithelial architecture and function in cultured CaCO2A monolayers with two-photon excitation microscopy, Microsc. Res. Tech. 51 (2000) 204–210. doi:10.1002/1097-0029(20001015)51:2<204::AID-JEMT11>3.0.CO;2-W.

[237]   J. Sharpe, Optical Projection Tomography as a Tool for 3D Microscopy and Gene Expression Studies, Science, 296 (2002) 541–545. doi:10.1126/science.1068206.

[238]   A. Reininger-Mack, H. Thielecke, A.A. Robitzki, 3D-biohybrid systems: applications in drug screening, Trends Biotechnol. 20 (2002) 56–61. doi:10.1016/S0167-7799(01)01880-7.

[239]   S.P. Lin, T.R. Kyriakides, J.J.J. Chen, On-line observation of cell growth in a three-dimensional matrix on surface-modified microelectrode arrays, Biomaterials. 30 (2009) 3110–3117. doi:10.1016/j.biomaterials.2009.03.017.

[240]   S.H. Jeong, D.W. Lee, S. Kim, J. Kim, B. Ku, A study of electrochemical biosensor for analysis of three-dimensional (3D) cell culture, Biosens. Bioelectron. 35 (2012) 128–133. doi:10.1016/j.bios.2012.02.039.

[241]   H. Thielecke, A. Mack, A. Robitzki, A multicellular spheroid-based sensor for anti-cancer therapeutics, Biosens. Bioelectron. 16 (2001) 261–269. doi:10.1016/S0956-5663(01)00140-3.

[242]   D. Kloß, R. Kurz, H.G. Jahnke, M. Fischer, A. Rothermel, U. Anderegg, J.C. Simon, A.A. Robitzki, Microcavity array (MCA)-based biosensor chip for functional drug screening of 3D tissue models, Biosens. Bioelectron. 23 (2008) 1473–1480. doi:10.1016/j.bios.2008.01.003.

[243]   M.R. Abidian, E.D. Daneshvar, B.M. Egeland, D.R. Kipke, P.S. Cederna, M.G. Urbanchek, Hybrid Conducting Polymer-Hydrogel Conduits for Axonal Growth and Neural Tissue Engineering, Adv. Healthc. Mater. 1 (2012) 762–767. doi:10.1002/adhm.201200182.

[244]   S.R. Shin, S.M. Jung, M. Zalabany, K. Kim, P. Zorlutuna, S.B. Kim, M. Nikkhah, M. Khabiry, M. Azize, J. Kong, K.T. Wan, T. Palacios, M.R. Dokmeci, H. Bae, X. Tang, A. Khademhosseini, Carbon-nanotube-embedded hydrogel sheets for engineering cardiac constructs and bioactuators, ACS Nano. 7 (2013) 2369–2380. doi:10.1021/nn305559j.

[245]   S.-Z. Yow, T.H. Lim, E.K.F. Yim, C.T. Lim, K.W. Leong, A 3D Electroactive Polypyrrole-Collagen Fibrous Scaffold for Tissue Engineering, Polymers (Basel). 3 (2011) 527–544. doi:10.3390/polym3010527.

[246]   N. Li, Q. Zhang, S. Gao, Q. Song, R. Huang, L. Wang, L. Liu, J. Dai, M. Tang, G. Cheng, Three-dimensional graphene foam as a biocompatible and conductive scaffold for neural stem cells, Sci. Rep. 3 (2013) 1–6. doi:10.1038/srep01604.

[247]   J.Y. Rho, R.B. Ashman, C.H. Turner, Young's modulus of trabecular and cortical bone material: Ultrasonic and microtensile measurements, J. Biomech. 26 (1993) 111–119. doi:10.1016/0021-9290(93)90042-D.

[248]   T. Arai, T. Nishijo, Y. Matsumae, Y. Zhou, K. Ino, H. Shiku, T. Matsue, Noninvasive measurement of alkaline phosphatase activity in embryoid bodies and coculture spheroids with scanning electrochemical microscopy, Anal. Chem. 85 (2013) 9647–9654. doi:10.1021/ac401824q.

[249]   S. Bilgen, K. Kaygusuz, A. Sari, Renewable energy for a clean and sustainable future, Energy Sources. 26 (2004) 1119–1129. doi:10.1080/00908310490441421.

[250]   I. Dincer, Renewable energy and sustainable development: a crucial review, Renew. Sustain. Energy Rev. 4 (2000) 157–175. doi:10.1016/S1364-0321(99)00011-8.

[251]   C. Koroneos, T. Spachos, N. Moussiopoulos, Exergy analysis of renewable energy sources, Renew. Energy. 28 (2003) 295–310. doi:10.1016/S0960-1481(01)00125-2.

[252] A.J. McCormick, P. Bombelli, A.M. Scott, A.J. Philips, A.G. Smith, A.C. Fisher, C.J. Howe, Photosynthetic biofilms in pure culture harness solar energy in a mediatorless bio-photovoltaic cell (BPV) system, Energy Environ. Sci. 4 (2011) 4699. doi:10.1039/c1ee01965a.

[253] A.J. McCormick, P. Bombelli, R.W. Bradley, R. Thorne, T. Wenzel, C.J. Howe, Biophotovoltaics: oxygenic photosynthetic organisms in the world of bioelectrochemical systems, Energy Environ. Sci. 8 (2015) 1092–1109. doi:10.1039/C4EE03875D.

[254] P. Bombelli, T. Müller, T.W. Herling, C.J. Howe, T.P.J. Knowles, A high power-density, mediator-free, microfluidic biophotovoltaic device for cyanobacterial cells, Adv. Energy Mater. 5 (2015) 1–6. doi:10.1002/aenm.201401299.

[255] S. Fowler, R. Roush, J. Wise, OpenStax College, Rice University, Concepts of biology, 2013. doi:10.2307/4450113.

[256] M. Rasmussen, S.D. Minteer, Photobioelectrochemistry: Solar Energy Conversion and Biofuel Production with Photosynthetic Catalysts, J. Electrochem. Soc. 161 (2014) H647–H655. doi:10.1149/2.0651410jes.

[257] P. Bombelli, M. Zarrouati, R.J. Thorne, K. Schneider, S.J.L. Rowden, A. Ali, K. Yunus, P.J. Cameron, A.C. Fisher, D. Ian Wilson, C.J. Howe, A.J. McCormick, Surface morphology and surface energy of anode materials influence power outputs in a multi-channel mediatorless bio-photovoltaic (BPV) system, Phys. Chem. Chem. Phys. 14 (2012) 12221. doi:10.1039/c2cp42526b.

[258] J.O. Calkins, Y. Umasankar, H. O'Neill, R.P. Ramasamy, High photo-electrochemical activity of thylakoid–carbon nanotube composites for photosynthetic energy conversion, Energy Environ. Sci. 6 (2013) 1891. doi:10.1039/c3ee40634b.

[259] D. Gerster, J. Reichert, H. Bi, J. V. Barth, S.M. Kaniber, A.W. Holleitner, I. Visoly-Fisher, S. Sergani, I. Carmeli, Photocurrent of a single photosynthetic protein, Nat. Nanotechnol. 7 (2012) 673–676. doi:10.1038/nnano.2012.165.

[260] O. Yehezkeli, R. Tel-Vered, J. Wasserman, A. Trifonov, D. Michaeli, R. Nechushtai, I. Willner, Integrated photosystem II-based photo-bioelectrochemical cells, Nat. Commun. 3 (2012) 742–747. doi:10.1038/ncomms1741.

[261] W. Verstraete, K. Rabaey, Critical Review Microbial Fuel Cells : Methodology and Technology, Environ. Sci. Technol. 40 (2006) 5181–5192. doi:10.1021/es0605016.

[262] L. Darus, T. Sadakane, P. Ledezma, S. Tsujimura, I. Osadebe, D. Leech, L. Gorton, S. Freguia, Redox-Polymers Enable Uninterrupted Day/Night Photo-Driven Electricity Generation in Biophotovoltaic Devices, J. Electrochem. Soc. 164 (2017) H3037–H3040. doi:10.1149/2.0091703jes.

Appendix

Papers included in the thesis

Please see the attachment "Papers and unpublished material" for links and content.

DTU Nanotech
Department of Micro- and Nanotechnology